Swansea University E-Theses

Secondary ion mass spectrometry and resonant ionisation mass spectrometry studies of nickel contacts to silicon carbide.

John, Gareth David

How to cite:

John, Gareth David (2004) *Secondary ion mass spectrometry and resonant ionisation mass spectrometry studies of nickel contacts to silicon carbide..* thesis, Swansea University.
http://cronfa.swan.ac.uk/Record/cronfa42495

Use policy:

This item is brought to you by Swansea University. Any person downloading material is agreeing to abide by the terms of the repository licence: copies of full text items may be used or reproduced in any format or medium, without prior permission for personal research or study, educational or non-commercial purposes only. The copyright for any work remains with the original author unless otherwise specified. The full-text must not be sold in any format or medium without the formal permission of the copyright holder. Permission for multiple reproductions should be obtained from the original author.

Authors are personally responsible for adhering to copyright and publisher restrictions when uploading content to the repository.

Please link to the metadata record in the Swansea University repository, Cronfa (link given in the citation reference above.)

http://www.swansea.ac.uk/library/researchsupport/ris-support/

Secondary ion mass spectrometry and resonant ionisation mass spectrometry studies of nickel contacts to silicon carbide.

by

Gareth David John B.Sc, M. Res.

This thesis is submitted to the University of Wales in candidature for the degree of Doctor of Philosophy

September 2004

Department of Physics
University of Wales Swansea
Singleton Park
Swansea SA2 8PP

ProQuest Number: 10801725

All rights reserved

INFORMATION TO ALL USERS
The quality of this reproduction is dependent upon the quality of the copy submitted.

In the unlikely event that the author did not send a complete manuscript
and there are missing pages, these will be noted. Also, if material had to be removed,
a note will indicate the deletion.

ProQuest 10801725

Published by ProQuest LLC (2018). Copyright of the Dissertation is held by the Author.

All rights reserved.
This work is protected against unauthorized copying under Title 17, United States Code
Microform Edition © ProQuest LLC.

ProQuest LLC.
789 East Eisenhower Parkway
P.O. Box 1346
Ann Arbor, MI 48106 – 1346

DECLARATION

This work has not previously been accepted in substance for any degree and is not being concurrently submitted in candidature for any degree.

Signed.. ....(candidate)

Date......18/01/2005..

STATEMENT 1

This thesis is the result of my own investigations, except where otherwise stated.

Other sources are acknowledged by footnotes giving explicit references. A bibliography is appended.

Signed.... ....(candidate)

Date........18/01/2005..

STATEMENT 2

I hereby give consent for my thesis, if accepted, to be available for photocopying and for inter-library loan, and for the title and summary to be made available to outside organisations.

Signed...... ....(candidate)

Date..........18/01/2005..

Acknowledgements

There are many people to whom I am indebted for their help and friendship during this research. Firstly, I must extend my deepest thanks to my supervisor Dr. Peter Dunstan, who has been totally supportive throughout these studies and has given an enormous amount to aid my research. I would also like to thank Professor Helmut Telle and the staff at the Katholieke Universiteit Leuven for their advice and support during the collaborative studies. I would especially like to thank Dr. Jeroen Bastiaansen for his friendship and advice (and his wife's cooking!).

I must also thank EPSRC for their financial support throughout this research.

I would also like to thank all my friends here in Swansea, particularly Martyn Brown, Greg Owen, David Walters, Gavin Williams, Andrew "Kenny" Jones, Steve Bidder, Rachel Davies, Richard Bayliss and my mate from the other lab Mat Ackland. In addition, the research would get nowhere without the support of the technical staff in the Swansea Physics Department, so I must relay my thanks to Hugh Thomas, Ray Squire, Julian Kivell, Paul Schembri, Dave Payne and Mike Rogers. A special note of thanks must go to Andrew Jardine in the School of Engineering who helped me out of tight spots on many an occasion. An extra note of thanks must also go to Owen Guy and Gareth Pope who helped in the preparation of samples.

Finally, I must give the utmost thanks to my parents and the rest of my family, who have been absolutely awesome throughout in their support and, in particular, my fiancée Tara Meacham, who has been the light in dark times!!

Abstract

Time-of-flight secondary ion mass spectrometry (TOF-SIMS) and resonant ionisation mass spectrometry (RIMS) have been used to perform depth profile analyses on nickel (Ni) contacts to silicon carbide (SiC) to understand the interfacial properties. In particular, as-deposited Schottky contacts and high temperature annealed Ohmic contacts have been characterised. Previous literature had indicated that the chemistry of the interface controlled the electrical properties of the contact.

Using the TOF-SIMS system, depth profiles have been performed with the standard duoplasmatron ion source and a newly introduced liquid metal ion gun. Sputtering conditions have been optimised enabling detailed depth profiling of Schottky and Ohmic samples. The data from these samples have indicated a distinct difference between the two contact types. Schottky samples have been shown to have an abrupt interface with any interfacial reaction appearing to be confined to the intimate interface. This region had no significant affect on ion yield. Conversely, the Ohmic samples exhibited an extended Si composition well into the Ni contact layer. Moreover, the ion yield varied substantially throughout the contact layer indicating matrix changes were present as a result of annealing to 1000°C.

RIMS studied the variation of Ni atoms sputtered into the Ni ground state (a^3F_4) and first excited state (a^3D_3) to determine variation in chemical bonding as a function of depth through the contact. Using a defocused ion beam passing through an aperture, detailed depth profiles were obtained by using two-colour, two-step resonant ionisation scheme. Again, a significant variation exists between the RIMS signals from Ohmic and Schottky samples. The ratio of the excited state to ground state for Ni showed measurable variations indicative of multiple Ni-silicide phases. Models for these interfaces are proposed and support other studies performed on this material system.

The success of these techniques is reviewed together with suggestions for experimental development.

Contents

Chapter 1: Introduction 1

1.1 General Introduction 1

1.2 Silicon Carbide (SiC) 2

1.3 Semiconductor contacts 3

1.4 Outline of Thesis 4

1.5 References 6

Chapter 2: Theory of SIMS 7

2.1 Introduction to SIMS 7

2.2 Sputtering 8

2.2.1 Sputter Yield 12

2.3 Influences on Sputter Yield 14

2.3.1 Primary Ion Mass and Energy 14

2.3.2 Incidence angle of primary ions and sample properties 16

2.4 Properties of sputtered particles 19

2.4.1 Energy and angular distribution 19

2.4.2 Sputtering into excited and charged states 20

2.4.3 Ionisation probability and secondary ion emission 21

2.5 Depth Profiling 22

2.5.1 Depth Resolution 23

2.6 Influences on Depth Resolution 23

2.6.1 Primary Ion Mass vs Range 24

2.6.2 Primary Ion Energy vs Range 26

2.6.3 Incidence angle of primary ions 27

2.7 Summary 27

2.8 References 27

Chapter 3: Theory of RIMS **30**

3.1 Introduction to RIMS 30

3.2 Resonant Multi-Photon Ionisation (RMPI) 30

3.3 Non-Resonant Multi-Photon Ionisation (NRMPI) 31

3.4 Ionisation scheme considerations 32

3.5 Saturation conditions for the resonant ionisation process 32

3.5.1 Rate Equations 33

3.6 Determination of nickel-silicon bonding using RIMS 35

3.6.1 Population partitions 35

3.6.2 Velocity distributions 37

3.7 RIMS Depth Profiling 39

3.8 Summary 39

3.9 References 40

Chapter 4: Semiconductor contacts and their preparation **41**

4.1 Introduction 41

4.2 Schottky contacts 41

4.3 Ohmic contacts 46

4.4 Sample Preparation 48

4.5 Samples used in SIMS/RIMS studies and bombardment conditions 50

4.6 Summary 51

4.7 References 51

Chapter 5: Experimental set-up **53**

5.1 Experimental set-up at Swansea 53

5.1.1 Vacuum system 54

5.1.2 Valve system 55

5.1.3 Primary ion column 57

5.1.4 Liquid metal ion source 62

5.1.5 Sample manipulation 65

5.1.6 Time-of-flight reflectron mass analyser 65

5.1.7 Data acquisition 66

5.1.8 Acquisition of depth profiles 67

5.1.9 Overlapping target location of primary ion guns 69

5.2 Apparatus at Leuven 72

5.2.1 Primary ion column 73

5.2.2 Main chamber and transfer system 75

5.2.3 Time-of-flight mass spectrometer 76

5.2.4 Ionising laser systems 78

5.2.5 Time synchronisation of system 79

5.3 Summary 80

5.4 References 81

Chapter 6: TOF-SIMS Measurements 82

6.1 Introduction 82

6.2 Optimisation of TOF-SIMS parameters 83

6.2.1 Selection of primary ion source for analysis 83

6.3 TOF-SIMS depth profiles of Ni/SiC samples using both ion sources 88

6.3.1 Time-to-depth conversion of profiles 89

6.3.2 Depth profile of Schottky Ni/SiC sample using two primary ion sources 89

6.3.3 Conclusions of Schottky Ni/SiC depth profile 93

6.3.4 Depth profile of Ohmic Ni/SiC sample using two primary ion sources 93

6.3.5 Overall assessment of technique of using both ion sources 96

6.4 TOF-SIMS depth profiles of Ni/SiC samples using LMIG in raster mode 96

6.4.1 Investigation into topographic effects of primary ion beam rastering 100

6.4.2 Overall assessment of technique of using rastered primary ion beam 102

6.5 TOF-SIMS depth profiles of Ni/SiC samples using LMIG with a defocused ion beam 103

6.5.1 Depth profile of Schottky Ni/SiC sample using defocused 15keV Ga^+ ion beam 103

6.5.2 Depth profile of Ohmic Ni/SiC sample using defocused 15keV Ga^+ ion beam 106

6.5.3 Evaluation of technique of using defocused Ga^+ ion beam 108

6.5.4 Depth profile of Schottky Ni/SiC sample using defocused 7keV Ga^+ ion beam 109

6.5.5 Depth profile of Ohmic Ni/SiC sample using defocused 7keV Ga^+ ion beam 113

6.6 Conclusion of TOF-SIMS depth profiles on Ni/SiC samples 116

6.7 References 118

Chapter 7: TOF-RIMS Measurements 120

7.1 Introduction 120

7.2 Velocity distributions and population partitions of nickel and associated silicides 121

7.3 TOF-RIMS depth profiling of Ni/SiC samples 122

7.3.1 RIMS depth profiling of Schottky Ni/SiC sample 124

7.3.2 RIMS depth profiling of Ohmic Ni/SiC sample 128

7.3.3 Evaluation of RIMS depth profiling 131

7.4 Optimisation of RIMS setting using a defocused primary ion beam 132

7.4.1 RIMS depth profiles of test sample 134

7.5 TOF-RIMS depth profiles of Ni/SiC samples using a defocused beam 137

7.5.1 RIMS depth profiling of Schottky Ni/SiC sample 137

7.5.2 RIMS depth profiling of Ohmic Ni/SiC sample 141

7.6 Conclusion of RIMS depth profiles on Ni/SiC samples 146

7.7 References 147

Chapter 8: Conclusions and Future Work **149**

8.1 Summary of results 149

8.2 Ni/SiC contacts: a proposed model based on TOF-SIMS and RIMS 151

8.3 Suggestions for future work 153

8.4 References 154

Chapter 1: Introduction

1.1 General introduction

It is well known that the properties of semiconductor devices are in many ways controlled by the nature of the contacts and interfaces that make up the device structure. For instance, the controlled fabrication of lattice matched III-V semiconductor interfaces has enabled the realisation of the quantum well laser. Clearly, the understanding of the physics of surfaces and interfaces has been a major driving force. Surface science techniques such as x-ray photoelectron spectroscopy (XPS), x-ray diffraction, scanning tunnelling microscopy (STM), Auger electron spectroscopy (AES) and low energy electron diffraction (LEED) have greatly contributed in the preparation of surfaces and the exploitation of electronic properties. Whilst surface science is now a mature field, there are still characterisation challenges, such as buried interfaces, which offer difficult propositions for many of these techniques.

Secondary ion mass spectroscopy (SIMS) became a commercial technique in the 1970's and it enabled the elemental nature of a sample to be resolved. The first instrument was made by Herzog and co-workers[1] under a NASA contract to study samples brought back to earth. Its part per million sensitivity meant that it was soon adopted by the semiconductor industry to investigate the level of doping within semiconductor materials. As an ion bombardment based technique, it has the drawback of being inherently destructive to samples. However, when correctly controlled, it is able to erode individual surface layers and depth profile through structures, thereby allowing characterisation of elements within a sample structure.

Resonance ionisation mass spectrometry (RIMS) is a laser based spectroscopy technique that has developed alongside SIMS over the past 30 years. It is, in principle, a simple technique which exploits well established quantum physics. In a simple two-step scheme, the technique uses photons from a tuneable laser to resonantly excite electrons from a specific energy level of a specific atom to a higher-lying state in that atom. It is then possible to use a second photon to excite the electrons above the ionisation potential. Hence, an ion-electron pair are produced enabling the photo-ionised atom to be detected in the same method as SIMS. This selectivity, obtained by using tuneable lasers, enables further information to be drawn on the nature of the sample, in particular taking elemental analysis towards chemical analysis. Primarily,

RIMS has been used for trace element analysis in material investigations[2,3] as it is capable of partially overcoming mass interferences present in SIMS, and has an increased detection yield via selective ionisation of sputtered neutrals. Subsequent work by Downey *et al* [4,5] on depth profiling of AlGaAs semiconductor structures showed that RIMS is much less susceptible to matrix effects than SIMS and that RIMS is an effective technique for interface analysis.

The objective of the present experimental work is to demonstrate the depth profiling capabilities of both SIMS and RIMS on samples that have varying interfacial compositions. By exploiting the sensitivity and selectivity of the techniques, as well as the depth profiling properties, the feasibility of depth profiling through semiconductor contacts is investigated. Moreover, the material systems investigated have significant technological importance and the mechanisms that dictate their electrical properties are the subject of some speculation. The experiments described in this thesis were performed using unique systems based at both Swansea and Leuven. Careful consideration was given to the bombarding conditions in both experimental set-ups and the thesis details modifications and experimental parameters refined to obtain accurate depth profiling data.

1.2 Silicon carbide (SiC)

The semiconductor industry has been dominated by silicon for many years due to its electrical properties, low cost and availability. As a result, the amount of research into Si based devices and improving the associated efficiency and capability of these devices has been enormous and helps support an industry worth billions of dollars. However, as the requirement for devices capable of operating in extreme conditions increases, Si based devices begin to breakdown. The search for alternative semiconductor materials capable of operating in such environments is a source of constant interest, thus research into materials such as diamond, silicon carbide and gallium nitride has increased substantially.

SiC is a wide band gap semiconductor, which permits SiC devices to be used for high temperature applications. Indeed, the US Air Force has estimated that SiC based electronics employed on a General Dynamics F-16 fighter aircraft could enable a reduction in weight of perhaps 100kg or more, primarily because cooling systems for

devices residing in hot environments would no longer be required. The weight saving inherently brings with it substantial benefits in terms of efficiency and performance.

Other advantages of SiC as a material include high thermal conductivity, high saturated electron drift velocity and a high breakdown electric field. Table 1.1 compares these parameters for Si, GaAs and various SiC polytypes.

	Si	GaAs	6H-SiC	4H-SiC	3C-SiC
Band Gap (eV)	1.1	1.42	3.0	3.2	2.3
Breakdown Field (V/m)	$6x10^7$	$6x10^7$	$3.2x10^8$	$3x10^8$	$>1.5x10^8$
Saturated Electron Drift Velocity (m/s)	$1x10^5$	$1x10^5$	$2x10^5$	$2x10^5$	$2.5x10^5$
Thermal Conductivity (W/cm.K)	1.5	0.5	4.9	4.9	5.0

Table 1.1: Comparison of physical parameters for various semiconductors.

These parameters, in addition to high chemical stability and high resistance to radiation damage, makes SiC an ideal candidate for high temperature, high frequency and high power applications. Moreover, its native oxide is SiO_2, and hence its integration into existing Si based fabrication methods is seen as a major advantage over other alternative high temperature, high power candidates.

1.3 Semiconductor contacts

Creating an electronic device requires that an electrical contact is made to a semiconductor. A metal contact layer is generally deposited on the semiconductor surface to create contacts that are either Ohmic or Schottky in nature. The contacts are Schottky if an electrical barrier exists between the metal contact and the semiconductor and Ohmic if current is allowed to flow in both directions across the metal-semiconductor junction.

Nickel has been used extensively in Si based contacts due to low contact resistivity and easily tailored electrical properties, which are varied via contact preparation. As a result, its interaction with SiC has proved of equal research interest. However, when a Ni/SiC contact is annealed to temperatures in excess of ~900°C, the rectifying nature is replaced by an Ohmic character.[6] To this end, research has been undertaken to determine the physical and chemical changes that are induced by the annealing process

to cause the shift in electrical characteristics. Studies on Ni/SiC samples have been performed using transmission electron microscopy (TEM)[7], x-ray photoelectron spectroscopy (XPS)[8]and very recently secondary ion mass spectrometry (SIMS)[9] (although the SIMS measurements were only performed on samples exhibiting Schottky characteristics). Combining the results from these studies, it is clear that the contact interface layer is substantially altered when annealed. TEM studies indicate the formation of voids, while XPS data[10] shows evidence of Ni and Si core level broadening due to chemical reactions and possible silicide formation. To achieve control of the interface between Ni and SiC, the mechanism for chemical and structural changes is important, particularly if other control layers can be utilised to prohibit temperature effects.

The variety of properties exhibited in this contact interface offer the potential for a detailed depth profile study using SIMS and RIMS. This has two major benefits; firstly, the development of the techniques, and secondly, gaining a detailed knowledge of the chemistry and physics of the interface will highlight possible methods for interface control.

1.4 Outline of thesis

In order to generate a best possible depth profile and understand SIMS mechanisms, chapter 2 introduces the theory of time-of-flight secondary ion mass spectrometry (TOF-SIMS). Highlighted are the issues of sputtering of secondary species from a sample surface and how primary ion and sample parameters affect the yield of sputtered particles. The technique of depth profiling is then reviewed with the associated aspect of depth resolution and the factors that influence it. The aim of the chapter is to establish the requirements for accurate TOF-SIMS depth profiling.

Similarly, chapter 3 briefly examines the theory of resonant ionisation spectroscopy (RIS), from which resonant ionisation mass spectrometry (RIMS) is developed. The chapter covers the basic theory of resonant ionisation and demonstrates how bonding mechanisms in Ni-Si based structures can be ascertained by means of the measuring the population of atoms in specific electronic states and the velocity distribution of atoms sputtered into these electronic states.

Applying these techniques to a semiconductor contact system requires basic knowledge of the theory of metal-semiconductor contacts, specifically the formation of a Schottky barrier and how the rectifying contacts differ from Ohmic contacts. Chapter 4 introduces these concepts and also discusses the processes involved in sample preparation used in these experiments.

An overview of the experimental apparatus used to perform experiments is presented in Chapter 5. A full description of the TOF-SIMS system at Swansea is offered, along with modifications that have been instigated during the course of these studies and details on the optimisation of the system. The time-of-flight RIMS system used whilst undertaking collaborative work at Katholieke Universiteit Leuven in Belgium is also described.

The TOF-SIMS results obtained on both as-deposited and annealed Ni/SiC samples are presented and discussed in chapter 6. The chapter shows the development of the depth profile acquisition process, beginning with profiles obtained using two primary ion sources then moving on to a single ion source employing an ion beam raster technique. The problems associated with each of the techniques are discussed and a solution is provided via modification of the primary beam. The final profiles make use of a defocused primary ion beam to acquire mass spectra and the results of these profiles are also discussed.

Chapter 7 introduces the RIMS results that were achieved on as-deposited and annealed Ni/SiC samples during the collaborative studies at Leuven. The initial profiles were acquired using a focused ion beam to sputter material for resonant laser ionisation. A series of experiments on a thin, multi-layered sample were then undertaken to enhance depth resolution by defocusing the ion beam and passing it through a diaphragm aperture. RIMS depth profiles were then obtained on the Ni/SiC samples using the new enhanced resolution method and again the results are discussed.

Finally, chapter 8 compares the results obtained through TOF-SIMS and RIMS analysis and discusses the implications of the findings. The conclusions are then drawn along with suggestions for future refinement of the work.

1.5 References

[1] R.F.K. Herzog, W.P. Poschenrieder abd F.G. Satkiewicz, NASA, Contract no. NAS5-9254, final report GCA-TR-67-3N (1967).

[2] N. Winograd, J.P. Baxter, F.M. Kimock, Chem. Phys. Lett. **88** (6), 581 (1982).

[3] J.E. Parks, H.W. Schmitt, G.S. Hurst, W.M. Fairbank, Thin Solid Films **108**, 69 (1983).

[4] S.W. Downey, A.B. Emerson, R.F. Kopf, J. Vac. Sci Technol. **B10** (1), 385 (1992).

[5] S.W. Downey, R.F. Kopf, E.F. Schubert, J.M. Kuo, Appl. Opt. **33**, 4938 (1990).

[6] A. Kestle, S.P. Wilks, P.R. Dunstan, M. Pritchard, P. Mawby, Electronics Letters Vol. **36** (3), 267 (2000).

[7] B. Pécz, Appl. Surf. Sci. **184**, 287 (2001).

[8] A. Kakanakova-Georgieva, Ts. Marinova, O. Noblanc, C. Arnodo, S. Cassette, C. Brylinski, Thin Solid Films **343-344**, 637 (1999).

[9] S. Roy, C. Jacobs, S. Basu, Solid-State Electronics **47**, 2035 (2003).

[10] W.Y. Lee, The control of metal-silicon carbide contact using a silicon interlayer, PhD Thesis, University of Wales Swansea (2004).

Chapter 2: Theory of SIMS

2.1 Introduction to SIMS

In simplistic terms, secondary ion mass spectrometry (SIMS) is a surface analysis technique that uses bombardment of a solid surface with a primary ion species to result in the emission of secondary sputtered ions from the target solid. An appropriate detector to produce a mass spectrum of the chemical structure of the solid may then detect these sputtered ions. However, there are a great number of factors that influence the spectral result, which must be taken into account in order to achieve reliable results. These factors may be broadly divided into two separate groups: the primary ion parameters (mass & atomic number, energy, angle of incidence) and the target sample characteristics (mass & atomic number, surface binding energy, structure). SIMS also forms the basis of resonant ionisation mass spectrometry (RIMS), whereby it is the neutral species sputtered from the sample surface, which undergo laser post-ionisation, that are of interest. The concept of RIMS is discussed in chapter 3 but much of the bombardment theory described in this chapter is also of relevance in RIMS.

There are two distinct varieties of SIMS analyses: dynamic SIMS and static SIMS. Until the early 1980's, dynamic SIMS was considerably the most widely used SIMS technique. This was due to the high primary ion flux that was required to create sufficient secondary ions for detection. Consequently, dynamic SIMS made use of the destructive nature of the technique and was used to measure the composition of samples as a function of depth. Dynamic SIMS found widespread use in semiconductor analysis, such as in determining dopant concentrations. However, it was Benninghoven in 1970[1] who showed that a very low primary ion flux ($<1nA.cm^{-2}$) could be used to obtain spectral data of a surface in a time substantially shorter than the erosion time of a monolayer, which resulted in the name static SIMS. This required a considerable advance in the transmission and detection efficiency of the system such that single particle detection was possible. A variety of different detecting systems were also employed to enable mass discrimination, including magnetic sector, quadrupole and time-of-flight detectors. The system used in these experiments was a time-of-flight (TOF) detector and is fully described in chapter 5.

Occasionally included as a separate variety of SIMS is imaging SIMS. Imaging SIMS is a technique that can make use of dynamic or static SIMS. By scanning a beam across

the sample, a map may be built up of the secondary ion intensity of an element as a function of its lateral location.

There are a number of factors that influence the magnitude of the secondary ions of a particular species emitted from a target sample. These include; the primary particle flux (generally ionic) that is incident on the surface; the concentration of the target species; the sputter yield of the target species, which determines the number of sputtered particles per incident particle; the ionisation probability, which in conjunction with sputter yield determines the number of sputtered ions of the target species; and the transmission efficiency of the experimental analysis system. These factors may be incorporated to form the basic SIMS equation[2]:

$$I_s^m = I_p \cdot y_m \cdot \alpha^+ \cdot \theta_m \cdot \eta \qquad \textbf{Equation 2.1}$$

where: $I^m{}_s$ is the secondary ion current of species m,

I_p is the primary particle flux,

y_m is the total sputter yield of species m (both neutral and ionic),

α^+ is the ionisation probability to positive ions,

θ_m is the fractional concentration of m in the surface layer,

η is the transmission of the system.

The most crucial factors in this equation are the sputter yield, y_m, and the ionisation probability, α^+, since they are very much dependent on the primary ion properties and sample properties. Together, the factors represent the sputter ion yield of an element or compound within a matrix. This chapter highlights these factors and their origins, together with depth profiling and resolution issues, as well as giving a brief overview of the formulisation and theory of energy transfer and sputtering mechanisms.

2.2 Sputtering

Sputtering is a process that was first observed in gas discharges approximately 150 years ago[3] but was not recognised for a further 50 years[4]. Sputtering takes place when a primary ion is incident on the surface of a target structure. The ion enters the solid and transfers its energy via elastic and inelastic collisions. The inelastic collisions take place with the electrons of the target atoms and the energy transferred is far lower in

magnitude then the energy transferred in the elastic collisions with the target nuclei. If the energy transferred to a target atom is sufficiently large, i.e. greater than its lattice site binding energy of the lattice site, it will be dislocated from its site and become a recoil atom. This recoil atom may then set further target atoms in motion possibly leading to a cascade. When the recoil atoms reach the surface layer of the solid due to the cascade, they may escape the surface provided their kinetic energy is greater than the binding energy at the surface. An atom that escapes from the surface in this way is described as a sputtered atom. There are three distinct forms of sputtering that may occur due to ion bombardment: single knock-on, linear collision cascade, and spike.

Single knock-on

This occurs when the primary incident ion is in the eV range, although this stretches to the low keV range when very light primary ions are used as a result of inefficient energy transfer during the collision. A target atom receives sufficient energy to be ejected from the surface. The energy transfer occurs either via a direct collision with the incident ion or a collision with a primary recoil atom.

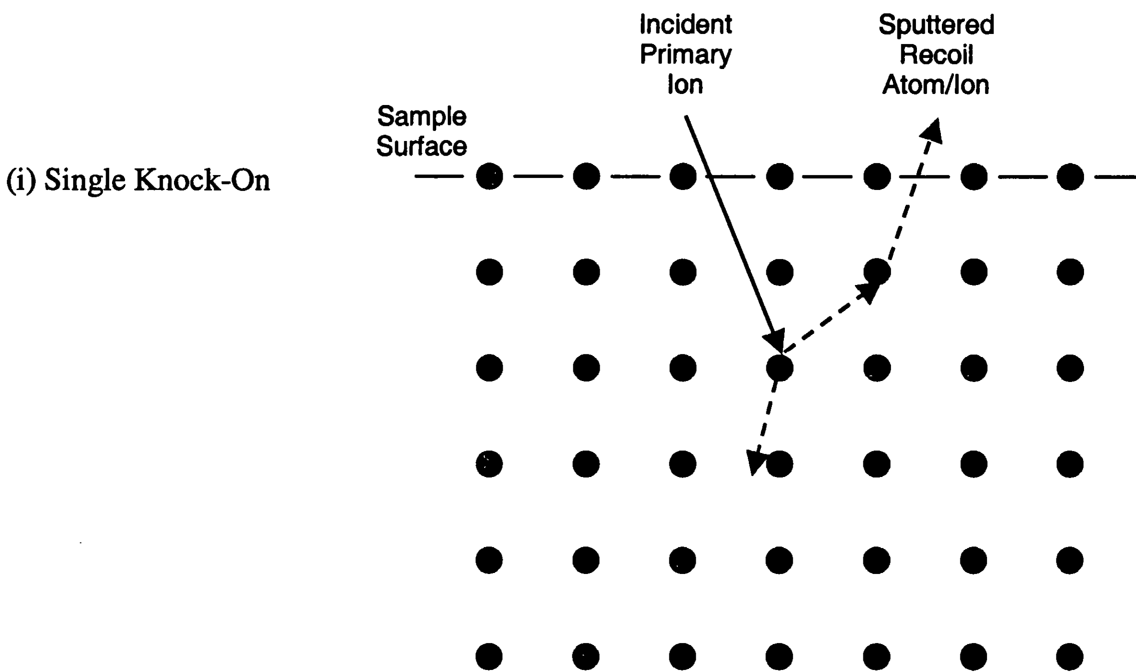

Figure 2.1: Example of a single knock-on collision. The red lines represent the path of the incident primary ion (dotted after collision). The blue dotted lines represent the path of the recoil atom.

Linear collision cascade

This event is typical when the primary incident ion is within the keV to MeV range, although it does not hold for particularly heavy ions (relative to the target species), as

these will tend to be brought to rest quickly and cause collisional spikes within the target (see next collision type).

When a primary ion transfers sufficient energy to a target atom, the target atom, and indeed the primary ion, may set other recoil atoms in motion. The propagation may continue, setting up a cascade, which can lead to the ejection of multiple sample atoms per incident ion.

(ii) Linear cascade

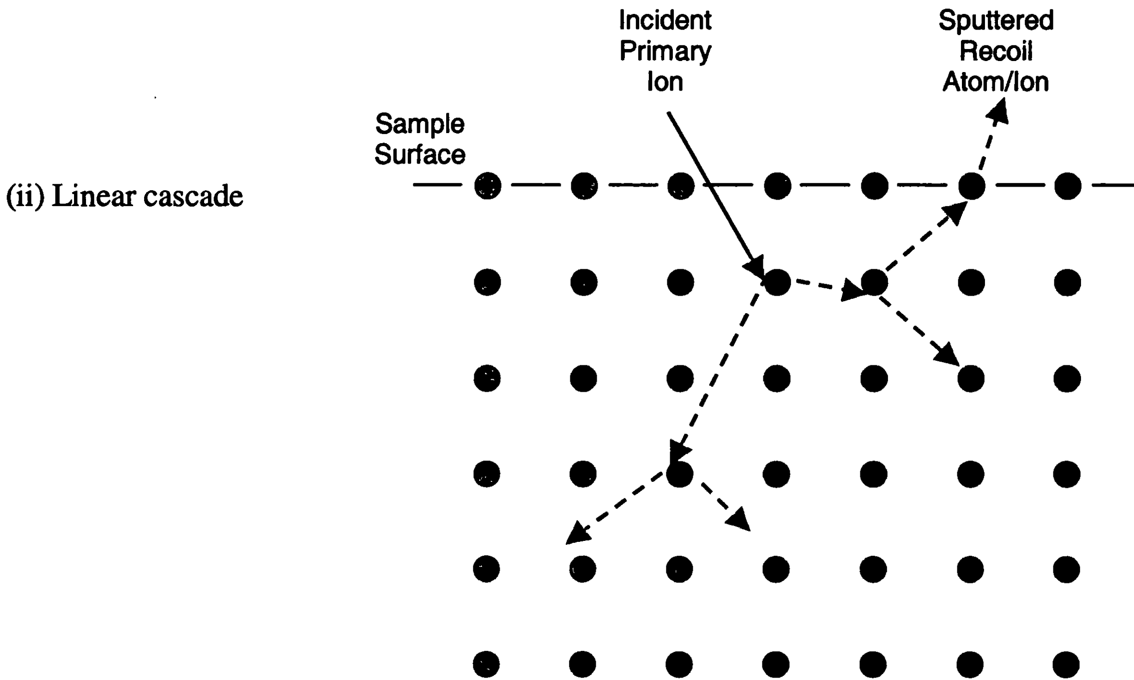

Figure 2.2: Example of a linear collision cascade. The red lines represent the path of the incident primary ion (dotted after collisions). The blue dotted lines represent the paths of the recoil atoms following a collision.

Spike

The spike collision occurs when the incident particles have energies in the MeV range and beyond. It is an evolution of the linear collision cascade and may be distinguished from the latter as it results in a substantially higher number of atoms per unit volume in motion. An example of this collision is shown in Figure 2.3. The extreme disturbance to the target atoms caused by the incident ion coupled with its projected range into the target means that this form of collision is less desirable for high resolution analysis.

It should be noted that for ease of clarity, the diagrams of the linear collision cascade and spike collision cases are rather simplified when regarding the number of sputtered atoms in comparison to the single knock-on regime.

(iii) Spike

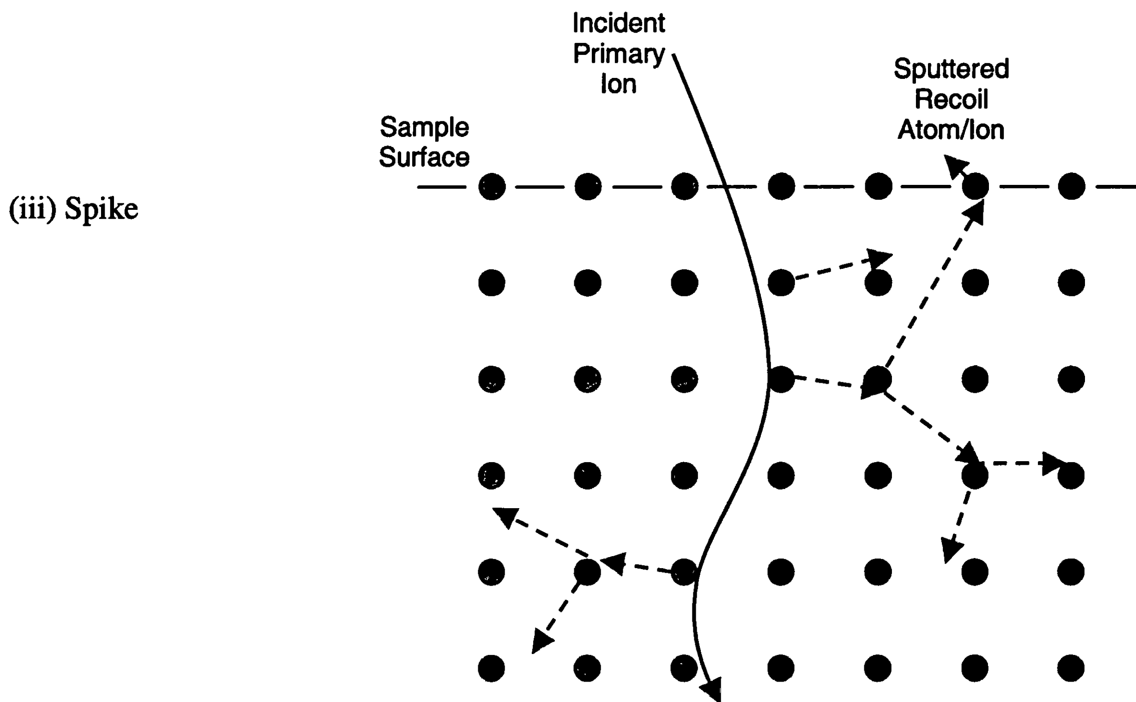

Figure 2.3: Example of spike collisions. The red line represents the path of the incident primary ion. The blue dotted lines represent the paths of the recoil atoms following a collision.

All the collision processes described are effectively differentiated by the number of collisions that occur before an atom is sputtered and the number of recoil atoms in motion within a volume. It is the linear collision cascade that is most applicable to this work and, as such, is only system that shall be considered in the theory.

Energy Transfer Mechanisms

When an energetic atom, or ion, enters a solid surface, it loses energy via collisions with constituent atoms of the target. If the atomic density of the target medium is taken as N, the mean energy loss per path length, or stopping force, is given by [5]:

$$\frac{dE}{dR} = -N \cdot S(E)$$ **Equation 2.2**

where *S(E)* is the stopping cross-section. The energy loss of the incident particle is divided between nuclear stopping, $S_N(E)$, whereby energy is transferred to recoiling atoms, and electronic stopping, $S_E(E)$, a general term describing projectile energy lost through electronic excitation as well as through electron capture by the ion. Therefore,

$$S(E) = S_N(E) + S_E(E) = \int T_N d\sigma + \int T_E d\sigma \qquad \textbf{Equation 2.3}$$

where $d\sigma = d\sigma\ (T_N, T_E)$ is the differential cross-section, which is dependent on the nuclear and electronic energy loss, T_N and T_E respectively, in individual ion-atom collisions [6]. While an incident particle will experience loss via energy transfer to both nuclei and electrons, the relative contribution of each of the components is dependent on the velocity of the projectile. At low velocities, nuclear stopping tends to dominate with significant angular deflection to the incident particle, while at higher velocities, electronic stopping becomes more important and indeed supersedes that of nuclear stopping within the Lindhard-Scharff [6,7]and Bethe[8] regions. The actual point at which electronic stopping dominates depends primarily on the atomic number of the incident particle. Further detailing on the nuclear and electronic stopping and associated corrections can be found in work by Glazov and Sigmund[5], and references therein. Nuclear stopping is a fundamental aspect of the sputter yield formula described in the following section

2.2.1 Sputter Yield

In order to attempt to quantify sputter depth profiling, one must take into account the sputter yield. The sputter yield in SIMS/RIMS may be defined as the average number of sample atoms ejected per incident primary ion. The most successful model of the sputtering process was that of Sigmund's linear collision cascade model in 1969 [9] and is still the primary model used today. Sigmund based the sputtering process on a linear Boltzmann transport equation to describe the specific energy loss of a particle moving through a semi-infinite random medium. The model may be described as a hard sphere model as it disregards electronic interactions between the incident particles and the target atoms and it assumes that three important conditions are met; (1) sputtering is a form of erosion observed on a material surface as a direct result of particle bombardment, (2) sputtering takes place under low incident beam current to ensure that macroscopic heating leading to evaporation is excluded as a sputtering effect, (3) sputtering is observed under low incident particle fluence, such that single particle sputtering may be initiated. As such, it is appropriate to the case of static SIMS. However, since the model regards electronic sputtering as negligible, in the low energy (few keV) region, as used in static SIMS, electronic interactions between incident

particles and target atoms may not be negligible hence the hard sphere model may not be completely appropriate.

Within the keV region using normal incidence, Sigmund derived the following yield equation:

$$Y(E) = \Lambda \cdot F_D(E)$$ **Equation 2.4**

where $F_D(E)$ is the deposited energy at the surface, given by:

$$F_D(E) = \alpha \cdot N \cdot S_N(E)$$ **Equation 2.5**

and Λ is function of the density of target atoms, N, and the surface binding energy, U_s, and is given by:

$$\Lambda = \frac{3}{4\pi} \cdot \frac{1}{N \cdot C_0 \cdot U_s} = \frac{0.042}{N \cdot U_s}$$ **Equation 2.6**

$S_N(E)$ is the nuclear stopping cross-section, α is a function of the masses of the primary particle, M_1, and target, M_2, and U_s is the surface binding energy, usually taken to be equal to the sublimation energy of the target. These combine to give the following yield equation:

$$Y(E) = \frac{0.042}{U_s} \cdot \alpha \cdot S_N(E)$$ **Equation 2.7**

Within the range $0.5 < M_2/M_1 < 10$, α may be approximated by [10]:

$$\alpha = 0.3 \cdot \left(\frac{M_2}{M_1}\right)^{\frac{2}{3}}$$ **Equation 2.8**

Yamamura et al [11] expanded on this formalism and proposed a new empirical formula, which better represented the aggregate data on ion-induced sputter yields as a function of the energy of the incident ion for different ion-target combinations.

$$Y(E) = 0.042 \cdot \frac{Q(Z_2) \cdot \alpha^*}{U_s} \cdot \frac{S_N(E)}{1 + \Gamma \cdot k_e \cdot \varepsilon^{0.3}} \cdot \left[1 - \sqrt{\frac{E_{th}}{E}}\right]^s$$ **Equation 2.9**

where Q, E_{th}, Γ and s are fitting parameters of the equation, Z_2 is the atomic number of the target atom, α^* is an updated version of the ion-target mass function, α, described in Equation 2.8, and k_e is the Lindhard electronic stopping coefficient[12]. This evolved formula is used to determine the sputter yield of a specific matrix, which is then used to evaluate the sample erosion rate due to the ion beam in chapter 6.

2.3 Influences on Sputter Yield

As seen in Equation 2.9, there are many factors that influence the sputter yield associated with the primary ion properties and sample properties. Indeed, the process of sputtering will cause modification of the surface structure of the sample, in some cases altering the sputter yield substantially. Effects such as surface roughening and ripple formation are dependent on both the primary ion parameters and the sample characteristics and can greatly affect the sputter yield.

The way in which the sputter yield varies when primary ion beam parameters are changed are markedly different depending on the sample structure. Amorphous samples tend to show a fairly linear variation when the bombardment parameters are changed whereas crystalline samples have rather more specific requirements for the ultimate sputter yield. The next few sub-sections describe the relationship of sputter yield to variation in primary ion and sample conditions, e.g. mass, energy, angle of incidence and sample crystallinity.

2.3.1 Primary Ion Mass and Energy

When considering the effect of the mass of the primary ion versus sputter yield, it is the relative primary ion/target atom mass ratio that is all-important, as determined by the function α^* in Equation 2.9. The sputter yield tends to increase as the primary ion moves across the periodic table to a maximum at the noble gases. Since the noble gases are among the most commonly used primary ion sources, Figure 2.4 shows an example of how the sputter yield of silicon varies with varying primary ion mass and energy for the noble gases.

From the graph, it can be seen that the sputter yield increases with energy to a maximum then decreases again. The decrease in the sputter yield at higher energies is caused by the excessive depth, to which the primary ions penetrate and, consequently, the excessive distance the recoil atoms are required to travel to reach the surface.

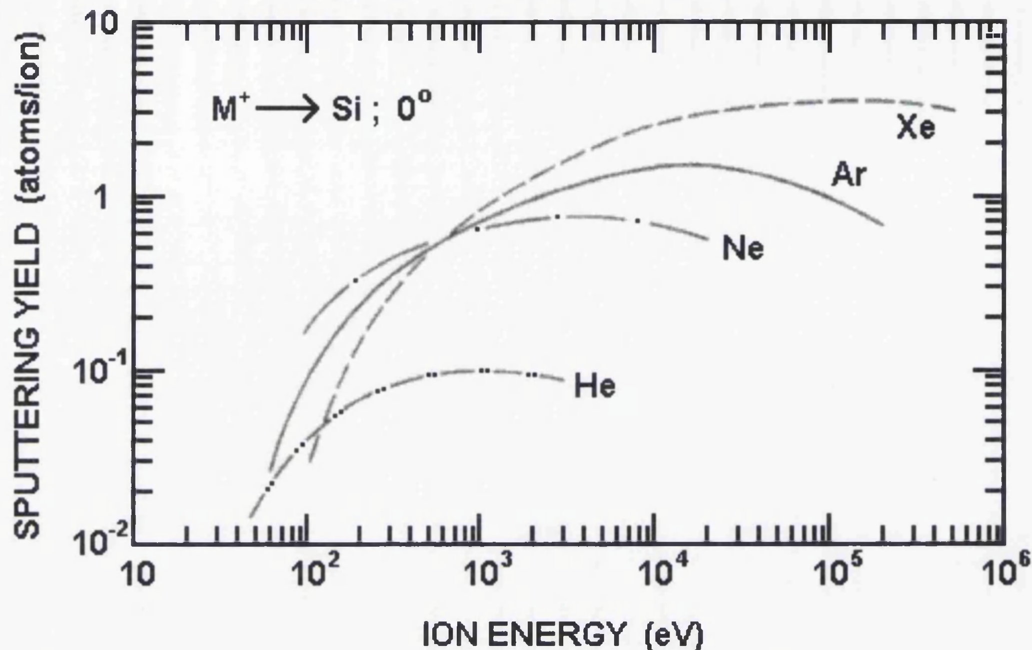

Figure 2.4: Variation of sputter yield as a function of ion mass and energy for noble gas species impacting a Si target at normal incidence [13].

At energies approximate to those in which the linear collision cascade occurs (several keV), the sputter yield is dependant on the primary ion mass while at energies below about 1keV, the sputter yield dependence is almost reversed. The results shown in Figure 2.4 were obtained with normally incident primary ions whereas the experimental set-up used for TOF-SIMS analysis in these studies was designed such that the primary ions intercepted the target at an angle of 35° to the normal. Consequently, simulations were undertaken using the SRIM-2003 2.0 program designed by Ziegler and Biersack [14] to investigate the variation of sputter yield with energy for various noble gases impacting a Ni target at 35° as shown in Figure 2.5.

The simulated sputter yield values at 35° show a very similar trend to those in Figure 2.4 indicating that the variation in angle of incidence between 0° and 35° does not influence the trend between the sputter yield and ion energy for different ion masses. However, both plots suggest that, at least for Si and Ni, the optimum primary ion energy range for efficient sputtering using Ar^+ is between 10-100keV. Ar^+ is one of the primary ions available for use in the TOF-SIMS system.

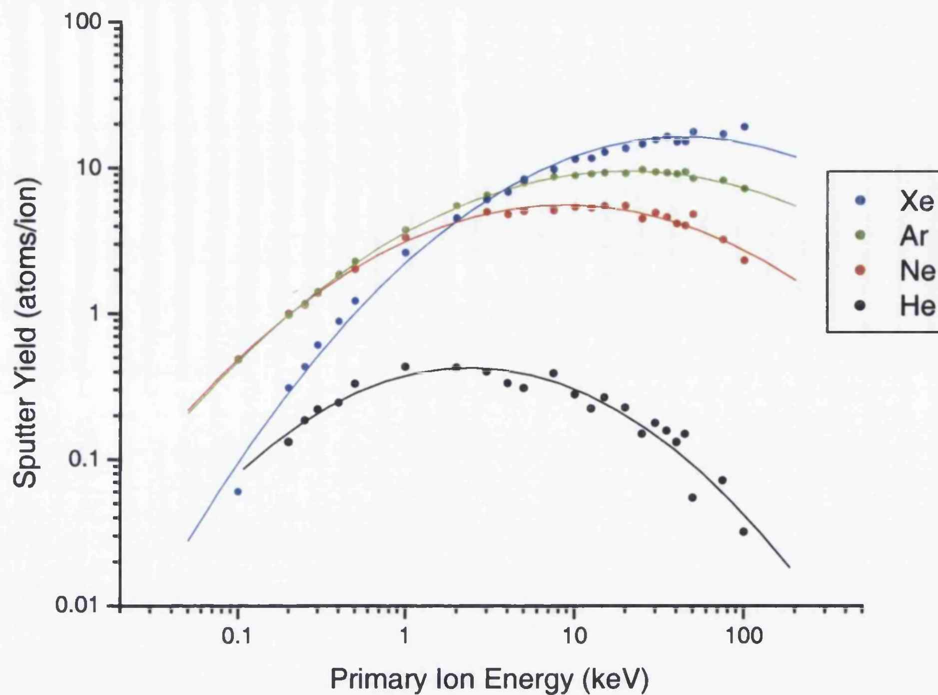

Figure 2.5: Variation of sputter yield as a function of primary ion energy for noble gas species impacting a Ni target at 35°.

2.3.2 Incidence angle of primary ions and sample properties

While the angle of incidence does not, in general, alter the trend in sputter yield as a function of primary ion energy, it does have a profound impact on the actual value of the sputter yield. Figure 2.6 shows an example of the angular dependence of the sputter yield.

From the plots, it can be seen that the sputter yield rises with increasing angle of incidence up to around 60-70° then falls off as the glancing incidence results in far less energy deposited in the sample. At impact angles below approximately 50°, the sputter yield typically follows a cosine-like dependence. The dependence of the sputter yield on primary ion energy can once again be observed in Figure 2.6 (a).

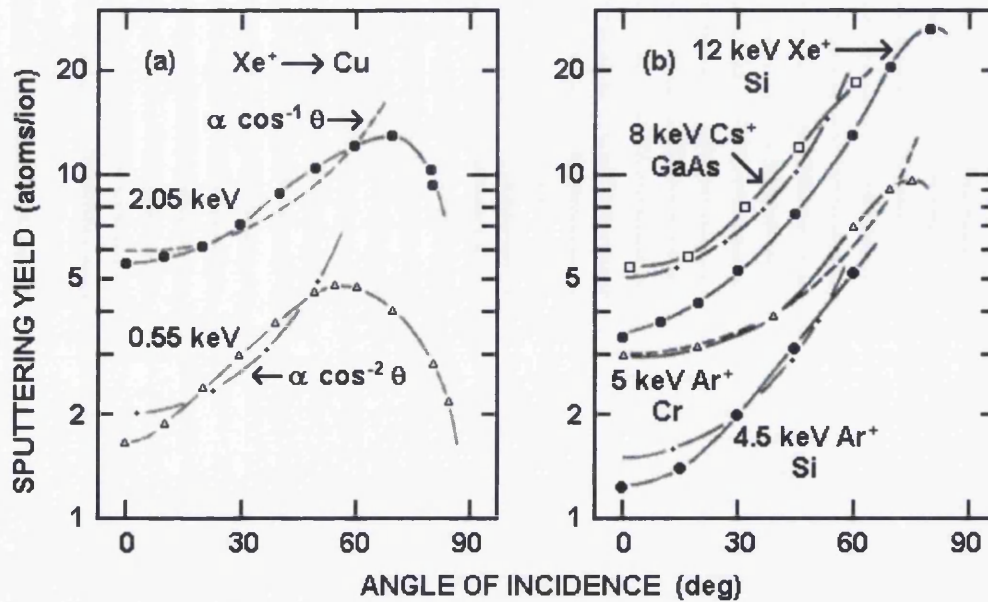

Figure 2.6: Variation of sputter yield as a function of incidence angle. (a) represents Xe^+ bombardment of Cu at two different energies[15], (b) represents a variety of ion-target combinations at different energies[13].

Crystalline samples that exhibit a regular structure and preserve it under ion bombardment reveal a very different dependence between sputter yield and bombarding ion energy and angle of incidence compared to amorphous samples. The disparity is often described in terms of channelling and transparency. Orientation of the lattice determines the amount of energy deposited at the surface of the sample. If the incoming ions are incident at an angle parallel to the lattice rows, only the top layer will be exposed since the atoms in subsequent layers will be shadowed. Consequently, much of the ion beam is channelled down the lattice rows with only a small fraction contributing to sputtering (that of the top layer), hence the sputter yield at this angle is reduced. An example of the angular dependence is shown in Figure 2.7, while an example of the energy dependence of the sputter yield for three different orientations is shown in Figure 2.8. From the graphs, it can be seen that the maximum sputter yield is achieved in the linear collision cascade region with the polycrystalline maximum at the upper end of this regime. It can also be seen that the sputter yield is greatest for the (111) surface due to the closely packed nature of this orientation as viewed along the axis of the ion beam, while the most openly packed orientation, that of the (110) surface shows the least yield.

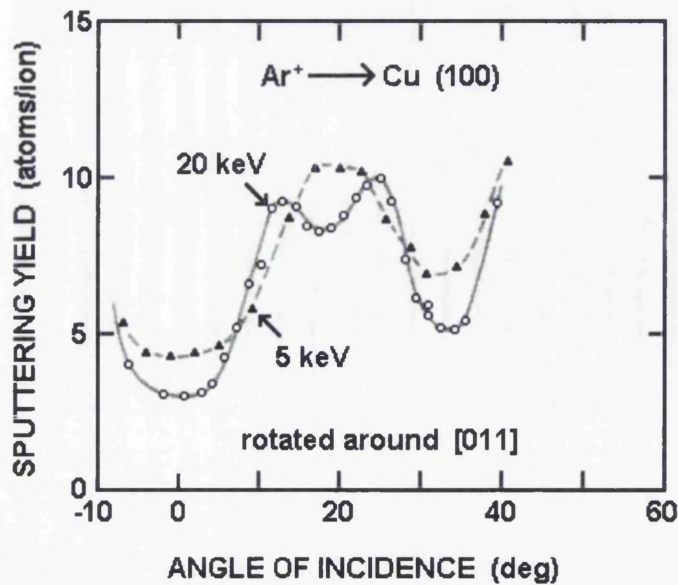

Figure 2.7: Variation of sputter yield as a function of angle of incidence for Ar^+ bombardment of a crystalline Cu target [16].

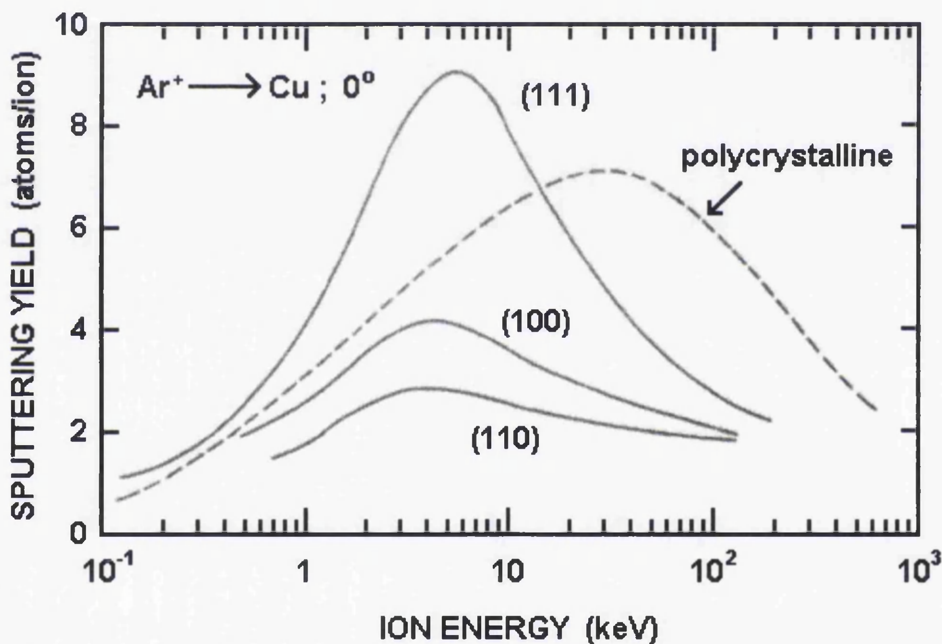

Figure 2.8: Variation of sputter yield as a function of Ar^+ primary ion energy for three primary crystallographic orientations of a Cu target [17].

By its very nature of multi-oriented grains, the magnitude of the sputter yield of the polycrystalline sample lies between these orientations within the 1-10keV energy range and peaks at ~30keV, while the sputter yield of the single orientation surfaces rapidly decreases. This is again primarily due to channelling effects and the associated depth to which the incident primary ion can penetrate within the sample. An important factor is that the variation of sputter yields with crystal orientation will cause a disparity in the erosion rate of one surface grain to the next. Consequently, this will result in substantial roughening of the surface following ion bombardment. The level of roughening will

naturally depend on the degree of orientation variation of the individual grains comprising the surface and sub-surface structure.

2.4 Properties of sputtered particles

When an ion beam is incident on a target sample, a host of species are emitted from the surface. Included in this array of species are backscattered primary ions but it is the species that are sputtered from the sample surface that are of interest. These species consist of ionised atoms, neutral atoms, molecules and clusters and all are emitted with a distribution of energies and trajectories.

2.4.1 Energy and angular distribution

If the geometry of the interaction between the incident ion and the target is considered, an atom sputtered from the target surface at an angle θ, with energy E_{sp} is ejected into a solid angle $d\Omega$, as shown in Figure 2.9.

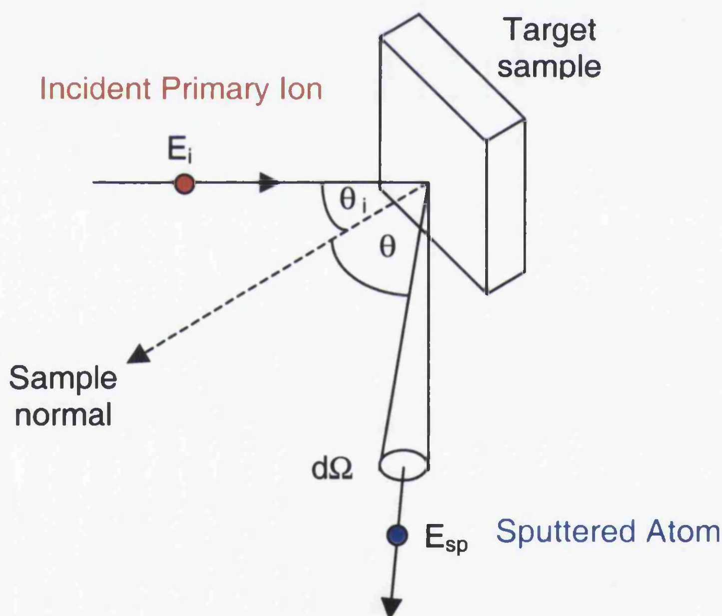

Figure 2.9: Diagram of intersection between primary ion and target sample and emission trajectory of sputtered atom.

In order for the atom to be sputtered, as shown in Figure 2.9, it must overcome the surface binding forces. In such a situation, the kinetic energy of the sputtered atom, E_{sp}, is given by:

$$E_{sp} = E_i - U_s$$ **Equation 2.10**

where E_i is the kinetic energy of the atom just prior to ejection from the surface and U_s is the surface binding energy (assumed to be planar). The surface binding energy is a difficult quantity to measure and is indeed only known for a few materials. In most experiments and computer simulation programs such as SRIM, the heat of sublimation is taken to be a good approximation.

Using the Sigmund-Thompson distribution,[18] derived from the linear collision cascade theory, the differential yield of the sputtered atoms as a function of energy and angle is given by:

$$\frac{d^3Y}{dE_{sp} \cdot d^2\Omega} \propto \frac{E_{sp}}{(E_{sp} + U_s)^{3-2m}} \cdot \left|\cos^n \theta\right| \qquad \textbf{Equation 2.11}$$

where m is an energy dependent parameter taken between 0 and 1, while n is taken between 1 and 2 depending on primary ion parameters. Experimental measurements[19] have determined that the exponent n is dependent on the primary ion energy as shown in Table 2.1:

Low energy, sub-keV range	n < 1
Low keV range	n = 1
High keV and above range	1 < n <2

Table 2.1: Variation of exponent n for different energy ranges.

2.4.2 Sputtering into charged and excited states

Neutral atoms usually account for the majority of particles sputtered during ion beam bombardment (up to 99% in certain cases) and the fraction of neutral atoms emitted is dependent on the ionisation probability of the species in question. However, not all sputtered atoms remain in the ground state. Indeed, the neutrals may be sputtered with a whole range of excited electronic states with the distribution of atoms in each state very much dependent on the composition of the sample under investigation. This forms the basis of the RIMS studies and will be discussed further in chapter 3.

2.4.3 Ionisation probability and secondary ion emission

In the case of SIMS experiments, it is the ionic portion of the sputtered material that represents the useful secondary yield for analysis, the neutral material being rejected into the surrounding components. However, the ionic portion within the sputtered population is usually very small, typically <1% of the total emitted species for most metals. An example of an exception to this is sputtering of a group 1 metal such as sodium using a positive primary ion source where the ionic contribution is actually greater than the neutral contribution. Oxygen is sometimes used in sputtering experiments as it can increase the secondary ion yield by several orders of magnitude[20,21].

For simple quantitative analysis, equation 2.1 can be simplified to:

$$I_s^m = K_m \cdot \theta_m \cdot I_p \qquad \textbf{Equation 2.12}$$

where K_m is a factor dependent on the elemental variables described in Equation 2.1. However, where high accuracy is required in SIMS (and indeed RIMS), all variables within equation 2.1 must be considered. In general, it is the ionisation probability that has the greatest influence on SIMS analysis, since the probability of a target atom becoming ionised by the collision cascade is very much dependent on the ionisation efficiency of the species in question. As mentioned previously, group 1 elements are particularly easy to ionise with a positively charge primary ion source, whereas noble gases have a very low ionisation efficiency, sometimes up to 7 orders of magnitude lower for a specific matrix. Typical ionisation efficiencies for positive and negative atomic ions sputtered from ion implanted Si and GaAs have been produced by Wilson et al.[22] Generally, the ionisation efficiency can be related to the ionisation potentials or electron affinities in most cases although there is no straightforward relationship as such.

In addition, the ionisation probability for a specific element can vary by several orders of magnitude from sample to sample. This is known as the matrix effect and is the single most obstructive factor in the quantitative SIMS analysis of sample concentration. With the lack of a complete and definitive theory to describe the matrix dependent ionisation probability, the most common method of concentration

quantification in SIMS is the use of highly accurate material standards to compare the secondary ion signals with. However, in the case of layered samples with non-discrete mixed phase interfaces, quantification becomes extraordinarily difficult. Such samples require a high level of pre-knowledge regarding the matrices present as a function of location within the interface. However, changes in a matrix and the ion yield are useful indicators of a reaction within layered material systems, yielding information on the location of compositional changes as a function of depth.

2.5 Depth Profiling

Depth profiling makes use of the destructive nature of ion bombardment to produce a profile that displays sample composition as a function of the thickness of material eroded. It has been used in a wide variety of applications such as biological, geological, metallurgical and superconductor analysis. However, by far the most widespread use of depth profiling has been in the field of semiconductor analysis in dopant depth profiling, whereby the high sensitivity and good depth resolution permit the identification of dopants within a semiconductor sample as a function of depth.

It should be noted that exact determination of the concentration of atomic and molecular species within a sample is complicated by the matrix effect inherent to SIMS analysis. The efficiency with which a particular species is sputtered, for constant ion beam conditions, is very much dependent on the target matrix under analysis. A target surface may also be roughened by the effect of ion bombardment thus altering the sputter yield. Many methods are employed to reduce the effect of roughening such as the use of a low energy ion beam at normal incidence. Where non-normal incidence is used, the technique of oxygen flooding the sample surface serves both to inhibit roughening and enhance the secondary ion yield, although the benefit is outweighed if the sample is particularly reactive to oxygen.

Consequently, any attempt at quantification of concentration requires precise knowledge of the target sample structure and all matrices therein and reference to standard samples with compositions as close as possible to the matrix compositions in question. This makes SIMS quantification particularly difficult, particularly when the interface between two layers is not discrete but consists of a multi-component matrix. However, a great deal of information can be gained from analysis of the variation of component species within the profile. For example, in layered samples, the thickness of the

interfaces between the layers can be determined with a large degree of confidence. Successful depth profiling of a target requires careful consideration of multiple factors before proceeding, with the ultimate aim being the optimisation of depth resolution.

2.5.1 Depth Resolution

Depth resolution is defined as the ability to resolve an abrupt feature as a function of depth, e.g. an abrupt interface in a layered sample. A recommended definition is the distance between the 84% and 16% levels of the depth profile of an element in a perfect-layered sample with an infinitesimally small overlap of the components [23]. In order to achieve maximum depth resolution, it is required that a flat-bottomed crater is eroded in the target. The secondary ion information used to produce mass spectra to build up the depth profile is obtained from the centre of this crater. Modern instrumentation uses a finely focused ion beam that is swept in a raster scan pattern to erode a square, or rectangular, area.

2.6 Influences on Depth Resolution

Since the interaction of energetic ions incident on a target sample causes recoiling atoms to be set in motion, the depth resolution of a system is related to the magnitude of relocation induced by the incident ions. This is generally known as ion intermixing or collisional mixing. Therefore, the depth resolution of a profile is dependent on the incident ion parameters as well as the sample characteristics. These will determine the mean path length of the primary ions within the sample and the post-collisional kinetics of target atoms and hence the number of atoms that can be set in motion.

The Stopping and Range of Ions in Matter program, SRIM, formerly known as TRIM, designed by Ziegler and Biersack [14], is a most useful tool for simulating the interaction of a specific primary ion with a specific target. SRIM considers the ion mass, energy and angle of incidence and the target mass, density, state of matter, displacement energy, lattice binding energy and surface binding energy when programming the primary ion parameters and uses the linear collision cascade model to determine the distribution of ions within the target and the sputter yields of target.

2.6.1 Primary Ion Mass Vs Range

The mass of the primary ion used for depth profiling itself is less important than its relative mass compared to that of the target atoms. Through conservation of momentum and energy, a light primary ion will tend to undergo significant angular deflection following collision with substantially heavier target atoms. Consequently, the mean path length of the primary ion within the target medium will be greater than that of a heavier primary ion and as such are capable of implanting far deeper into the medium. However, due to this excessive path length, it will be capable of colliding with a far greater spatial range of target atoms, including those buried deep beneath the surface. As a result, depth resolution will be less than ideal. Conversely, an excessively heavy primary ion will tend to come to rest very quickly after imparting its energy to a small number of target atoms. These target atoms will have substantial energy and will proceed to collide with many other target atoms. Therefore, depth resolution may again be reduced from its optimum, via knock-on of target atoms. Figure 2.10 shows the projected mean path lengths as a function of primary ion mass relative to the mass of a Ni target obtained using SRIM-2003.2.0 [14] to perform simulations.

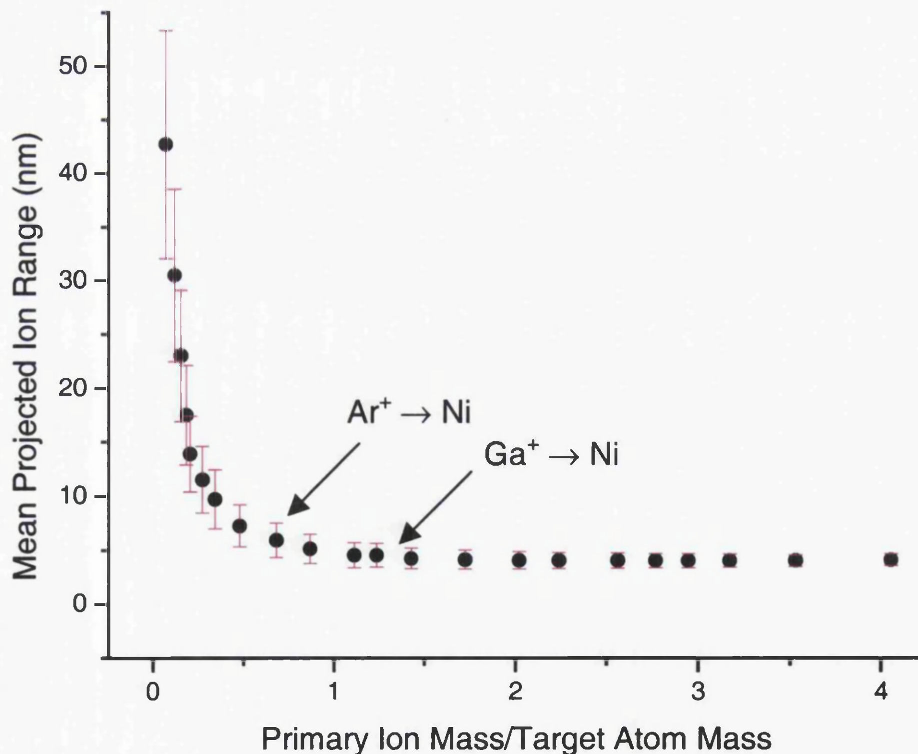

Figure 2.10: Plot of the mean projected ion range as a function of primary ion mass/target atom mass for random primary ion projectiles normally incident on a Ni target at 10keV, simulated using SRIM-2003.2.0 [14].

From the graph, the effect of primary ion mass on the projected ion range is quite clear. As the mass ratio of the primary ion to target atom approaches unity from zero, the mean projected ion range rapidly decreases and levels off over the remaining range. However, it is not merely the depth to which the primary ion is implanted that is of importance. The action of the recoiling atoms set in motion by the primary ion collisions is also crucial. Figure 2.11 shows the effect of primary ion mass for various noble gases striking a Ni target.

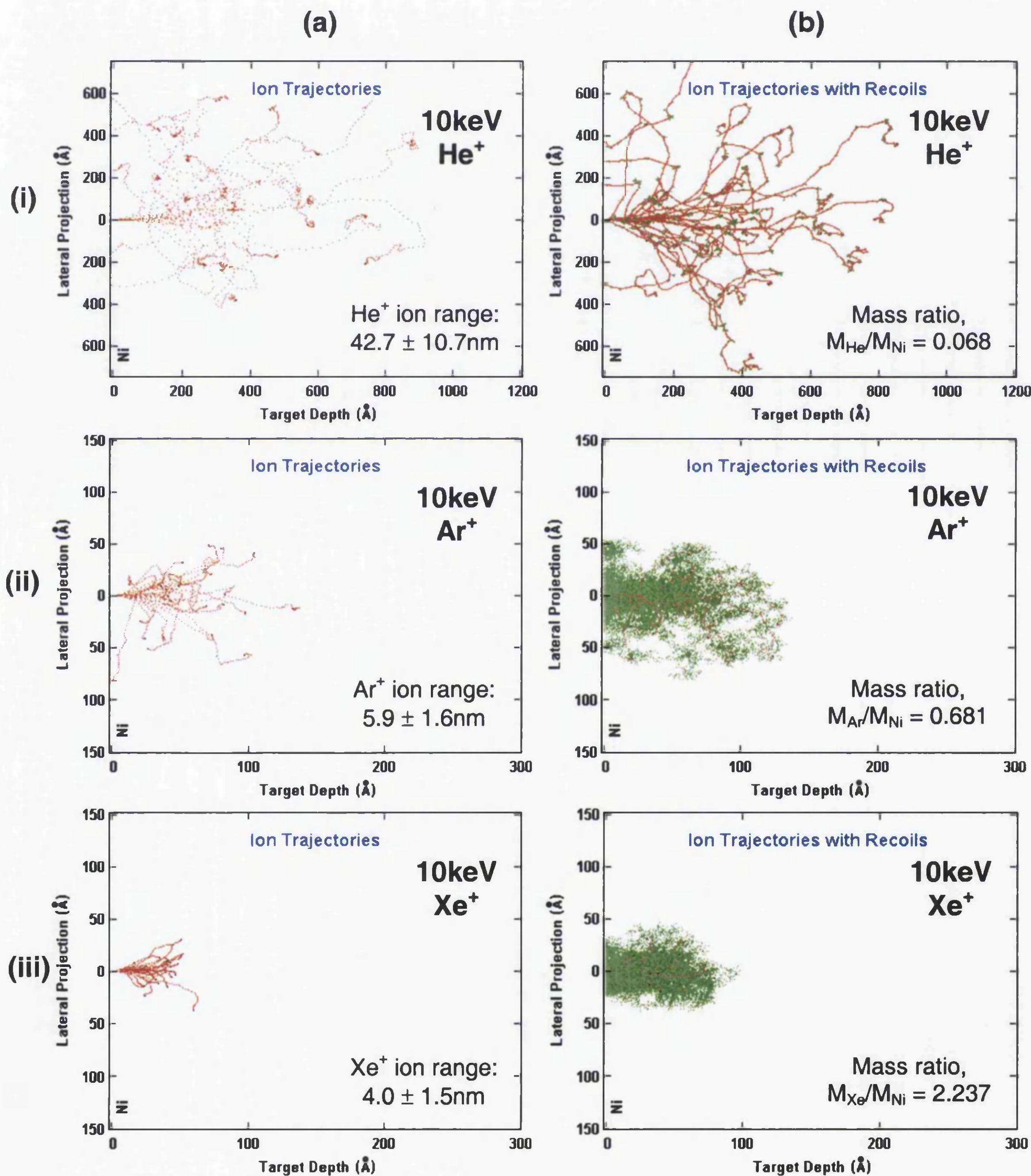

Figure 2.11: Simulations demonstrating the effect of primary ion mass for 25 (i) He^+, (ii) Ar^+ and (iii) Xe^+ ions (all 10keV) striking a Ni target at normal incidence. (a) represents comparison of projected mean ion ranges, (b) represents ion trajectories with associated recoils to show the scale of ion-target interaction. Simulations performed using SRIM-2003.2.0 [14].

The simulations demonstrate that very light ions such as He^+, in addition to having very long path lengths before coming to rest, also set very few recoil atoms in motion. Of the two remaining primary ion species, the heavier Xe^+ ion appears to possess the greatest potential for optimum depth resolution. However, this only holds true where the target medium consists of atoms of similar mass such that subsequent collisions between recoil atoms distribute the collisional energy in approximately equal amounts. In the case of multi-layered samples, whereby alternating layers may be composed of species of greatly differing mass, the heavy primary ion will cause substantial inter-diffusion at the interfaces between the two species. In such cases, it is advantageous to use a primary ion of similar mass to both species. In most situations, there are other factors that are taken into account when choosing a primary ion. It is desirable to use a substance that has very few associated isotopes. Preferably the source should be mono-isotopic, such that a Wien filter is not required for isotope selection. Expense is also a factor, rare gases inherently cost more and this must be offset against the rate of consumption.

Cluster ion sources can often generate substantial secondary ion yields enhancements in comparison to atomic ion sources. A recent addition to the array of ion sources available is the buckminsterfullerene C_{60}^+ cluster beam source, whose high mass offers good depth resolution potential. C_{60}^+ sources are becoming more widely available and the benefits are currently under investigation.[24]

2.6.2 Primary Ion Energy Vs Range

As with the species used, the primary ion energy directly affects the range to which the ions penetrate into the target sample. Naturally, a low energy ion will not cause as much damage to the target as a higher energy ion. Indeed, much work has been undertaken that demonstrates enhanced depth resolution using low energy (typically sub-keV) depth profiling[25,26,27]. The lower energy used typically reduces the level of intermixing that occurs although it is also associated with an increase in surface roughening of the target. Surface roughening leads to irregular and generally reduced sputter yield. Consequently, a balance is required between ultimate depth resolution and consistent secondary ion production.

2.6.3 Incidence angle of primary ions

The angle at which the primary ions are incident on the target can be linked with ion energy since the energy deposited normal to the target surface by the primary ion is naturally lower than the total ion energy if non-normal incidence occurs. Therefore, using non-normal angles of incidence will result in a lower mean ion range perpendicular to the target surface. This is useful if a minimum primary ion energy is required for the ions to reach the target surface. However, ions incident at non-normal angles cause roughening of the target surface to occur with the magnitude of roughening proportional to the magnitude of the angle from the normal.

2.7 Summary

Optimum depth resolution for SIMS depth profiling has been found to require a minimum altered layer thickness by using the lowest primary ion energy possible, a normal angle of incidence and the highest mass primary ion[28], preferably a noble gas. However, an element of compromise must be sought when selecting the optimum parameters, with the properties of the target sample when exposed to ion bombardment a key factor to consider. The interaction of a primary ion beam with a sample will tend to roughen the surface, particularly if the ions are incident at an angle to the surface. Normal incidence obviously limits this to an extent, but normal incidence reduces the sputter yield efficiency and may not always be practical to use in reality and while methods such as oxygen flooding have benefits in terms of roughening inhibition, it is hampered when a reactive sample is used. Consequently, the compromise must consider the efficiency of the sputter ion process and the predicted depth resolution that is achievable in terms of primary ion parameters and sample properties.

2.8 References

[1] A. Benninghoven, Z. Physik **230,** 403 (1970).

[2] J.C Vickerman, A.J. Swift in *Surface Analysis-The Principle Techniques* (Ed. J.C. Vickerman) Wiley 137 (1997).

[3] W.L. Grove, Phil. Mag. **5**, 203 (1853).

[4] J.J. Thomson, Phil. Mag. **20,** 252 (1910).

[5] L.G. Glazov, P. Sigmund, Nucl. Instrum. Meth. **B207,** 240 (2003).

[6] J. Lindhard, V. Nielsen, M. Scharff, P.V. Thomsen, Mat. Fys. Medd. Dan. Vid. Selsk. **33** (10), 1 (1963).

[7] J. Lindhard, M. Scharff, H.E. Schiøtt, Mat. Fys. Medd. Dan. Vid. Selsk. **33** (14), 1 (1963).

[8] H.A. Bethe, Ann. D. Physik **5,** 325 (1930).

[9] P. Sigmund, Phys. Rev. **184,** 383 (1969).

[10] J. Bodhansky, Nucl. Instrum. Meth. **B2,** 587 (1984).

[11] Y. Yamamura, H. Tarawa, Atomic Data and Nuclear Data Tables **62,** 149 (1996).

[12] J. Lindhard, M. Scharff, Phys. Rev. **124,** 128 (1961).

[13] K. Wittmaack in *Practical Surface Analysis* 2nd Edition, Volume 2 – Ion and Neutral Spectroscopy (Ed. D. Briggs, M.P. Seah) Wiley 112 (1992).

[14] J.F. Ziegler, J.P. Biersack, The Stopping and Range of Ions in Matter Version SRIM-2003.2.0.

[15] H. Oeschner, Z. Phys. **261,** 37 (1973).

[16] D. Onderdelinden, Can. J. Phys. **46,** 739 (1968).

[17] H.E. Roosendaal, in *Sputtering by Particle Bombardment* (Ed. R. Behrisch), Vol. 1, Topics in Applied Physics Vol. 47, p.219, Springer, Berlin (1981).

[18] M. Thompson, Phil. Mag. **18,** 377 (1968).

[19] G. Betz, K. Wien, Int. J. Mass Spectrom. Ion Proc **140,** 1 (1994).

[20] A. Benninghoven, Surf. Sci. **35,** 427 (1973).

[21] A. Benninghoven, Surf. Sci. **53,** 596 (1975).

[22] R.G. Wilson, F.A. Stevie, C.W. Magee, *Secondary Ion Mass Spectrometry: A Practical Handbook for Depth Profiling and Impurity Analysis*, Wiley, New York (1989).

[23] IUPAC Compendium of Chemical Terminology, 2nd Ed. (1997).

[24] S. Sun, C. Szakal, E.J. Smiley, Z. Postawa, A. Wucher, B.J. Garrison, N. Winograd, Appl. Surf. Sci. **231-232,** 64 (2004).

[25] R. Liu, C.M. Ng, A.T.S. Wee, Appl. Surf. Sci. **203-204,** 256 (2003).

[26] T.J. Ormsby, D.P. Chu, M.G. Dowsett, G.A. Cooke, S.B. Patel, Appl. Surf. Sci. **144-145,** 292 (1999).

[27] M.G. Dowsett, Appl. Surf. Sci. **203-204,** 5 (2003).

[28] S. Oswald, S. Baunack, Thin Solid Films **425,** 9 (2003).

Chapter 3: Theory of RIMS

3.1 Introduction to RIMS

Resonance ionisation spectroscopy (RIS), from which resonant ionisation mass spectrometry (RIMS) is derived, is a technique that uses one or more lasers to achieve highly selective ionisation of atoms. RIS differs from traditional ionisation techniques that use x-rays, electrons, ions or α particles to ionise atoms via "brute force", in that it uses multiple photon absorption processes to promote electrons via higher states to the ionisation continuum. RIMS itself is an evolution of the SIMS technique whereby the species to be studied are sputtered from the sample under analysis by the interaction of a primary ion beam. However, RIMS analyses the secondary neutral species sputtered from the sample, as opposed to the secondary ions used for SIMS analysis, by post-ionisation via laser interaction.

The selectivity of the RIS process enables RIMS to overcome to a large degree the matrix effect, which afflicts SIMS analysis, and it offers the ability to consider the nature of bonding within a sample and discriminate between different alloy regions. The sample system of Ni contacts to SiC is one in which this technique can readily be applied. This chapter will introduce the concept of RIMS, also known as SNMS (Sputtered Neutral Mass Spectrometry), and discuss in detail its application to the Ni/SiC contacts.

3.2 Resonant Multi-Photon Ionisation (RMPI)

Resonant multi-photon ionisation (RMPI) was first employed for SNMS by Winograd et al [1], whereby each photon used in this technique has an energy that is insufficient to directly ionise an atom, otherwise the selectivity of the process would be lost. Hence one photon is used to elevate the electron to an excited level while further photons may be used as required to pump additional transitions with the final photon used to promote the electron to the ionisation continuum. A situation where one laser is used to ionise an atom via two photons is called a one-colour, two-step scheme shown in Figure 3.1 (a). Many atoms may be ionised in this way, whereby photons of the same energy are used to resonantly excite and ionise the atom. In many cases, the final transition to the ionisation continuum may not be a resonant transition, hence the reason why most atoms can be ionised via a two-step scheme. The use of resonant intermediate

transitions, with associated high cross-sections, enables saturation of many, or all, of the steps at reasonably moderate laser intensities (of the order of 10^8 W.cm^{-2}).

The process of RMPI is particularly sensitive and the photo-ionisation routines are applicable to atoms in a metastable excited state configuration as well as the ground state. However, the efficiency of the process is determined by the relative population of the initial state in question. Another limitation is that additional laser systems are generally required if analysis of multiple species is required. A second laser system can also be used if a two-colour ionisation scheme is required. This arrangement permits enhanced selectivity by choosing schemes particularly specific to the species under analysis. A general two-colour, three-step ionisation scheme is shown in Figure 3.1 (b).

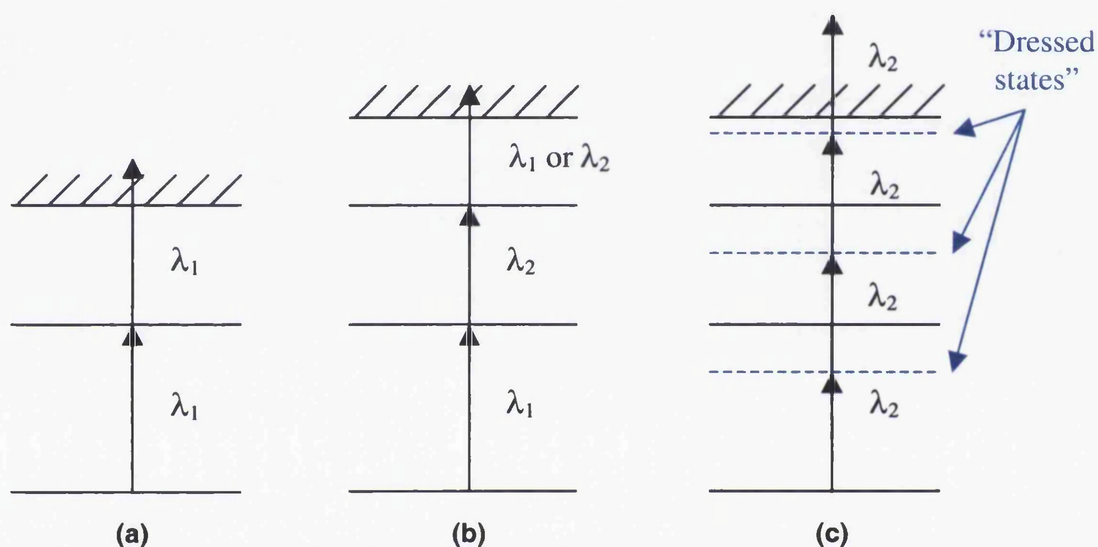

Figure 3.1: Typical ionisation schemes (a) resonant one-colour, two-step ionisation scheme, (b) resonant two-colour, three-step ionisation scheme, (c) non-resonant multi-photon ionisation scheme. The dashed lines in (c) represent "dressed states".

3.3 Non-Resonant Multi-Photon Ionisation (NRMPI)

Non-resonant multi-photon ionisation is a process that can occur as a result of an intense photon field to generate "dressed" states. Consequently, atoms or molecules within the photon field may absorb several photons at once leading to ionisation. The photon-dressed ground state is often addressed as a virtual energy level. An example of this is shown in Figure 3.1(c). Non-resonant MPI can naturally reduce selectivity of the ionisation process although it can be useful where multiple species ionisations are desirable with a single laser source.

3.4 Ionisation scheme considerations

When performing resonant ionisation experiments, it is necessary to select an appropriate ionisation scheme that balances selectivity with sufficient probability of photo-ionisation for a particular population of atoms. In the case of the excitation step(s), simply tuning a laser to a wavelength corresponding to the energy difference between the initial state and any intermediate metastable state is not always sufficient, or feasible. In spectroscopy, the polyelectronic atomic state is denoted $^{2S+1}L_J^{\pi}$ where L is the orbital angular momentum, S is the spin angular momentum, J is the total angular momentum, and π is the parity of the atomic state. Odd parity is represented by a symbol o, while even parity has no symbol. Quantum selection rules regarding angular momenta and parity should be considered for efficient excitation. In the case of the ionisation step, it is advantageous that the step terminates in an autoionising state to increase the efficiency of the ionisation process.

Autoionising States

An autoionising state is a bound atomic state lying above the first ionisation limit. These states are typically formed when two electrons are simultaneously excited, or a single electron from an inner shell is excited resulting in bound states with energies ≥ ionisation continuum states. The atom can then either decay radiatively or into a continuum state of equal energy and parity. Autoionising states have the advantage of a dramatically enhanced cross-section (often comparable to that of bound state transitions), when compared to non-resonant steps into the ionisation continuum and they allow increased selectivity of the ionisation scheme with the addition of another resonant step.

3.5 Saturation conditions for the resonant ionisation process

Efficient photo-ionisation of an atom or molecule is most successfully obtained when both the excitation step(s) and ionisation step are saturated, i.e. all atoms within the laser photon field are excited and photo-ionised. In order to describe a simple two-step ionisation process theoretically demands that a complete quantum mechanical analysis is carried out. However, the density matrix formalism can be simplified to a rate equation method if the laser system used satisfies the requirement that a sufficiently precise interaction between the ionisation system and the laser photon field occurs [2].

3.5.1 Rate Equations

The simplest method is to consider a two-step ionisation process as shown in Figure 3.2, which is relevant to the work undertaken in these studies. $N_1(t)$ is taken to be the number of atoms present in the initial state (typically the ground state but it could be any low-lying metastable state) as a function of time throughout the photon field interaction. $N_2(t)$ represents the equivalent number of atoms in the intermediate step with identical degeneracy to the initial state. $N_i(t)$ denotes the number of atoms that undergo ionisation. The photon flux, denoted by Φ_{12}, represents the number of photons passing though a unit area per unit time.

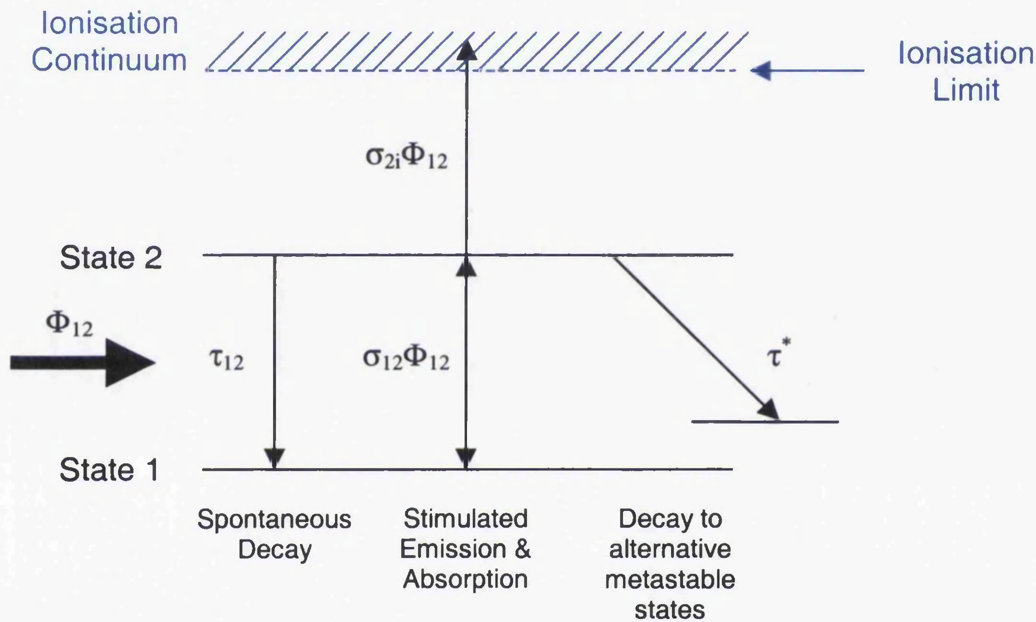

Figure 3.2: Diagram showing general processes that can occur during resonant ionisation.

There are four processes that normally occur for an atom in the intermediate state 2 to leave this state. Decay to state 1 can occur through spontaneous decay a rate denoted by τ_{12}, and through stimulated emission with a cross-section σ_{12}. Absorption of a photon can promote the electron to the ionisation continuum, thus ionising the atom with a cross-section σ_{2i} for this process. The final process, representing a loss mechanism, which can occur, is the decay to a metastable state, other than the initial state. This process takes place through various means, the rate of which is taken as τ^*.

By considering the rate at which the states are populated and de-populated, the following rate equations can be formulated:

$$\frac{dN_1(t)}{dt} = \tau_{12} \cdot N_2 - \sigma_{12} \cdot \Phi_{12} \cdot N_1 + \sigma_{12} \cdot \Phi_{12} \cdot N_2$$ **Equation 3.1**

$$\frac{dN_2(t)}{dt} = -\tau_{12} \cdot N_2 + \sigma_{12} \cdot \Phi_{12} \cdot N_1 - \sigma_{12} \cdot \Phi_{12} \cdot N_2 - \sigma_{2i} \cdot \Phi_{12} \cdot N_2 - \tau^* \cdot N_2$$ **Equation 3.2**

$$\frac{dN_i(t)}{dt} = \sigma_{2i} \cdot \Phi_{12} \cdot N_2$$ **Equation 3.3**

If the lifetime of the intermediate state 2 is assumed to be sufficiently long, a practically achievable situation, then decay to other metastable states and spontaneous emission can be neglected, permitting the absorption and stimulated emission processes to dominate. If the photon flux is also sufficiently high, quasi-equilibrium conditions are set up between state 1 and state 2 during the laser pulse.

Thus, when these conditions are fulfilled, the number of ionised atoms within a given time, T, is given by:

$$N_i = \int_0^T \sigma_{2i} \cdot \Phi_{12} \cdot N_2(t) \cdot dt = \frac{\sigma_i \cdot \Phi_{12} \cdot N_1}{\sigma_i \cdot \Phi_{12} + \tau^*} \cdot \left[1 - \exp(-0.5 \cdot \left(\sigma_i \cdot \Phi_{12} + \tau^*\right) \cdot T\right]$$ **Equation 3.4**

In order to obtain saturation of the resonant ionisation process at the end of the laser pulse, two conditions must be satisfied, the so-called flux condition and fluence condition. The flux condition dictates that the rate of photo-ionisation should be much greater than the rate of irreversible losses:

$$\sigma_{2i} \cdot \Phi_{12} >> \tau^*$$ **Equation 3.5**

while the fluence conditions states that:

$$\sigma_{2i} \cdot \phi >> 1$$ **Equation 3.6**

where ϕ represents the photon fluence, defined as the number of photons per laser pulse per unit area. If these conditions are satisfied, all atoms present in the initial state 1 are

photo-ionised within a sufficiently long laser pulse. The fluence condition is more difficult to achieve owing to the low cross-section for ionisation (~ 10^{-18} cm^2). However, the use of autoionising states permits an increase of this cross-section to a much higher value. Indeed, cross-sections of ~ 10^{-15} cm^2 are achievable.

3.6 Determination of nickel-silicon bonding using RIMS

Quantification of nickel-silicon bonding using RIMS is not merely as simple as selecting one wavelength to resonantly ionise Ni, and another to ionise Si, and then comparing the signal intensities. Even if saturation conditions are met for both cases, the matrix effect still has an effect where multiple matrices are involved since sputter yields of the components will vary, thus the relative populations measured are sputter yield dependent. Therefore, a more subtle method is required. The method used in these studies is based on the number of atoms in a particular electronic state and the associated velocity distribution of the atoms in each of these states and how these vary for different nickel-silicon compounds.

The RIMS measurements in this thesis build on the work undertaken by Vandeweert[3,4] and Bastiaansen[5], who investigated the population partitions and velocity distributions of pure Ni and Ni-silicides. Since the population partition of individual electronic states and velocity distributions of each of these states is unique for pure Ni and the individual Ni-silicides, a method of discriminating between bonding states is established.

3.6.1 Population Partitions

The population partition of an ensemble of atoms describes the number of atoms present in each of the atomic states. It is generally taken relative to the ground state population, which itself is set to unity. The origin of the population of Ni atomic states can be described by the resonance electron transfer (RET) model [6,7]. The metal is assumed to consist of ions surrounded by delocalised electrons occupying the metal valence band states. An incident particle setting up a collision cascade permits particles to escape from the surface. These particles that are initially in the same charge state as in the solid may be neutralised by electrons, which evolve from metallic band states to atomic states. The population probability of specific atomic states is principally determined by the bulk metal properties, e.g. bulk band structure and Fermi level position. Indeed, atomic states with electron wavefunctions similar to those of metal valence band electrons are strongly broadened as a result of higher coupling strength. There is a

decrease in the overlap between the metallic and atomic wavefunctions with increasing distance from the metal surface hence electrons from the metal preferentially populate atomic states with a bulk-type electron configuration.

Population partition experiments have been undertaken on Ni [3,4,8] and a variety of Ni silicides[5] using a continuous ion beam to sputter material and a two-colour, two-step resonance process to ionise the atoms within the laser field. The experiments used two laser systems, one tuned to provide the excitation step to a sufficiently long lifetime intermediate state and a second tuned to the wavelength required to ionise atoms out of this intermediate state. Use of the same intermediate state and hence second laser wavelength in all experiments on the same target meant that, as long as the first excitation step was saturated, the ion signal detected represented the relative population of the initial state probed each time. It also meant that the ionisation step could be tuned to an autoionising state to enhance the ionisation efficiency. In addition, use of the same intermediate state required that only the wavelength of the laser tuned to provide the excitation step needed adjustment for each initial state. A simplified ionisation scheme for obtaining population partitions is shown in Figure 3.3.

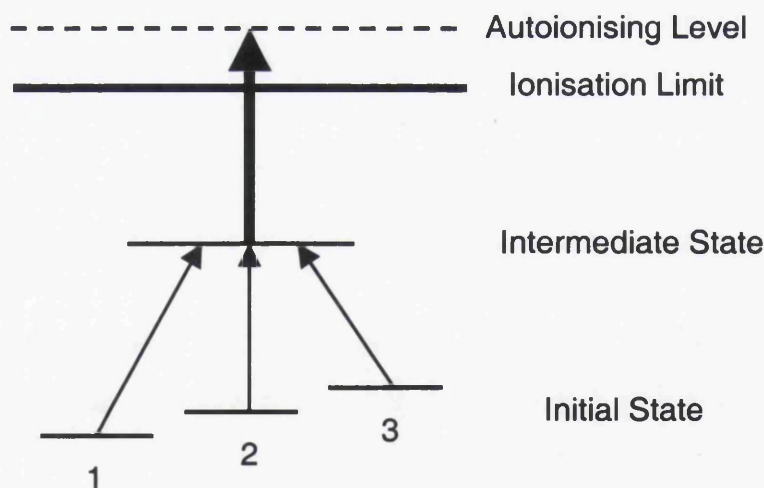

Figure 3.3: Schematic diagram representing method of acquiring population partitions of multiple metastable states.

The results obtained on pure Ni and Ni-silicides proved that the majority of atoms in these samples are sputtered in the ground and lower lying metastable states with the a^3D_3 yielding the greatest population. In addition, the magnitude of the population of the a^3D_3 state varied markedly between the samples, thus providing a means of discrimination between Ni-Ni bonding and Ni_x-Si_y bonding. Thus, recognition of

specific Ni-silicide bonding enables identification of Ni-silicide based chemical compositional changes occurring in annealed Ni/SiC samples.

3.6.2 Velocity Distributions

When a target is bombarded with an ion beam, the material sputtered from the surface does not travel at a single speed. Indeed, there is an inherent distribution of velocities of the sputtered species. It has been shown that these velocity distributions are highly dependent on the electronic state of the sputtered atoms and that these state-dependent velocity distributions can themselves vary according to the bonding environment [5].

The method of obtaining a velocity distribution requires that a short, pulsed ion beam (of the order of 300ns) is used to probe the sputtered material. In this way, the photo-ionisation process becomes very velocity selective. By fixing the distance at which the laser pulses intercept the sputtered plume from the target surface and varying the time at which the lasers fire, a plot of the photo-ion intensity as a function of the time delay will represent the velocity distribution of that particular electronic state. If the delay time range was varied from zero to ∞, with infinitely small increments, the integral of each velocity distribution should theoretically equal the corresponding state value in the population partition.

Figure 3.4 shows an example of state-selective velocity distributions for the ground state multiplet, a^3F_J, and first excited state multiplet, a^3D_J, obtained by Bastiaansen[5] on various nickel-silicide targets. The velocity distributions of all the atoms in the a^3D_J states tends to be broader and peak at higher velocities in comparison to those in the a^3F_J, although the disparity varies depending on the Ni-silicide. Ni_2Si showed the greatest distinction between the ground and excited state distributions, while the difference became less pronounced as the stoichiometry changed to favour Si. The comparable measurements for pure Ni [9] exhibited broader velocity distributions with the peaks correspondingly occurring at higher velocities. Consequently, careful selection of laser pulse timing permits photo-ionisation of a specific section of the velocity distributions. By selecting this intercept time such that maximum variation is observed when a different sample composition is present whilst yielding sufficient atoms to be photo-ionised for detection, identification of the actual composition can be ascertained. This becomes a powerful tool in a mixed phase sample as it allows discrimination between pure Ni and Ni-silicide, and also between individual Ni-silicides themselves.

Such discrimination is particularly useful in these studies, where mixed phase structures consisting of Ni-silicides have been suggested.[10,11,12]

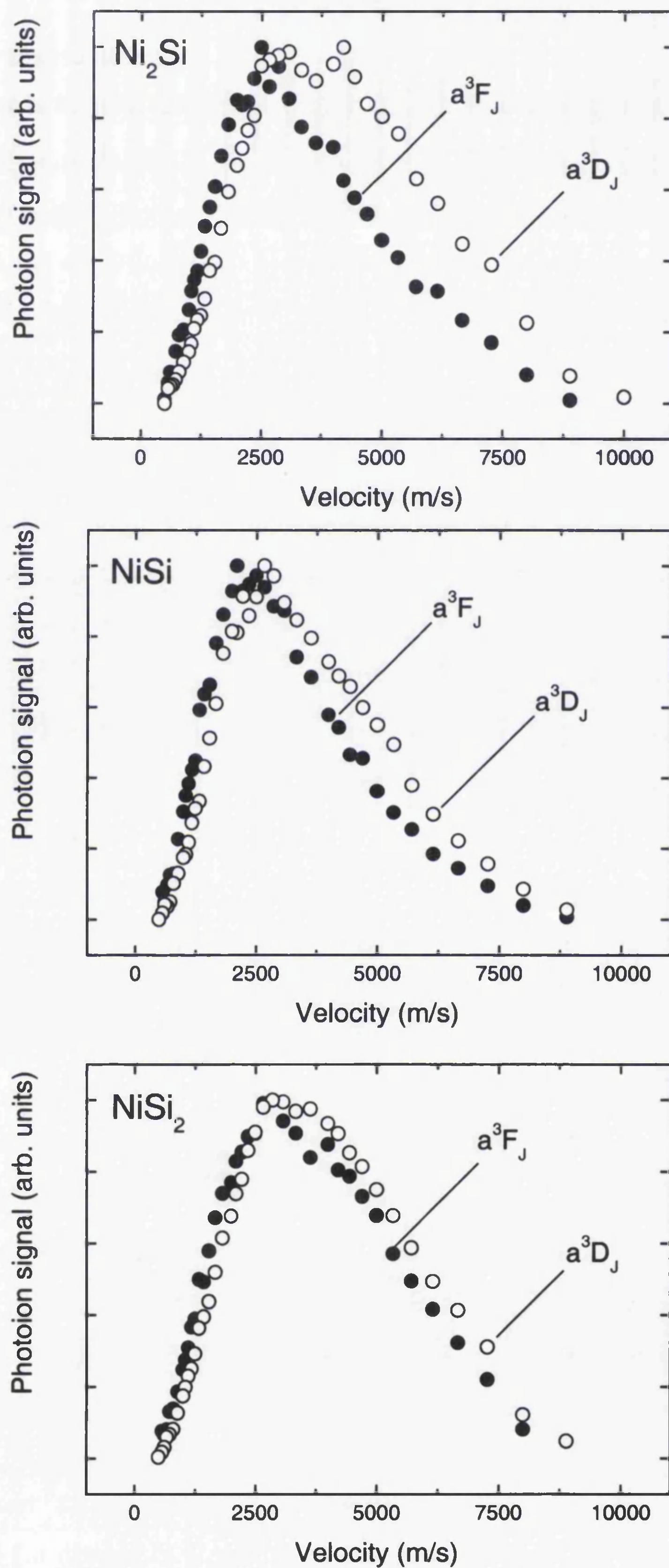

Figure 3.4: State-selective velocity distributions of Ni atoms sputtered from Ni_2Si, NiSi, and $NiSi_2$ targets (Bastiaansen, 2003)[5].

3.7 RIMS Depth Profiling

Depth profiling using TOF-SIMS is a well-established technique used in many areas of research. However, its greatest drawback is the well documented "matrix effect", whereby the secondary ion yield is sensitive to the target matrix under analysis. By employing the RIMS technique for use in depth profiling, the matrix effect is negated to a large extent, permitting a more sensitive analysis to be performed. Indeed, several groups have undertaken RIMS/SNMS depth profiling using Ar^+ primary ions with an encouraging level of success [13,14,15], while Willey et al [16] have used a liquid metal ion gun (LMIG) to provide enhanced spatial resolution.

A shortfall of the technique is that a limited number of elements can be analysed simultaneously. Naturally, if more laser systems are available, the technique is not restricted to single element analysis per profile.

3.8 Summary

This chapter has given a brief introduction to the theory of RIMS, the factors affecting efficient ionisation, and a description of how the technique of measuring the population partitions of atoms in specific electronic states and the associated velocity distributions are sensitive to chemical binding thus enabling identification of specific Ni-silicide alloys. It is important to note that the range of sputtered atom velocities probed and hence the number of photo-ions detected is directly proportional to the length of the sputtering ion pulse. Consequently, where a particularly small section of the velocity distribution is to be probed, detector efficiency is of the utmost importance, particularly when depth profiling through a matrix of low sputter yield. Where the photo-ion signal is particularly poor, use of a sufficiently long primary ion pulse permits photo-ionisation of the entire distribution thus enabling identification of the alloy present via the difference in the population partitions. In either case, the flexibility of this technique is particularly useful in practice.

The application of the RIMS theory is shown in the RIMS depth profiles of Ni/SiC samples in Chapter 7.

[1] N. Winograd, J.P. Baxter, F.M. Kimock, Chem. Phys. Lett. **88,** 581 (1981).

[2] G.S. Hurst, M.G. Payne, *Principle and Applications of Resonance Ionisation Spectroscopy*, (IOP Publishing Ltd., Adam Hilger, Bristol) (1988).

[3] E. Vandeweert, Sputtering of atoms in metastable states studied by resonant laser-ionization spectroscopy, PhD thesis, Katholieke Universiteit Leuven (1997).

[4] E. Vandeweert, V. Philipsen, W. Bouwen, P. Thoen, H. Weidele, R.E. Silverans, P. Lievens, Phys. Rev. Lett. **78,** 138 (1997).

[5] J. Bastiaansen, Electronic Processes during Sputtering of Metals studied by Resonant Laser Ionization, PhD thesis, Katholieke Universiteit Leuven (2003).

[6] E. Vandeweert, J. Bastiaansen, V. Philipsen, P. Lievens, R.E. Silverans, Nucl. Instrum. Meth. **B164-165**, 795 (2000).

[7] J. Bastiaansen, F. Vervaecke, E. Vandeweert, P. Lievens, R.E. Silverans, Spectrochimica Acta **B58**, 1147 (2003).

[8] P. Lievens, V. Philipsen, E. Vandeweert, R.E. Silverans, Nucl. Instrum. Meth. **B135,** 471 (1998).

[9] J. Bastiaansen, F. Vervaecke, E .Vandeweert, P. Lievens, R.E. Silverans, Spectrochimica Acta **B58,** 1147 (2003).

[10] Ts. Marinova, A. Kakanakova-Georgieva, V. Krastev, R. Kakanakov, M. Neshev, L. Kassamakova, O. Noblanc, C. Arnodo, S. Cassette, C. Brylinski, B. Pécz, G. Radnoczi, Gy. Vincze, Materials Science and Engineering **B46,** 223 (1997).

[11] B. Pécz, G. Radnoczi, S. Cassette, C. Brylinski, C. Arnodo, O. Noblanc, Diamond and Related Materials **6,** 1428 (1997).

[12] B. Pécz, Appl. Surf. Sci. **184,** 287 (2001).

[13] L. Johann, P. Kern, R. Stuck, Nucl. Instrum. Meth. **B100,** 519 (1995).

[14] Y. Higashi, T. Maruo, Y. Homma, Surface and Interface Analysis **26** (3), 220 (1998).

[15] Y. Higashi, Spectrochimica Acta **B54,** 109 (1999).

[16] K.F. Willey, H.F. Arlinghaus, T.J. Whitaker, Appl. Surf. Sci. **144-145,** 36 (1999).

Chapter 4: Semiconductor contacts and their preparation

4.1 Introduction

Semiconductors are materials with electrical characteristics that fall between insulators and conductors and which form the basis of most electronic devices. It is possible to form a device when metal contacts are deposited onto a semiconductor and these contacts can then allow an electric current to pass through the device. Depending on the metal and semiconductor used, and indeed the temperature to which the device is exposed, the contact produced can exhibit either rectifying characteristics or Ohmic characteristics. The rectifying nature allows current to flow in one direction but not in the other (via a high resistance). An Ohmic contact is characterised by a low resistance in both directions (forward and reverse bias), allowing current to flow easily.

These studies investigate the chemical changes that occur when nickel is deposited on silicon carbide at room temperature then subsequently annealed to high temperature, ~1000°C. At room temperature, the metal-semiconductor contact displays rectifying, or Schottky, characteristics whereas the annealed samples reveal an Ohmic nature[1].

This chapter will give a general overview of semiconductor theory, specifically describing metal-semiconductor contact formation, before outlining the sample preparation techniques. A full description of semiconductor theory can be found in books by Rhoderick & Williams[2] and Wilmsen.[3]

4.2 Schottky contacts

It is common that when a metal film is deposited on a semiconductor, a barrier to current flow (known as a Schottky barrier) is formed at the interface. This barrier impedes current flow across the metal-semiconductor interface. The principles of such rectifying contacts are established in the Schottky-Mott theory [4,5] and are best described by considering the band structure of metals and semiconductors. When the metal and a semiconductor are separate from one another as in Figure 4.1 (a), the conduction and valence electron bands of the semiconductor are flat up to the surface of the semiconductor (assuming ideal conditions and neglecting surface states), while the vacuum levels of both the metal and semiconductor are aligned with one another.

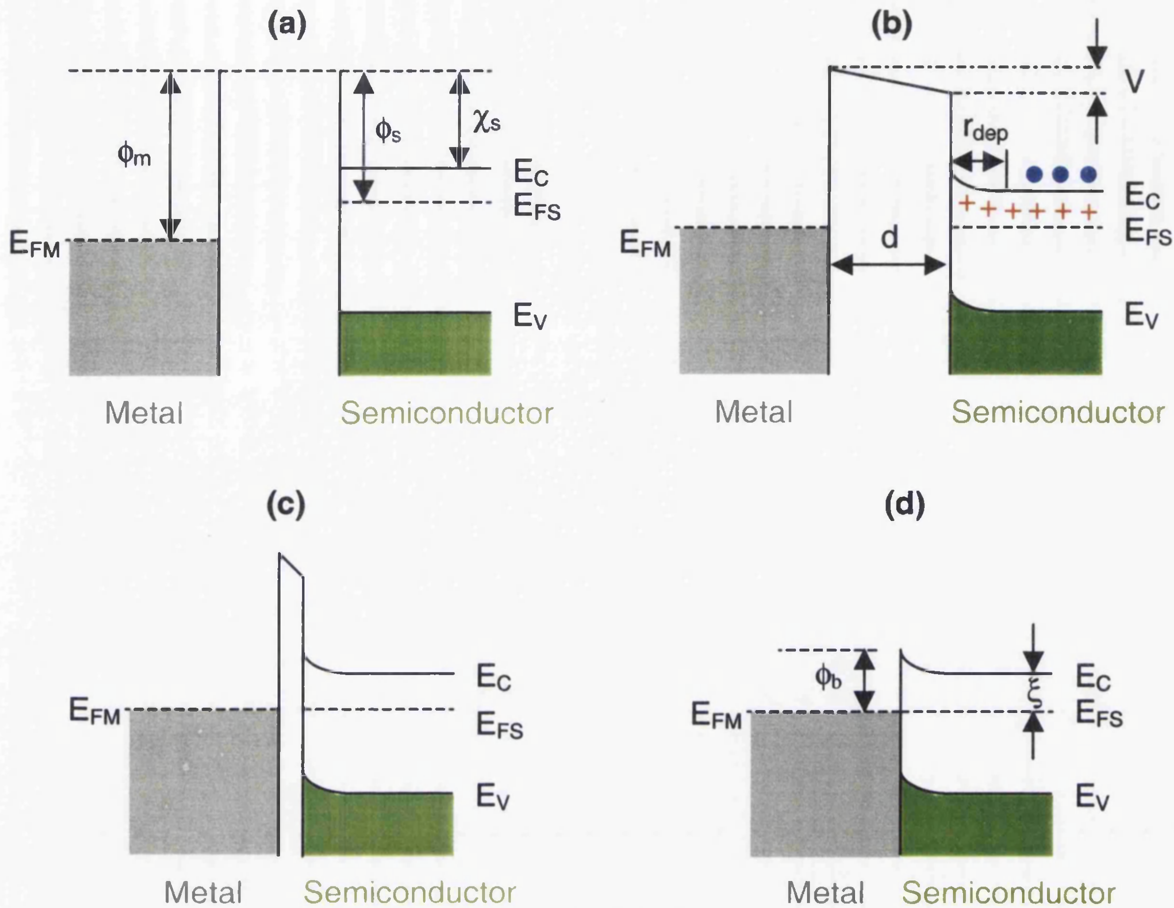

Figure 4.1: Schottky contact barrier formation between a metal and semiconductor where the metal and semiconductor are: (a) separate and neutral, (b) electrically connected, (c) separated by a narrow gap, (d) in intimate contact. ϕ_m and ϕ_s are the work functions of the metal and semiconductor respectively, χ_s represents the electron affinity of the semiconductor, ϕ_b represents the Schottky barrier height, ξ is the field in the gap, r_{dep} represents the depletion region and d is the distance between the metal and semiconductor. ● represents the conduction band electrons, while the donor ions are represented by +.

The work functions, ϕ_m and ϕ_s, are defined as the amount of energy required to raise an electron from the Fermi level of the metal or semiconductor respectively, to a state of rest outside the surface of the metal or semiconductor, known as the vacuum level. In the case of Figure 4.1, the semiconductor is taken to be n-type and hence the work function of the metal is greater than that of the semiconductor. The electron affinity, χ_s, may be defined as the energy difference between an electron in the vacuum level and an electron at the bottom of the semiconductor conduction band, just within the surface. Figure 4.1 (b) represents a situation where the metal and semiconductor are connected electrically, although the two are not in direct physical contact. In such a situation,

electrons are transferred from the semiconductor into the metal causing the Fermi levels of the metal and semiconductor to shift into alignment with one another. The transfer of conduction electrons from the semiconductor results in a negative charge on the metal surface with a corresponding positive charge due to donor ions in an electron depleted region (denoted r_{dep}) near the surface of the semiconductor causing an electric field to be set up in the metal-semiconductor gap. This results in upward bending of the semiconductor bands.

The potential difference, V, caused by the difference in energies of electrons outside the surface of the metal and semiconductor is determined by the width of and electric field within the metal-semiconductor gap, i.e.

$$V = d.\xi \qquad \textbf{Equation 4.1}$$

where d is the metal-semiconductor separation and ξ is the field in the gap. Therefore, V must decrease as the metal and semiconductor are brought closer together, as in Figure 4.1 (c), in order to maintain a finite value of ξ. When the metal and semiconductor are in direct contact, as shown in Figure 4.1 (d), the vacuum-induced barrier is removed, leaving a Schottky barrier with a height, ϕ_b, equal to the work function of the metal in question, ϕ_m, minus the electron affinity of the semiconductor, χ_s, i.e.

$$\phi_b = \phi_m - \chi_s \qquad \textbf{Equation 4.2}$$

It should be noted that this equation assumes an ideal contact is formed. In reality, an oxide layer will be formed on the semiconductor in most practical contact, although the potential drop in this oxide layer is small enough to permit Equation 4.2 to yield a good approximation for the barrier height [2].

Equation 4.2 implies that the choice of metal is crucial in determining the electrical properties of the device. In reality, however, it is often found that the barrier height is independent, or only weakly dependent on the work function of the metal. Consequently, Bardeen[6] developed a theory based on surface states rather than work function differences. The motivation for this theory was that the periodicity of a

semiconductor crystal lattice is interrupted at the material surface, at which localised electronic states could exist within the energy gap of a semiconductor, as shown in Figure 4.2. A distribution of surface states of density D_S cm^{-1}.eV^{-1} are assumed and the charge neutrality level ϕ_o is taken into account. The charge neutrality level is defined as the energy level, taken relative to the valence band, to which surface states must be filled when the surface is neutral. In the case of the Schottky-Mott model, where surface states are not considered, the required condition for an electrically neutral junction between the metal and semiconductor is that the negative charge on the metal surface, Q_M, is countered by a positive charge of equal magnitude as a result of the uncompensated donor ions in the depletion region, Q_D. Preservation of an electrically neutral junction where surface states are present dictates that:

$$Q_M + Q_D + Q_S = 0$$ **Equation 4.3**

where Q_S is the charge due to the surface states. The surface state occupation is determined by the Fermi level, up to which states are filled and above which the states are empty when the absolute-zero approximation is used. This approximation is generally sufficient in most cases.

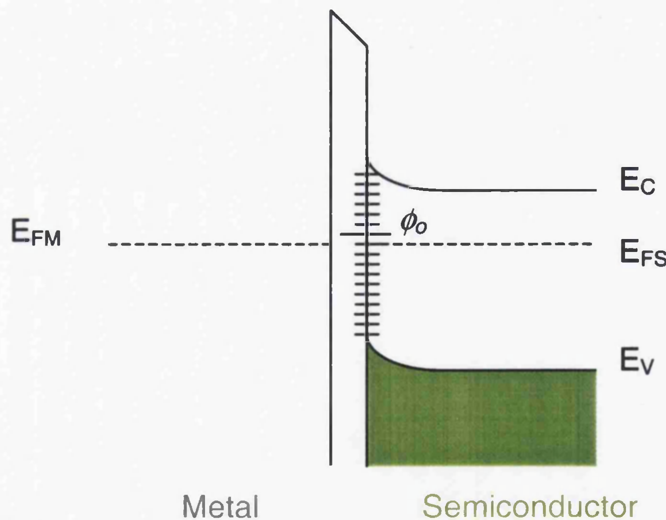

Figure 4.2: Diagram of surface states within a metal-semiconductor contact.

If ϕ_o is above the Fermi level, as in Figure 4.2, the surface states will exhibit an overall positive charge, which, to maintain neutrality, demands that the charge due to the donor ions, Q_D, must decrease, resulting in a corresponding decrease in the width of the

depletion region and the degree of band bending. This results in a decrease in the barrier height ϕ_b, which has the effect of forcing ϕ_o towards the Fermi level by reducing the positive charge in the surface states. Conversely, if ϕ_o is below the Fermi level and the surface states exhibit an overall negative charge, Q_D must increase also, resulting in an increase in the width of the depletion region and the barrier height, again causing ϕ_o to be forced towards the Fermi level. Where the density of states is particularly large, ϕ_o is approximately equal to the Fermi level and the barrier height is given by:

$$\phi_b = E_g - \phi_o \qquad \textbf{Equation 4.4}$$

where E_g is the semiconductor band gap. This equation is known as the Bardeen limit and, in such cases, the barrier height is "pinned".

Since a thin interfacial layer is usually formed between a metal and semiconductor, the barrier height ϕ_b typically lies between the Schottky and Bardeen limits. From the initial analysis of this general case[7], the Schottky barrier height with no electric field present within the semiconductor was derived:

$$\phi_b = \gamma(\phi_m - \chi_s) + (1-\gamma).(E_g - \phi_o) \qquad \textbf{Equation 4.5}$$

where γ is given by:

$$\gamma = \frac{\varepsilon_l.\varepsilon_o}{\varepsilon_l.\varepsilon_o + e.\delta.D_s} \qquad \textbf{Equation 4.6}$$

where ε_l is the relative permittivity of the interface layer, ε_o is the permittivity of free space, e is the electronic charge and δ is the width of the interface layer. When the density of states, D_s, equals zero, as in the Schottky model, $\gamma = 1$ and ϕ_b is given by ϕ_m - χ_s, i.e. the Schottky limit (Equation 4.2). Conversely, when the density of states is large, γ tends to zero and ϕ_b is given by E_g - ϕ_o, the Bardeen limit (Equation 4.4).

Whilst it is possible to deposit a metal layer epitaxially on a semiconductor, whether or not the lattice constants are matched (although matched lattice constants reduces strain within the layer), it is usual for the deposited metal layer to be polycrystalline in nature.

Since most metal-semiconductor interfaces are not atomically abrupt, diffusion of metal atoms into the semiconductor and vice versa may occur. Where the metal deposition on the semiconductor results in substantial chemical reactions, an interfacial compound layer is formed, which can substantially alter the electrical characteristics. In some cases, a relatively inert reaction can be replaced by a strong reaction when the temperature of the metal-semiconductor is increased sufficiently.

Another interaction that occurs between the metal and semiconductor is the formation of metal-induced gap states (MIGS), first described by Heine[8], which replace intrinsic electron states present on the semiconductor surface. The effect is quantum mechanical in nature and stems from the wavefunctions of the metal electrons decaying exponentially into the semiconductor where the metal conduction band and semiconductor band gap overlap. The tails of these electron wavefunctions form a continuum of states within the band gap. Near the valence band, the character of the MIGS is donor-like, it is acceptor-like near the conduction band, and zero at the Fermi level. The occupation of the MIGS determines the position of the Fermi level and thus dictates the barrier height.

4.3 Ohmic contacts

As already described, when ϕ_b is large, a Schottky barrier exists. However, when ϕ_b is small or negative, an Ohmic contact exists. Both these contact types are shown in Figure 4.3 (a) and (b). In an ideal Ohmic contact, no potential exists between the metal and semiconductor and charge carrier flow is not obstructed in either direction across the junction hence the current flow under an applied voltage is directly proportional to the voltage.

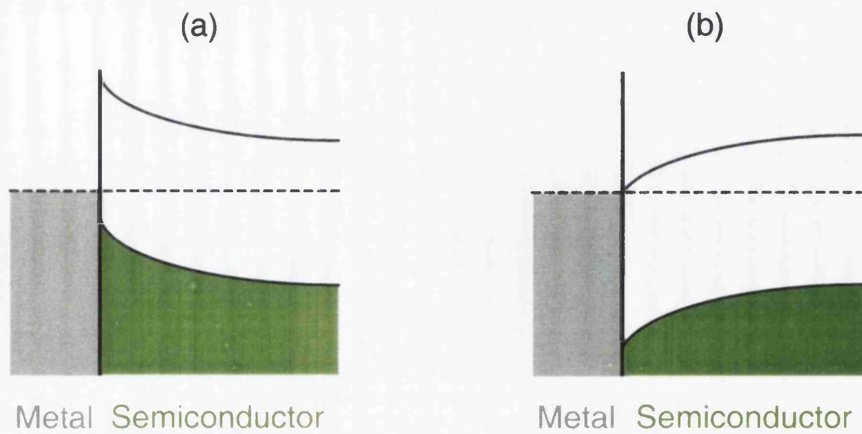

Figure 4.3: Examples of barriers for an n-type semiconductor. (a) is a Schottky barrier, where $\phi_m > \phi_s$, while (b) is an Ohmic contact, where $\phi_m < \phi_s$.

The Ohmic and Schottky nature of contacts is best described in a current/voltage (I/V) plot. Figure 4.4 represents an example of the different I/V characteristics of both contacts.

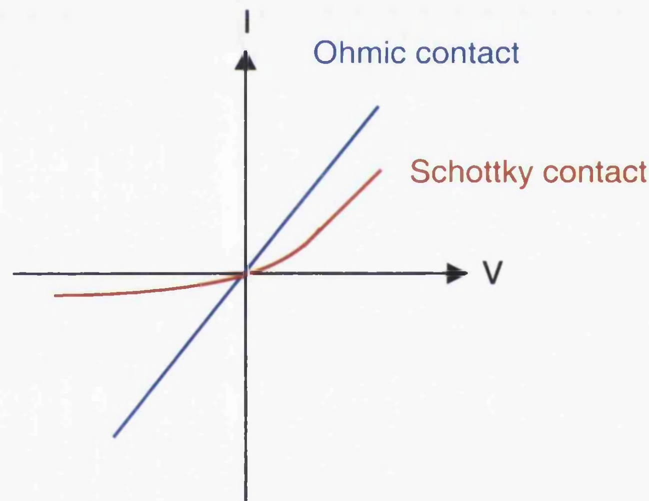

Figure 4.4: I/V characteristics of Schottky and Ohmic contacts.

The barrier height ϕ_b is now known to be weakly dependent on the work function of the metal contact used thus most practical contacts rely on a high level of semiconductor doping at the interface. Many different metals have been studied for use as contact layers to SiC, including fairly exotic metals such as palladium[9] and ruthenium[10] as well as more common metals such as titanium, aluminium and nickel.

4.4 Sample Preparation

All samples used in these studies used n-type 4H-SiC wafers doped with nitrogen at a density of $10^{-19}cm^{-3}$ with a 10μm epilayer. In order to remove inherent surface roughness and surface contamination from external sources, the samples underwent a series of cleaning and etching routines to produce an atomically clean surface. The ex-situ clean consisted of a solvent clean and an RCA clean. The solvent clean is a soft chemical clean using Trichloroethylene, Acetone and Isopropanol to remove oil based contaminants and dust. The RCA clean is a strong chemical clean used to remove organic substances, oxide strip and ionic clean, details of which are described by Kern and Puotinen[11]. The RCA chemicals attack the SiO_2 on the surface but do not modify the SiC. The technique prevents re-plating of metal contaminants and leaves the surface free of residue and contamination.

When performing UHV deposition, the sample was also heat treated in UHV by e-beam bombardment to remove oxygen from the surface of the SiC prior to deposition. This anneal followed standard procedures[12] of SiC preparation for STM measurements. Following deposition of Ni, contacts with an Ohmic nature were produced by e-beam heating of the sample at 1000°C for 10 minutes. Methods were altered for Edwards preparations, where no heat cleaning of the SiC was undertaken prior to Ni deposition. Details of the UHV and Edwards evaporation techniques are described below.

UHV Metal Evaporation

In order to produce a metal contact for deposition on the semiconductor surface, an Oxford Research EGN4 mini e-beam UHV evaporator was used. The evaporator consists of four hearths, enabling deposition of up to four materials in one routine, into which a rod of the desired material is inserted. To prevent evaporation of material in adjacent hearths, a water-cooling system is employed. In these studies, a 99.99% purified nickel rod was used. In order to evaporate the Ni, a 2kV potential is applied to the rod, while a filament emits electrons, forming a focused electron beam, which is forced to the end of the rod causing it to melt and evaporate when the filament current is sufficient. The evaporated metal is then deposited on the sample, while an ion current collector detects the flux of ionised Ni atoms. The ion current is directly proportional to the amount of evaporated Ni, permitting a deposition rate to be established. The deposition rate and thickness can also be calibrated using a quartz crystal monitor, and verification of Ni thickness using an AFM is also employed.

A drawback of the UHV deposition technique was that it is designed for thin film coverage. Therefore, the deposition of a 200nm contact layer for TOF-SIMS and RIMS studies took approximately 5 hours to complete. During this time, systemic fluctuations can cause an element of variability in the deposition rate. As a result, the actual thickness of the Ni layer deposited on the SiC substrate would occasionally be quite different from the desired thickness.

High Vacuum Edwards Evaporation Chamber

While the UHV deposition source is generally used to deposit thin metal contact layers, deposition of the thicker contact layers, such as those required for practical devices, becomes impractical in the UHV system. In such cases, an Edwards E306A Thermal Evaporator is more applicable. Indeed, later samples were produced using the Edwards system.

The Edwards evaporator functions at high vacuum, typically in the 10^{-6} mbar range (pumped via a rotary pump and diffusion pump) and uses a coil filament to heat a graphite crucible containing small pieces of pure metal to be evaporated for deposition. The sample is held above the crucible with the surface used to accept the metal facing the crucible. A shield is inserted between the crucible and the sample while the metal is heated. During the heating process, the evaporation rate increases until it reaches a constant level. Once the rate is constant, the shield is removed and the metal deposition on the semiconductor proceeds. A crystal monitor is used to determine the thickness of the metal deposition. Again the deposition rate is dependent on the filament current and once the evaporation rate was constant, deposition of "thick" contacts of ~ 200nm was achieved in minutes rather than hours, as in the UHV evaporator.

The Edwards evaporator also possesses the facility to anneal samples in-situ by connecting the sample holder to a high voltage external power source with current regulation. An anneal temperature of 1000°C, which is more than sufficient to induce the Schottky-Ohmic transition in Ni/SiC sample, is typically attained with a current of ~ 40mA.

4.5 Samples used in SIMS/RIMS studies and bombardment conditions

Top Contact	Deposition Type	Barrier Type	Erosion Conditions	Acquisition Conditions
200nm Ni	UHV As-deposited	Schottky	4keV Ar^+ (2kV bias) 500μm spot	15keV Ga^+ (4kV bias) 25μm x 25μm
100nm Ni	UHV 1000°C	Ohmic	4keV Ar^+ (2kV bias) 500μm spot	15keV Ga^+ (4kV bias) 25μm x 25μm
50nm Ni	UHV As-deposited	Schottky	15keV Ga^+ (4kV bias) 100μm x 100μm	15keV Ga^+ (4kV bias) 25μm x 25μm
100nm Ni	UHV 1000°C	Ohmic	15keV Ga^+ (4kV bias) 100μm x 100μm	15keV Ga^+ (4kV bias) 25μm x 25μm
200nm Ni	Edwards HV As-deposited	Schottky	15keV Ga^+ (4kV bias) 500μm spot	15keV Ga^+ (4kV bias) 200μm spot
200nm Ni	Edwards HV 1000°C	Ohmic	15keV Ga^+ (4kV bias) 500μm spot	15keV Ga^+ (4kV bias) 200μm spot
200nm Ni	Edwards HV As-deposited	Schottky	7keV Ga^+ (4kV bias) 500μm spot	7keV Ga^+ (4kV bias) 200μm spot
200nm Ni	Edwards HV 1000°C	Ohmic	7keV Ga^+ (4kV bias) 500μm spot	7keV Ga^+ (4kV bias) 200μm spot

Table 4.1: Samples used for SIMS studies and bombardment conditions. All samples used a SiC substrate with a 50nm Ni Ohmic back contact.

Top Contact(s)	Substrate	Bottom Contact	Deposition Type	Barrier Type	Bombardment Conditions
200nm Ni	SiC	50nm Ni	UHV As-deposited	Schottky	15keV Ar^+ 2mm spot
100nm Ni	SiC	50nm Ni	UHV 1000°C	Ohmic	15keV Ar^+ 2mm spot
5nm Ag 5nm Ni 5nm Ag 5nm Ni	MgO	n/a	Molecular Beam Epitaxy	n/a	15keV Ar^+ 1mm spot (Variable focus)
200nm Ni	SiC	50nm Ni	Edwards HV	Schottky	15keV Ar^+ 1mm spot (defocused)
200nm Ni	SiC	50nm Ni	Edwards HV	Ohmic	15keV Ar^+ 1mm spot (defocused)

Table 4.2: Samples used for RIMS studies and bombardment conditions.

4.6 Summary

Using the basic theory of semiconductor contacts and standard preparation techniques, Ni/SiC contacts of varying electrical nature were produced for TOF-SIMS and RIMS analysis. Results are described in chapter 6 and chapter 7 respectively.

4.7 References

[1] A. Kestle, S.P. Wilks, P.R. Dunstan, M. Pritchard, P. Mawby, Electronics Letters Vol. **36** (3), 267 (2000).

[2] E.H. Rhoderick, R.H. Williams, Metal-Semiconductor Contacts 2nd Ed. (1988).

[3] C.W. Wilmsen, Physics and chemistry of III-V compound semiconductor interfaces, Plenum Press (1985).

[4] W. Schottky, Naturwissenschaften **26,** 843 (1938).

[5] N.F. Mott, Proc. Camb. Phil. Soc. **34,** 568 (1938).

[6] J. Bardeen, Phys. Rev. **71,** 717 (1947).

[7] A.M. Cowley, S.M. Sze, J. Appl. Phys. **36,** 3212 (1965).

[8] V. Heine, Phys. Rev. **A138**, 1689 (1965).

[9] S. Roy, S. Basu, C. Jacob, A.K. Tyagi, Appl. Surf. Sci. **202,** 73 (2002).

[10] S. Roy, C. Jacob, M. Zhang, S. Wang, A.K. Tyagi, S. Basu, Appl. Surf. Sci. **211,** 300 (2003).

[11] W. Kern, D.A. Puotinen, RCA Rev. **31,** 187 (1970).

[12] W.Y. Lee, The control of metal-silicon carbide contact using a silicon interlayer, PhD Thesis, University of Wales Swansea (2004).

Chapter 5: Experimental Systems and Procedures

5.1 Experimental Setup at Swansea

The system in Swansea is a VG time-of-flight secondary ion mass spectrometer in which the sample under investigation is held in an ultra-high vacuum (UHV) chamber. The basic configuration of the TOF-SIMS system consists of two primary ion sources with alignment optics, a sample chamber, a secondary ion extraction assembly, a mass discriminating detector and analyser, and an acquisition control and analysis system. Details of this system can be found elsewhere[1,2], but this chapter focuses on those areas essential to improving the depth-profile analysis.

The primary ion sources form ions that are accelerated and focused to the sample chamber and bombard the sample under investigation. This causes secondary ions, in addition to a large proportion of neutral species and clusters, to be ejected from the surface of the sample in a sputtered plume. The secondary ions are extracted from the specimen chamber and are accelerated to the mass analyser via a reflectron-type analyser where they are detected and mass differentiated. A mass spectrum of the sample may then be produced and the chemical composition of the sample determined. Diagrams of the TOF-SIMS system are shown in Figure 5.1 and Figure 5.2.

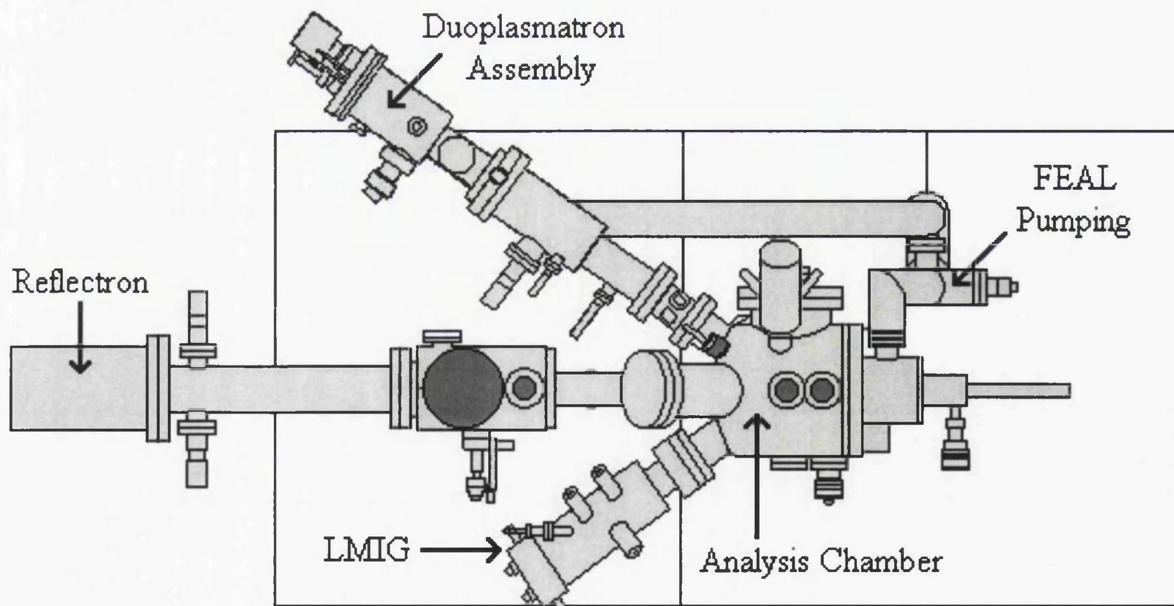

Figure 5.1: Plan view of TOF-SIMS apparatus at Swansea (following installation of LMIG).

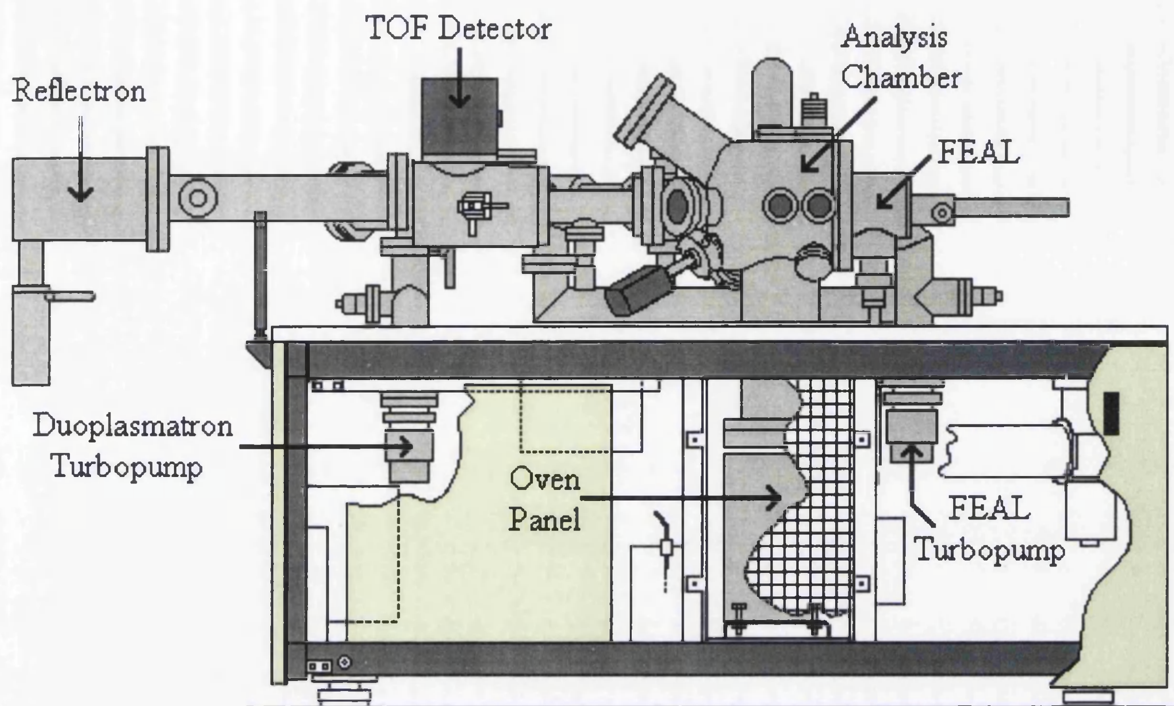

Figure 5.2: Side view of TOF-SIMS apparatus at Swansea (prior to installation of LMIG).

5.1.1 Vacuum System

One of the most fundamental aspects involved in SIMS regards the internal pressure of the equipment used to obtain SIMS data. SIMS experiments are always carried out in ultra-high vacuum (UHV) conditions i.e. less than 10^{-9} hPa, to prevent molecules within the air changing the surface properties of the sample under consideration. In the case of SIMS, excessive pressure within the ion source and sample chamber can also affect the path of the primary ion beam thus adversely affecting the efficiency of the system.

In order to achieve UHV conditions, the TOF-SIMS system was constructed from stainless steel and employed a multitude of pumping systems. The sample to be used for analysis was housed in the main chamber, to which the primary ion column (and later the liquid metal ion source also) and fast-entry air lock (FEAL) are attached. The first phase of pumping is undertaken by two Edwards RV5 rotary, or roughing, pumps each operating in conjunction with Pfeiffer-Balzers TPU60 turbo-molecular pumps to reduce the system pressure from atmospheric pressure to approximately 10^{-6} hPa. The first rotary/turbo pair is attached to the primary ion column to maintain constant pressure in the ion gun while the ion source is in operation. The second rotary/turbo

pair are attached to the FEAL, which itself can be isolated from the main chamber via a pneumatic isolation valve. The valve is capable of holding a 10^{-9} hPa pressure in the main chamber while the FEAL is at atmospheric. Consequently, this permits rapid sample changes to be carried out without unduly affecting the main chamber pressure. The second phase of pumping utilised a Perkin Elmer 170 l/s ion pump, attached directly beneath the main chamber, which was capable of operating in the 10^{-9} to 10^{-10} hPa range.

If the system spent an appreciable time at atmospheric pressure, e.g. when maintenance and/or refurbishment took place, UHV pressures were only re-achievable in a reasonable timescale if the system underwent a bake to accelerate desorption of gases from the chamber internal walls. The bake consisted of enclosing the system within reflective aluminium panels and operating the heating filament and circulating fan. The heating filament was thermostatically controlled to ensure the system temperature did not exceed 150°C, in order to prevent damage to Viton O-rings within the FEAL and ion gun. Following a bake, a base pressure of approximately 2.5×10^{-10} hPa was regularly achievable.

The duoplasmatron ion source had a typical operating pressure of approximately 5×10^{-4} hPa as a result of the gas supply. In order to prevent leakage into the main chamber that would raise the pressure and compromise UHV conditions, a differential pumping system was employed connecting the main section of the primary ion column to the FEAL rotary/turbo pair. Operable via a pneumatic valve controlled by the programmable logic control system when the ion source was lit, the differential pumping system was not entirely successful at isolating the main chamber from a pressure rise. Indeed, the main chamber pressure during analysis was typically about 1×10^{-8} hPa.

5.1.2 Valve System

The majority of the valves in the system were operable via a common-line pneumatic system running on nitrogen gas at 550kPa (80psi). The valving system, as employed in the TOF-SIMS apparatus, is shown in Figure 5.3 and consisted of a N_2 cylinder connected to the pneumatic valve manifold, which distributed the pressurised gas to individual valve actuators. Each actuator was controlled by a solenoid switch, which itself was controlled by the system programmable logic controller (PLC). Certain

valves, e.g. V20 between the DP ion gun and its turbopump, could be overridden manually via a push switch on the main electronic racks. This added a degree of flexibility to isolate sections of the system as required.

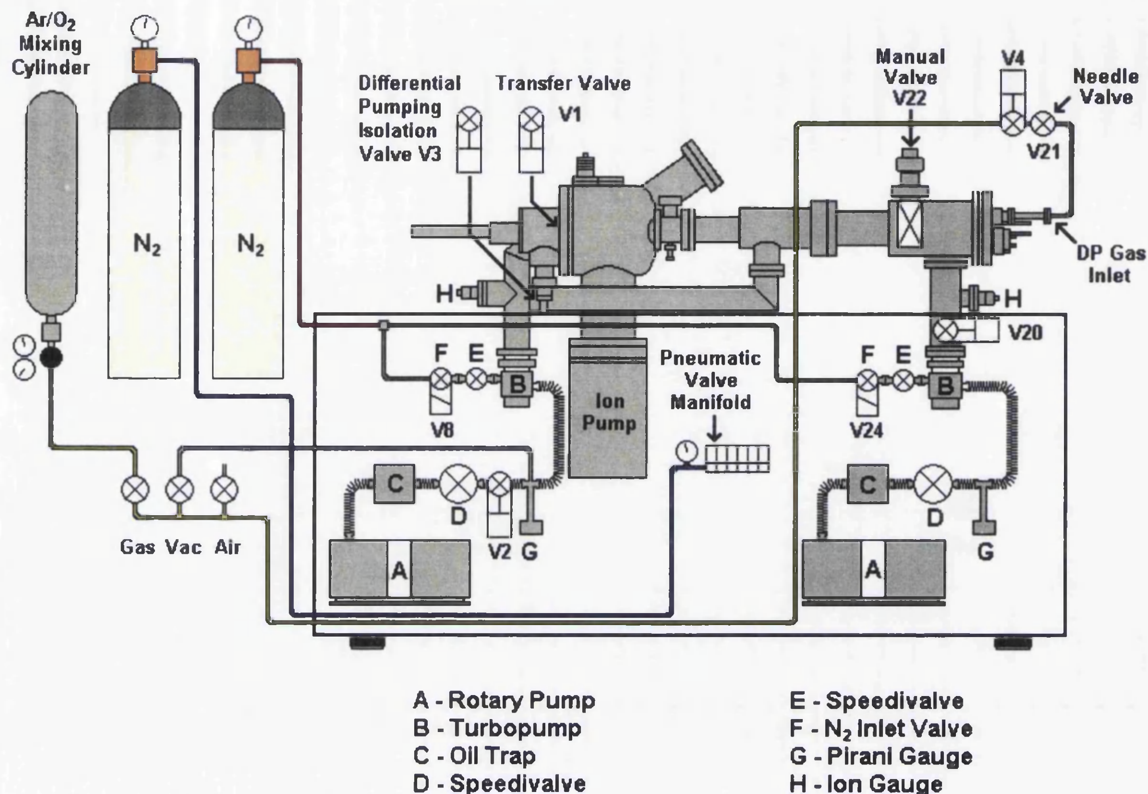

Figure 5.3: Pneumatic valving system for TOF-SIMS.

A minor addition to the existing valving system was the insertion of a speedivalve (SP10K) (labelled E on Figure 5.3) between the vent valve and the turbopump on both the main chamber pumping system and the ion gun pumping system. This modification served two purposes. Firstly, it was a precautionary measure instigated following failures that had occurred at inopportune times. Following failure of a vacuum component or the pneumatic circuit, the system would automatically default to atmospheric pressure through the opening of the vent valves once the turbopumps reached 35% of their maximum rated speed. Occasionally, a glitch in the PLC could also cause a shutdown of the system. In situations where the problem could be easily rectified, the loss of vacuum was a major setback. By ensuring the speedivalves were closed, a partial vacuum could be maintained for a longer duration when the system was shut down. If the shut down time was limited, a bake could often be foregone once pumping was restarted.

The second purpose of the speedivalve installation was to increase the flexibility of the system and permit both rotary/turbo pairs to be switched off for a short time (<1 hour), while holding the vacuum on the ion pump. Switching off the turbopumps also caused the associated cooling fans to power down. The net effect resulted in cancellation of the major source of noise and vibration in the system. Consequently, higher resolution imaging and spatial control of the ion beam was possible during this time. It was deemed unwise to hold the vacuum on the ion pump for longer periods while the ion gun was in operation.

5.1.3 Primary Ion Column

The original ion column assembly present in the TOF-SIMS system consists of a VG Ionex DP50B duoplasmatron ion source and high precision optical steering column to focus and steer the ion beam to the target.

A diagram of the duoplasmatron assembly as it appears when removed from the system is shown in Figure 5.4, while a magnified view of the components used in the formation of the plasma and extraction of the primary ions is shown in Figure 5.5.

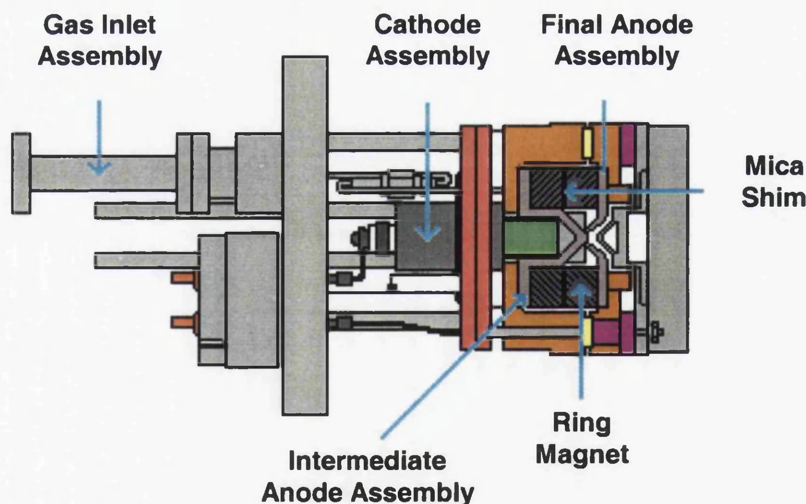

Figure 5.4: Diagram of duoplasmatron assembly.

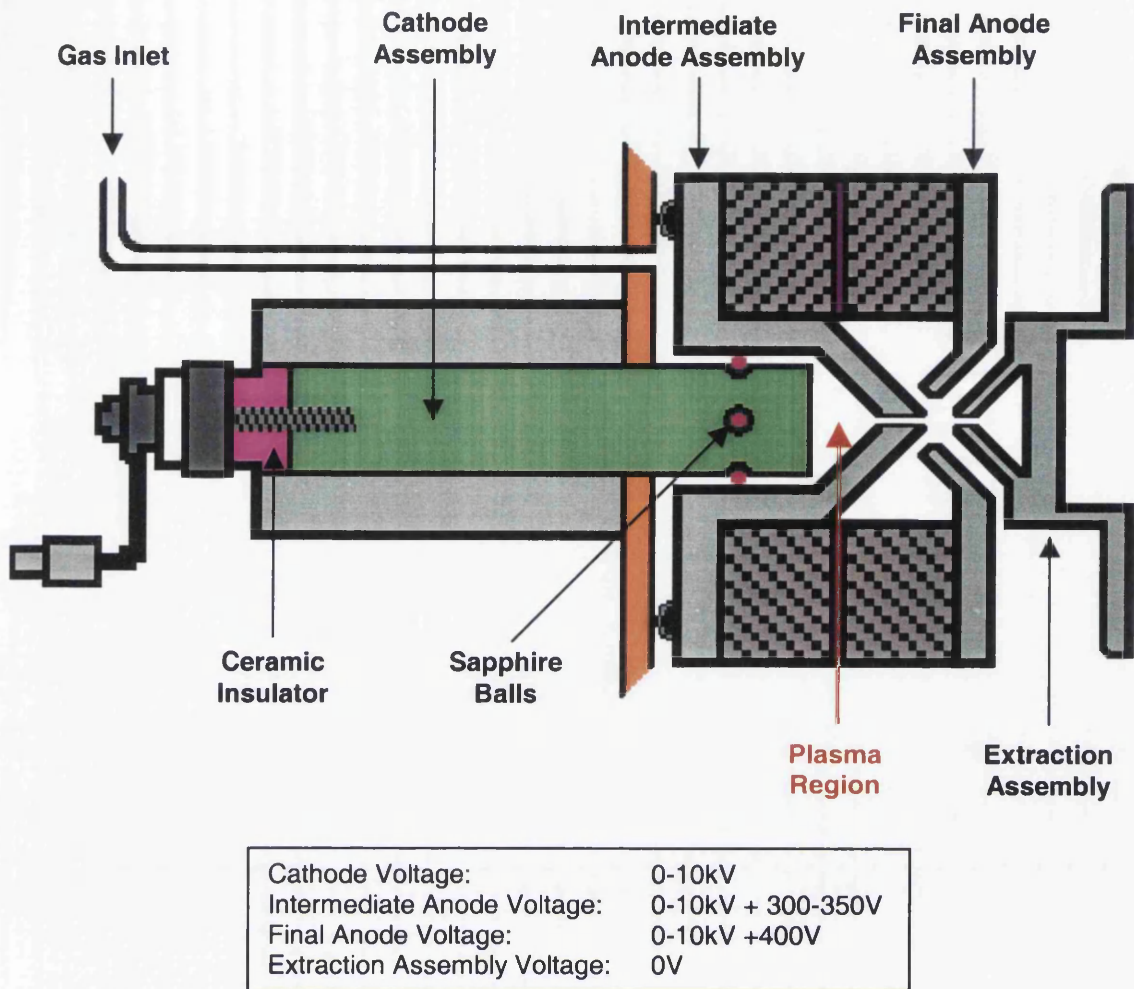

Cathode Voltage:	0-10kV
Intermediate Anode Voltage:	0-10kV + 300-350V
Final Anode Voltage:	0-10kV +400V
Extraction Assembly Voltage:	0V

Figure 5.5: Magnified section of plasma-forming and extraction assembly.

The duoplasmatron (DP) ion source works by feeding a gas supply of Ar/O_2, commonly in equal proportions into the plasma region identified in Figure 5.5. An arc is struck between the cathode, intermediate anode and anode to form a plasma that is magnetically constricted by two cylindrical magnets surrounding the intermediate anode/final anode assembly. The entire cathode and anode assemblies float at a user-defined high voltage (up to 10kV). The plasma expands through a small aperture in the anode plate, following which an ion beam is extracted due to the potential difference between the anode assembly and the extraction electrode, which is held at ground.

Due to the voltages involved, isolation of the individual components within the ion gun is essential. The cathode is isolated from its housing by six sapphire balls and a ceramic insulator at its base. The intermediate anode and final anode are also isolated by ceramic spacers and through mica shim insulators between the two ring magnets. Ceramic spacers are also used to isolate the final anode and extraction electrode. With

prolonged use, the electrical isolation characteristics of the ceramic pieces eventually deteriorates as they become covered with metallic particles "sputtered" by the plasma from components within the ion gun. Consequently, maintenance was routinely required to clean the ceramic insulators and ion gun components to regain efficient operation. A manual valve, V22, (refer to Figure 5.3) allowed the ion source to be isolated from the remainder of the system but was only capable of holding a pressure of 10^{-4} hPa in the main chamber when the ion gun section was at atmospheric pressure. As a result, the ion pump could not be operated and the main chamber vacuum had to be maintained with the rotary/turbo pair. Nevertheless, this feature often removed the necessity to bake the system after ion gun maintenance.

Once the ion beam was extracted from the ion gun, it proceeded down the primary ion column, a diagram of which is shown in Figure 5.6.

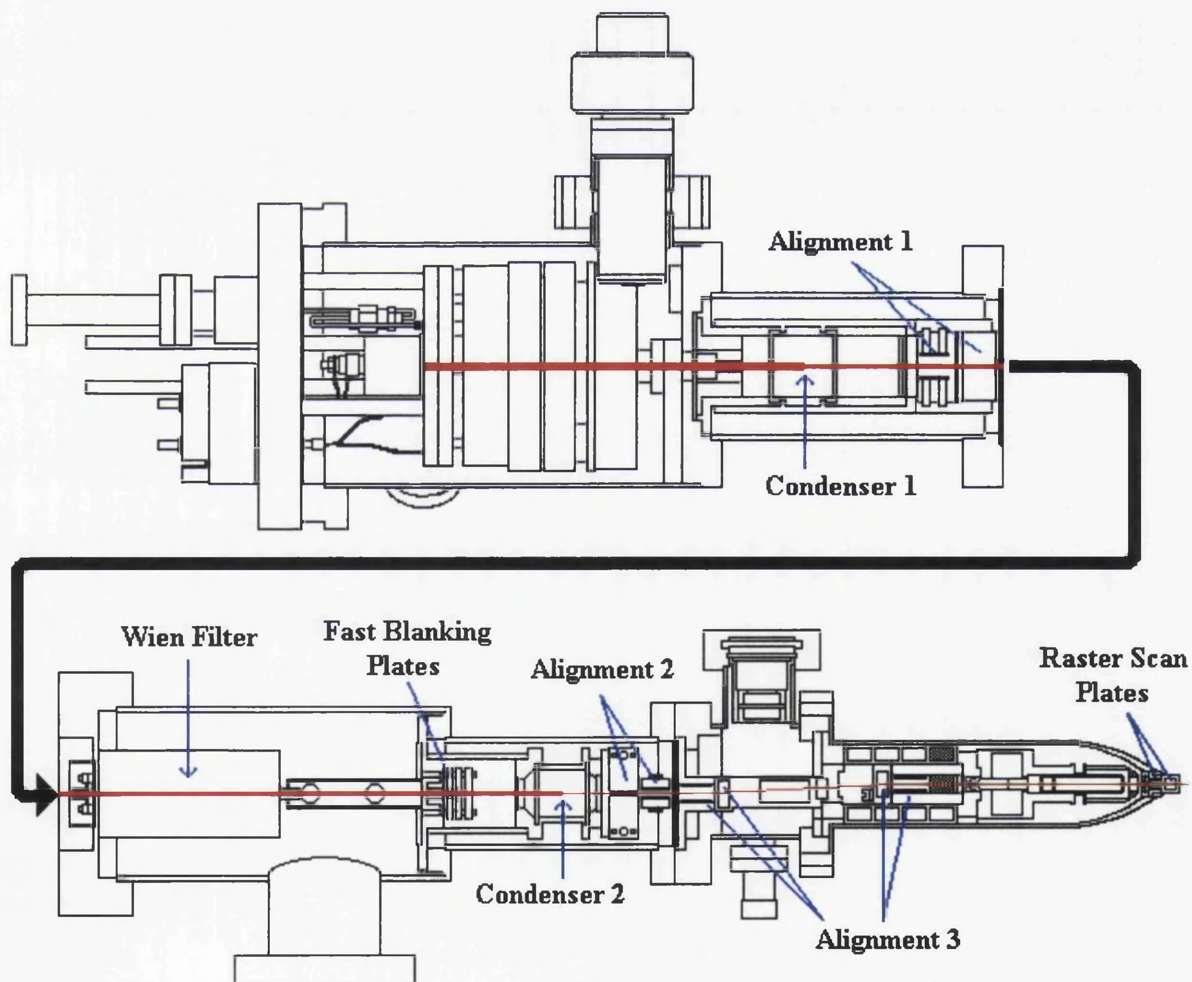

Figure 5.6: Diagram of duoplasmatron primary ion column.

To steer the ion beam from the source to the sample, a precision ion optical column was fitted, consisting of a series of alignment plates, lenses and a Wien Filter. The first component intercepted by the ion beam directly after emerging from the ion source is an Einzel condenser lens (denoted Condenser 1), which acts to uniformly compress the ion beam as a function of voltage applied to the lens. A set of X/Y beam alignment deflection plates then steer the focused ion beam towards the Wien Filter, a device used to select a particular mass primary ion to be used for analysis while terminating the paths of all other mass ions emitted from the ion source. The concept of a Wien Filter is shown in Figure 5.7.

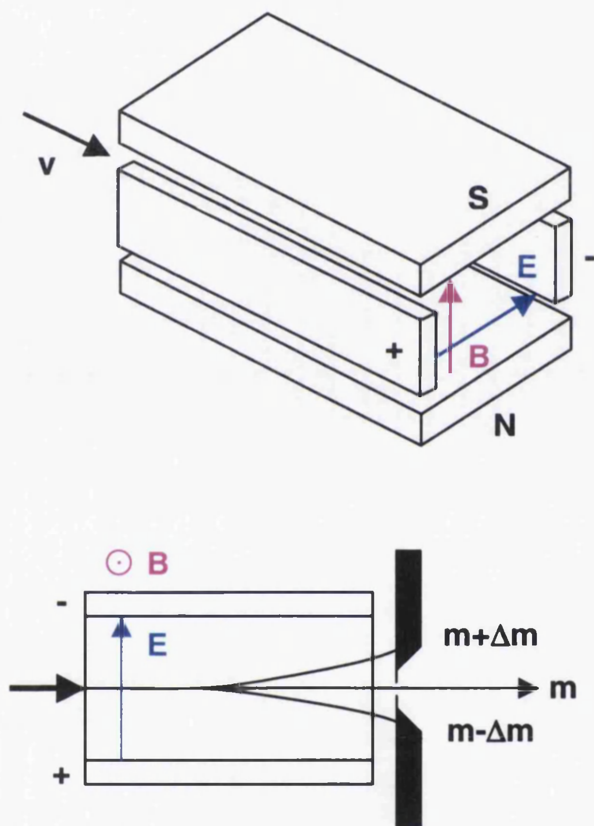

Figure 5.7: Diagram of a Wien filter showing how the mass selection process works.

The constant magnetic field between the N and S plates causes a mass dependent deflection of the ions. By applying an electric field to the perpendicular plates, the ion beam is counter deflected and variation of this field permits selection of the specific primary ion mass to be used for analysis.

In order to pulse the primary ion beam for mass spectrum acquisition, a series of fast blanking plates are located after the Wien Filter. These plates rapidly deflect the path of the conical ion beam, permitting it to pass through an aperture before deflecting the

beam back to its starting position resulting in an ion pulse that travels onward to the sample. Naturally, once the ion pulse has been produced, the voltage applied to the fast blanking plates must be returned to its initial value. To ensure that the beam does not sweep back through the aperture at any time while the voltage on the plates is returning to the starting values, an orthogonal set of plates deflect the beam at 90° to its initial path, thus the beam describes a "squared-circular" shape during a single cycle. In continuous mode, a continuous high voltage is applied to one of the plates, while the other is kept at 0V to allow the beam through.

The ion pulse or continuous beam passes through a second Einzel condenser lens to counter divergency from the first lens then proceed to the second and third set of X/Y alignment plates. The two sets enable any substantial variation in the beam to be significantly corrected. The third set consists of two individual sets of X alignment plates and two individual sets of Y alignment plates. The first set of Y alignment plates are used to deflect the beam sufficiently to compensate for a "dog-leg" in the ion column, which is used to eliminate any neutral species that may still be present. The second set of Y plates share the same voltage supply but are connected the opposite way such that they deflect the beam by an equal amount as the first set thus permitting the ion beam to proceed parallel to its initial trajectory.

A set of stigmators are used to correct any inconsistency in the cross-sectional shape of the beam while the final focusing lens determines the final spot size at the target surface. Finally, a set of X/Y deflector plates are used to permit the beam to be raster scanned across the sample. The raster scan rate was originally controlled by a physical imaging unit, which also received the signal from the photomultiplier assembly. By synchronising the raster scan rate with that of the video signal, a real-time secondary electron image of the sample could be obtained. Magnification was also controlled by the physical imaging unit and was undertaken by confining the range of the raster scan.

With the ion beam successfully steered by the ion optical column to the target, a maximum current of approximately 200-300nA was incident on the target. The original specification of the primary ion assembly suggested a target current of the order of 1.5μA was possible. Despite much effort, such a magnitude was not achievable. Nevertheless, the experiments performed in these studies did not require excessive

primary ion current since careful erosion of the sample was crucial to successful depth profiling.

5.1.4 Liquid Metal Ion Source

The most extensive modification made to the TOF-SIMS apparatus was the installation of an Ionoptika IOG25 Liquid Metal Ion Gun (LMIG). The LMIG offers added flexibility to the system and provides far greater spatial resolution and beam control than the duoplasmatron ion source. The liquid metal ion source (LMIS) operation is based on the field ion emission process, whereby a high electrostatic field is set-up between the liquid gallium and the electrode. The liquid surface is distorted into a "Taylor" cone on the tip of the needle filament. When the field at the apex of this cone becomes sufficiently large, gallium atoms are evaporated and ionised enabling acceleration of the ions towards a target. The atoms that have undergone ionisation at the apex of the cone are constantly replenished resulting in a constant ion beam.

The LMIS is of the needle/reservoir type and the arrangement of the ion source, shown in Figure 5.8, consists of a gallium covered tungsten needle filament connected to two electrodes. The gallium reservoir located beneath the filament stores contains sufficient gallium to allow the ion source to be rated at 500mA.hr.

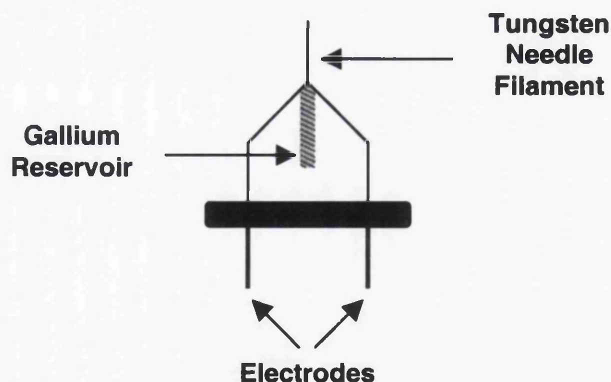

Figure 5.8: Schematic diagram of the liquid metal ion source.

The ion optical system is shown in Figure 5.9, and consists of the liquid metal ion source, two Einzel condenser lenses, stigmator and alignment units, aperture selection, blanking and fast pulsing deflection plates and X/Y raster plates. A choice of five apertures were available, ranging from 10μm to 1mm, the smallest of which permitted a

minimum ion beam diameter of ~50nm to be used which, along with sample currents as low as 20pA, allowed sub-micron structural features to be eroded. Prolonged use of the smaller apertures eventually leads to excessive erosion of the aperture thus increasing the diameter. In general, it was the largest aperture (1mm) that was used for depth profile analysis in these studies, since absolute spatial resolution was not required.

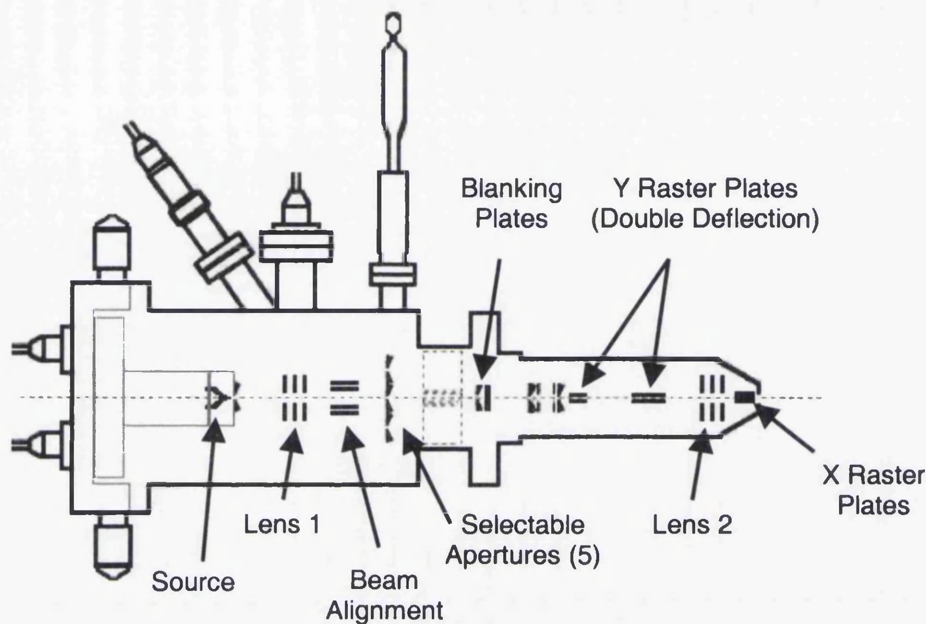

Figure 5.9: LMIG ion optical system.

The LMIG settings were controlled by two primary electronic units. The ion gun controller unit dealt with the settings of the lens, extractor, anode, stigmator and alignment voltages as well as control of the ion source heating current. Heating of the ion source was only required if the source could not be started by conventional means, e.g. following exposure of the ion source to atmosphere or when a new source was fitted. A fibre-optic connection sent control signals to a high voltage unit that fed the high voltage signals to the LMIG. A useful feature indigenous to the ion gun controller was automated control of either the extraction voltage or the emission current. The selected value to be held at a constant level was continuously monitored by the controller unit, which adjusted individual component voltages in order to maintain the set value. The control of the emission current was most valuable in these studies since it naturally permitted regulation of the current incident on the sample, which provided enhanced confidence in the fluence delivered to the sample.

The second controller unit was the RSU1000 raster scan unit, which also used a fibre-optic link to control the amplifier unit supplying high voltage signals to the raster plates.

The controller unit determined the image size/magnification, the ion beam position and the scan type, i.e. raster scan mode or single spot mode. The raster scan mode used a TV raster rate such that real-time imaging could be performed using the photomultiplier/scintillator assembly in conjunction with a video signal synchronisation unit. The high current density of the LMIG, coupled with its enhanced spatial resolution compared to the DP source permitted higher quality imaging of the sample surfaces such that precise targeting of the ion beam with an accuracy of the order of less than 10μm was possible.

A useful feature of the raster scan unit was the external scan option, which permitted an external source to control the raster scan plates and, therefore, the beam position, enabling the LMIG to be used for lithography, ion beam milling or raster scanning at variable rates.

LMIG pulsing

A dedicated pulser unit was supplied with the LMIG, which enabled primary ion pulses of between 1ns and 999ns to be used. Either the rising or falling edge of an external TTL trigger signal was required for the unit. For ease of timing synchronisation with the acquisition system, the trigger signal was sourced from the TOF acquisition unit (X129) and used the rising edge of one of the fast blanking signals for the duoplasmatron ion source. Therefore, the host computer maintained control over the mass spectrum acquisition and a recalculation of the mass spectrum calibration factors was all that was required to obtain a mass spectrum using the LMIG. Generally, a pulse width of 25-50ns (with a rise and fall time rated at 7ns) was used for experiments for optimum resolution.

Raster software

An Elphy Quantum nano-lithography system was acquired for this system to enhance the potential of the LMIG. The raster scan unit was controlled using the aforementioned external scan mode by a Raith control board installed into a PC. The software to run the control board is designed specifically for lithography purposes and, as such, the program has multiple parameters that can be varied to permit accurate dosing of the target sample over a specified area. Raster scanning the ion beam to erode a regular shaped crater is a fairly straightforward use of the system but it does allow substantial flexibility in the timescale of the routine.

5.1.5 Sample Manipulation

A sample holder constructed from brass and stainless steel was used to allow samples up to 2.5cm x 2.5cm x 1cm to be mounted. Variation in sample thickness was accommodated by a spring mechanism to hold the sample against the top plate. In order to admit the samples to the main chamber, the sample holder was placed onto an armature and locked in position via a pin mechanism. The FEAL, containing the sample holder and armature was then evacuated until a pressure in the 10^{-6} hPa range was achieved. The transfer valve, V1, between the FEAL and main chamber could then be opened, permitting the armature to be extended into the main chamber using a rack and pinion mechanism.

The sample holder slotted into a receptacle within the sample stage, whereby the pin mechanism retracted enabling the armature to be withdrawn and the transfer valve closed to restore UHV conditions. The sample stage itself was x-y adjustable using bellowed micrometer adjusters capable of translating the stage with an accuracy of 5μm.

5.1.6 Time-of-flight Reflectron Mass Analyser

The reflectron analyser is located at the end of the time-of-flight (TOF) tube and consists of 17 parallel meshed plates with increasing voltage towards the end of the tube. The reflectron is used to compensate for the kinetic energy spread of secondary ions of the same mass sputtered from the surface. The typical mass resolution of TOF mass spectrometer was approximately 3000 at 58 a.m.u..

In general, secondary ions are emitted from the target sample surface with a distribution of energies in the eV range. At the surface they are accelerated towards the TOF tube by a sample bias in the kV range (the extraction aperture of the TOF tube is held at 0V). In theory, all secondary ions should have the same energy as they enter the TOF tube hence the mass of the individual ions is inversely proportional to the velocity of the ions and, therefore, directly proportional to the flight time to the detector. However, the initial ion energy distribution is superimposed on the energy supplied by the sample bias (several keV), which results in a spread of flight times for ions of the same mass. The potential gradient of the reflectron slows the secondary ions and virtually reflects them back on their original path towards the detector, midway along the TOF tube. If two ions of equal mass but different energy are considered, both will enter the reflectron and the higher energy ion will penetrate deeper into the potential gradient before being

reflected back in comparison to the lower energy ion. If the reflectron is set correctly, both ions will reach the detector at the same time.

The reflectron voltage may be set manually, or a factory-preset value of 4.6kV may be selected, which is used in conjunction with a corresponding factory-preset sample bias of 4kV. A series of alignment plates within the TOF tube are used to compensate for any spatial variation in the secondary ions.

The detector system was of the dual channel plate design, using two Hamamatsu MCP F1208 channel plates. A –100V bias was applied to the first channel plate to prevent unwanted detection of electrons produced via ion collisions with components in the TOF tube.

5.1.7 Data Acquisition

Acquisition of mass spectrum data for this system was computer controlled and used software provided by VG, specifically designed for this system. The software was developed to for the OS/2 1.3 operating system, running on a 486-33MHz PC. Attempts to run the software and operating system on more modern computer systems were unsuccessful, due to the file allocation system of modern hard disk drive units. Despite this, the arrangement proved sufficient to obtain mass spectra, from which the integrated peak height values were used to plot the depth profiles shown in chapter 6.

The TOF software communicated and controlled the acquisition system via a purpose designed controller card connected to the ISA slot in the computer. This card used a dedicated fast parallel data bus (denoted X148) to communicate with the TOF acquisition unit (X129), which consisted of three plug-in boards, specifically the time-to-digital converter, the ion source timing controller, and the laser trigger unit. Since the laser system for RIMS was not employed in these studies, the latter unit was not relevant. The ion source timing unit controller in the TOF acquisition unit determined the pulsed timing of the primary ion source, with the pulse cycle rate, pulse width and number of cycles dictated by user defined values input into the host computer. The ion source timing unit controller was designed to send a TTL pulse train to the TOF deflection unit (X168), where the 5V TTL input signal was amplified to a high voltage pulse signal via the scan amplifiers, and sent to the fast blanking pulse plates in the ion

optical column. The timing unit was capable of pulsing the ion source at rates between 1kHz and 10kHz, with pulse widths between 40ns and 5μs.

The time-to-digital converter (TDC) operates by sensing the onset of pulses from the channel plates and stores the times of these events. This data is transmitted to a computer, which compiles a histogram of the number of ions detected in consecutive time intervals, known as bins. The TDC used in this system had a time resolution of 1ns and a maximum range of 500μs. The unit a typical count rate of 2MHz and also had a burst count rate in excess of 200MHz, when many ions arrived simultaneously. The effective dead time of the TDC was less than 4ns.

5.1.8 Acquisition of depth profiles

The depth profiles used for sample analysis are an assemblage of mass spectra acquired at set depth intervals. Each mass spectrum consists of a series of peaks plotted as a function of mass, derived from the flight time of the secondary ions from the sample to the detector. The height of each peak is simply representative of the number of ions detected for a specific mass. While the reflectron is used to compensate for the kinetic energy spread of equal mass ions, total compensation is virtually impossible to achieve in practice. Consequently, each mass spectrum will not consist of perfectly sharp peaks but a broader distribution of peaks astride the actual mass value. Integration of this distribution gives a more accurate determination of the true peak height although this procedure may introduce large errors where species of almost identical mass are also present in the mass spectrum. Such an effect is referred to as a mass interference, an example of which is the $^{28}Si_2^+$ dimer ion and $^{56}Fe^+$ ion. In such situations, high mass resolution is required to discriminate between the two peaks as there will be a very small mass difference between the two species.

Even when no mass interferences are present, it should not be assumed that an integrated value of the peak distribution at each mass is representative of the concentration of the species in question. As described in chapter 2, SIMS analysis is particularly sensitive to the sample matrix being probed since individual matrices substantially affect the yield of secondary ions that are sputtered from the sample surface. Oxygen, present as an oxide layer on most samples, is a particularly well-known species for inducing secondary ion enhancement. Two examples of mass spectra are shown in Figure 5.10.

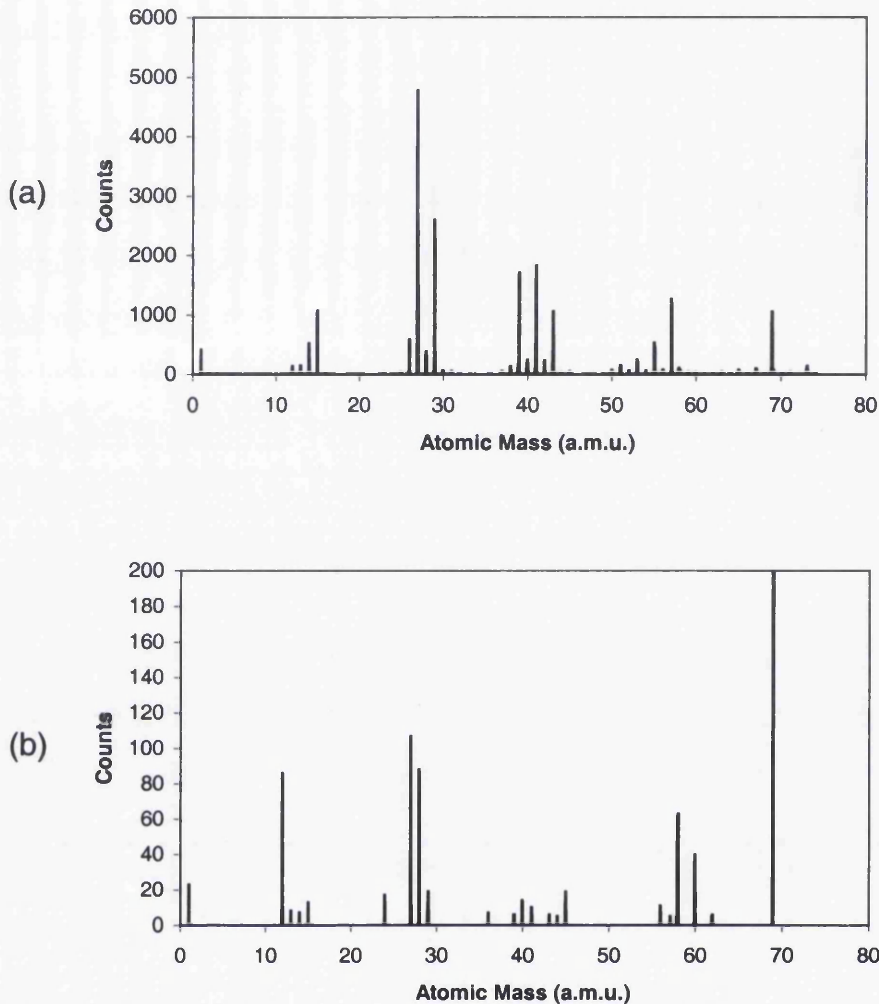

Figure 5.10: Mass spectra obtained from a Ni/SiC sample (a) with an oxide layer present, (b) with the oxide layer almost completely removed.

The mass spectrum in Figure 5.10 (a) was obtained from the surface layer of a Ni/SiC sample and displays a large number of peaks, which are associated with contaminants present on the sample surface. These contaminants are primarily hydrocarbon based and predominantly occur at odd mass numbers. The mass spectrum in Figure 5.10 (b) was obtained after the upper contaminated layers had been almost totally eroded. Consequently, fewer peaks are present in the spectrum. However, of great importance is the magnitude of the peaks themselves, which are substantially lower than those in Figure 5.10 (a), due to the eradication of the oxide layer, thus demonstrating the effect of the matrix under analysis.

Depth profiling consists of a series of cycles of mass spectrum acquisition followed by an erosion sequence. By logging the peak magnitude of each element required for

analysis in each mass spectrum, a profile is built up showing the variation of the elemental peaks as a function of depth, which can be used to determine chemical and structural variations within the sample.

5.1.9 Overlapping target location of primary ion guns

While a single ion gun may be used for both erosion of the sample and acquisition of mass spectra, it can be beneficial to use separate guns for these purposes. To this end, the use of two guns requires careful alignment on the target surface so that the beams overlap, as shown in Figure 5.11.

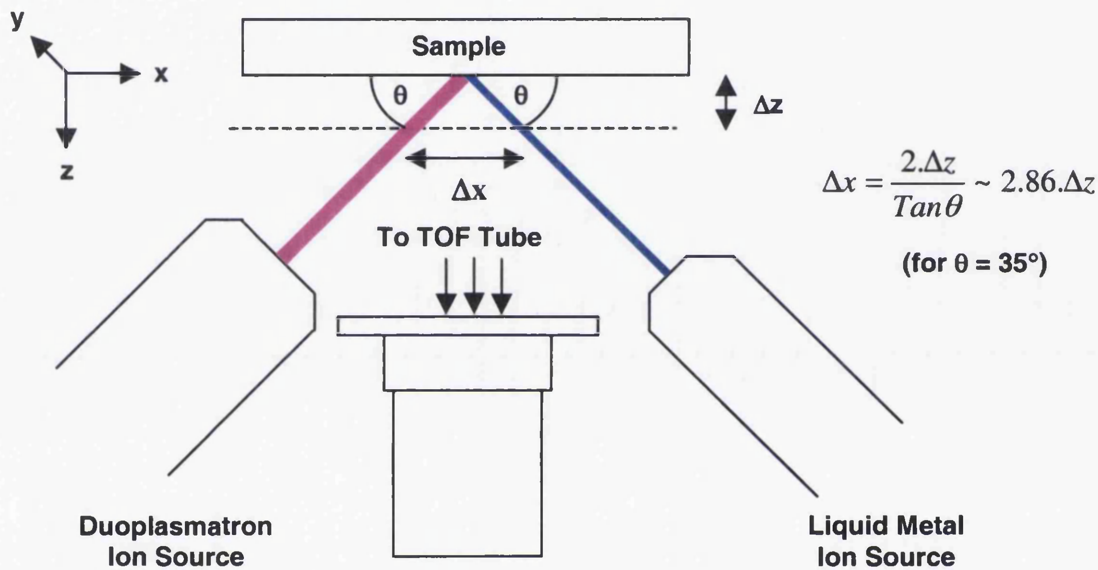

Figure 5.11: Schematic of ion gun overlap on target sample surface

There are a number of important factors that must be taken into account when attempting to overlap or coincide the target location of both guns. Issues such as sample positioning, primary ion voltage and target voltage are crucial in gaining beam overlap and maximum secondary ion yield. The TOF system has a limited area of extraction, hence for maximum secondary ion transmission a specific point on the sample surface is targeted, corresponding to the point of optimum extraction. Tests on the surface of various samples show that there is substantial variation in secondary ions detected depending on the position that the primary ion beam intercepts. An example of this is shown in Figure 5.12, where a mass spectrum was obtained at 25 separate spatial locations on a test sample.

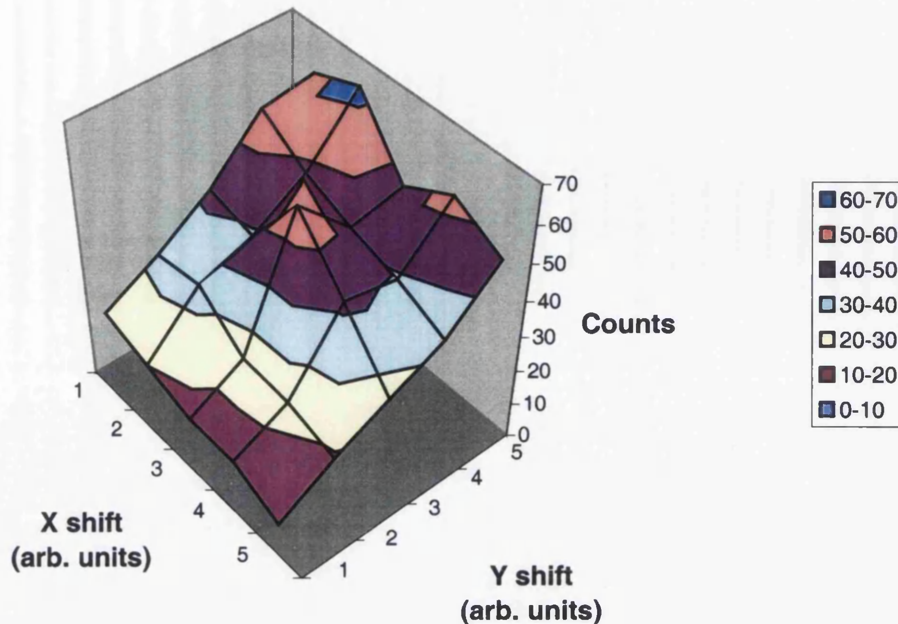

Figure 5.12: An example of signal variation with ion beam target location on the sample surface.

The 3D chart demonstrates how sensitive the target location is with respect to secondary ions detected. Consequently, when attempting to overlap the target location of both ion guns, the target coordinates for optimum extraction must be known. The coordinates of the optimum extraction point itself is not constant for all samples and since the ion guns are arranged such that the ion beams do not intercept the sample at normal incidence, this point is very much dependent on the distance of the sample surface to the extraction optics, i.e. the thickness or z-position of the sample. Figure 5.11, shows that the distance between the ion beam centres is approximately equal to $2.86.\Delta z$, where Δz represents the variation in z-distance from the position where the centres of the ion beams overlapped. The actual variation in thickness of all the samples will, at maximum, be of the order of several hundred nanometres, hence the shift of the target coordinates will be of the same order and should have a negligible effect on the secondary ion detection. Indeed, mechanical noise inherent to the system will have a far greater influence than this. However, it is the mounting of the samples that potentially causes the greatest problems. Due to the geometry of the samples (approximately 5mm x 5mm), it was required that the samples were adhered to the sample holder by using conductive tape. This means that significant variation can exist in the z-distance from the sample surface to the extraction optics for each sample. This dictated that optimisation of the target coordinates on the sample was required each time a new

sample, or indeed a markedly different area on the same sample, was profiled so that the optimum extraction point is targeted.

Alignment of the two guns is made more complicated due to the design of the LMIG mounting flange. While the duoplasmatron ion assembly is set up so that the X/Y raster plates are in correct alignment with respect to the sample, the LMIG mounting flange does not allow the same feature to be true for its X/Y raster plates. Consequently, a pattern design ablated by each of the ion guns was necessary to observe where the overlap occurs. With both ion guns used for sample analysis, it is essential that both guns target the same location on the sample surface each time a new sample is inserted.

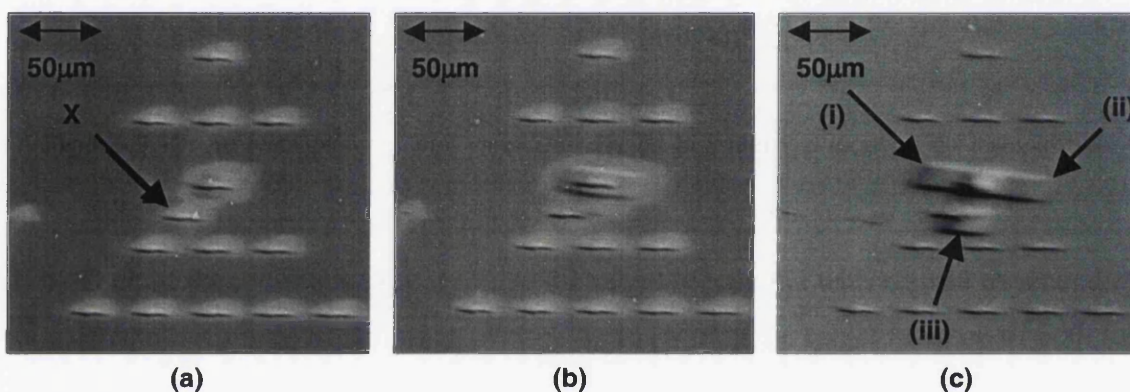

Figure 5.13: SEM images of Si sample showing method for determining ion beam overlap conditions; (a) series of spots ablated to form a partial grid by duoplasmatron ion source, spot X is located using half value settings for X and Y adjustment, (b) single LMIG ablated rectangle at optimum extraction location, (c) three further rectangles ablated by LMIG to observe LMIG translation with respect to duoplasmatron translation, (i) and (ii) located using X adjustment only, (iii) located using Y adjustment only.

To this end, a series of spots were ablated by the duoplasmatron ion source on a silicon test sample by varying the X/Y position of the beam by a set value each time. This formed a partial grid of spots, as shown in Figure 5.13 (a), permitting the spatial target location of the duoplasmatron ion source to be ascertained. A full grid was not described so that the direction of translation of the ion beam could be determined, hence the apparent "arrow" design used. A final spot, denoted by point X on Figure 5.13 (a), was ablated using an X/Y position halfway between set X and Y values such that the translation distance could be better related to the control settings. It should be noted that the spots ablated by the duoplasmatron ion source appear "squashed" as a result of the second Einzel condenser lens, which was set to give maximum current on the

sample. Naturally, depth profiles obtained with the duoplasmatron ion source used a beam profile that was far more uniform and regular.

A 25μm x 19μm rectangle was then ablated at TV rate by the LMIG at the optimum extraction location, as shown in Figure 5.13 (b). In this instance, it overlapped one of the spots ablated by the duoplasmatron ion source. Therefore, a depth profile could be obtained using these settings. However, since the optimum target coordinates is variable in all samples, the LMIG target location must be similarly translated. Consequently, beam overlap will no longer be maintained. Therefore, it is necessary to investigate how the LMIG ion beam is translated in comparison to the duoplasmatron ion beam.

Three further rectangles were ablated by the LMIG, as seen in Figure 5.13 (c). The beam was translated by set values using the X-raster plates of the LMIG to ablate the rectangles (i) and (ii), while rectangle (iii) was ablated after adjusting the Y-raster plate by an identical amount. It can be seen that the set X and Y translation values of the LMIG ion beam are less than that of the duoplasmatron ion beam, although the relative translation rate of each is known. Consequently, the two ion sources can be aligned with a fair degree of accuracy, even allowing for the misalignment of the LMIG mounting, evident in the SEM image. In addition, the magnitude of duoplasmatron spot (~ 500μm diameter) in comparison to the area sampled by the LMIG (~25μm x 19μm) means that there is large region from which the LMIG can sample.

5.2 Experimental Setup at Leuven

The system in Leuven is a time-of-flight mass spectrometer, similar to the one in Swansea, in which the sample under investigation is held in an ultra-high vacuum (UHV) chamber. The details of the Leuven setup is well described in publications by researchers who routinely use it for RIMS[3,4,5,6,7]. Considered here are some of the fundamental aspects included both for completeness and to gain an understanding of the system parameters required for depth profiling. Primary ions are incident on the sample causing secondary species (ions, neutrals, clusters, etc.) to be emitted. In SIMS mode, the secondary ions are extracted and accelerated to the mass spectrometer via a reflectron type analyser. In RIMS mode, the secondary neutrals that drift off the sample surface are photo-ionised by a laser system. The extraction is pulsed to eliminate as much secondary ion detection as possible while allowing the photo-ionised secondary

neutrals to be accelerated towards the detector. A diagram of the system is shown in figure 5.14.

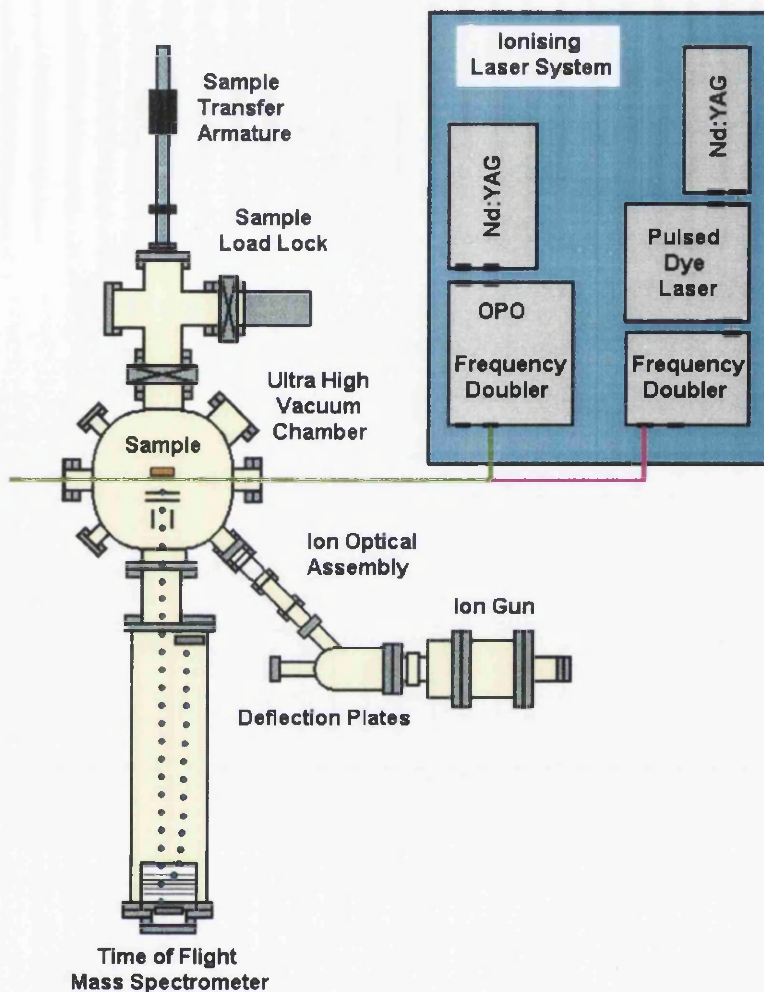

Figure 5.14: Plan view diagram of the TOF-RIMS apparatus at Leuven.

5.2.1 Primary ion column

The primary ion column produces the primary ions used for sputtering and directs and collimates them to the sample. The ion gun itself is an Atomica A-DIDA W610 commercially available unit. It uses a hot cathode to generate the ions that are accelerated with a kinetic energy selectively ranging from 0.1 to 15keV.

A gas feed to the ion gun supplies the Ar to be ionised. A tungsten filament within the gun is electrically heated to emit electrons. The electrons experience combined electric and magnetic fields forcing them to move spirally increase the probability of collisions with the Ar atoms. When the gas pressure is sufficient, the ionised Ar atoms form a plasma, which may be extracted. The ion source is floated at the acceleration voltage whilst the extraction electrode is held at a lower voltage to form a small potential

difference that is used to remove ions from the plasma. A subsequent acceleration electrode, held at ground, causes the ions to experience a second, much greater potential difference, which accelerates them towards the sample.

Prior to intercepting the sample, the ion beam passes through an array of deflection plates and lenses to steer and focus it onto a specified point on the sample. The beam first passes through a Wien filter to remove any contaminant ions then through an in-house built fast ion deflector to steer the beam through 45°. This removes any ions that have become neutralised and also any ions that do not have the specified energy. Any energy variance in the primary ions may be a result of collisions with other ions or recombined neutrals.

With only ions of the desired energy present, the ion beam passes through the ion optical assembly, which consists of three pairs of electrostatic plates and an Einzel lens. The first two pairs of electrostatic plates are mutually orthogonal and align the beam with the centre of the sample chamber. The final pair of plates are used if pulsing of the beam is required. The Einzel lens is a condenser lens used to focus the beam to a spot on the surface of the sample. The spot is of the order of 2-3mm in diameter. A diaphragm aperture may be installed prior to the sample chamber to reduce the diameter of the spot to approximately 1mm. This is useful if one wishes to remove as much of the Gaussian nature of the beam as possible. The ion beam then enters the sample chamber and is incident on the sample at an angle of 45°.

Crucial to efficient production of the plasma and transmission of the ion beam is the preservation of an adequate vacuum within the ion gun assembly and ion optical column. Pumping of the ion gun is undertaken by a Pfeiffer-Vacuum TMU 260 turbo-pump, which is backed by a Vacuubrand MD 4T oil free membrane pump. The fast ion deflector has a Pfeiffer-Vacuum TPU 240 turbo-pump, backed by an Edwards E2 M8 rotary vane pump. The remainder of the ion optical assembly is also pumped by the main chamber pumping system. The combination of pumps enables a base pressure of approximately 10^{-8} hPa to be achieved.

5.2.2 Main chamber and transfer system

The main chamber is spherical structure 40cm in diameter in which the sample is held and where the experiments are performed. The chamber has 12 separate ports of varying sizes to which other chambers, pumps, feedthroughs and viewing ports are connected. The largest of these ports are connected to the ion gun assembly, the mass spectrometer assembly, the sample stage manipulation drives, the sample load-lock assembly and the main chamber pumping system. The two ports parallel to the sample surface and at the same height contain UV-grade fused silica windows through which the laser beams are passed. These windows have a rated transmission efficiency of more than 85% for wavelengths ranging from 200 to 1900nm. Another of the ports is used is as an electrical feedthrough connected to the sample stage. This permits the measurement of current on the sample or enables a voltage to be put on the sample. The remaining ports are used for viewing within the chamber. The sample stage itself may be translated in three perpendicular directions and rotated in the horizontal plane. The translation accuracy is 0.025mm.

The sample load-lock assembly consists of a hinged entry window, a vacuum pumping system and a transfer arm to move the sample from the load-lock to the sample stage in the main chamber via a manual isolation valve. The pumping system uses a Pfeiffer-Vacuum TPU 240 turbo-pump, which is backed by an Edwards E2 M5 rotary pump to achieve a pressure of 10^{-8} hPa from atmospheric pressure within 1 hour.

The main chamber and mass spectrometer pumping system uses an array of pumps to produce a base pressure in the 10^{-10} hPa range. A Perkin Elmer TNB-X system consisting of a differential ion pump and a titanium sublimation pump (TSP) is used in conjunction with a Leybold Coolvac 800 cryopump. The ion pump and TSP enable both a fast rate of pumping and low pressures to be attained. The ion pump uses a high electric field to ionise gas atoms and implant them into plates within the pump. However, due to its high ionisation potential, the ion pump is less efficient at pumping down inert gases such as Ar, which is used in the experiments. To overcome this, the cryopump removes gas atoms via condensation and absorption onto extremely cold surfaces of 10-20K. The combination of these pumps holds the main chamber pressure at about 10^{-9} hPa during experiments.

5.2.3 Time-of-flight mass spectrometer

The system uses an R. M. Jordan Cie. AREF-850 reflectron time-of-flight mass spectrometer. Secondary ions of the sample under investigation created by sputtering or laser post ionisation in SIMS and RIMS respectively are accelerated by an electric field into the time-of-flight mass spectrometer. Three electrodes are used for this process. The first is the sample itself which, in the case of SIMS, has a high voltage applied to provide the first acceleration stage. The second electrode has an applied voltage approximately 200V lower to create a potential difference that extracts the ions. The third electrode is typically grounded which, in concert with the second, generates a much larger potential difference to accelerate the ions down the time-of-flight tube. The second and third electrodes have a constant applied voltage in all cases and have a small aperture that only allows a small polar angle of secondary particles to be transmitted. The aperture of the second electrode has a fine mesh added to maintain the uniformity of the electric field.

In RIMS experiments, the extraction process uses a pulsed scheme. The sample is held at ground potential when the primary ion beam is incident on the sample. Consequently, the majority of secondary ions emitted are forced back to the sample as a result of the voltage on the second electrode while the neutrals continue to drift off the surface. Less than 1μs after the ion beam strikes, the extraction field is activated. The neutrals photo-ionised by the laser system and are extracted and accelerated by the electric fields down the time-of-flight tube.

The time-of-flight can also be used in two modes; linear mode, which detects ions at the end of the time-of-flight tube; and reflectron mode, which deflects the secondary ions through almost 180° towards another detector. The advantage of linear mode is that it enables a greater number of secondary ions to be registered although the mass resolution is quite low, of the order of 200 at 58 amu. The low resolution is caused by the kinetic energy spread of the secondary ions. When the secondary ions are accelerated from the sample, there is inevitably a variation in their kinetic energy and spatial location. The reflectron consists of a series of electrodes with increasing electric potential, which causes it to act as an electrostatic mirror. Higher energy ions travel deeper into the reflectron before being stopped and sent back. This eliminates much of the kinetic energy and spatial variation of the secondary ions, thus improving the mass resolution of the technique. In this system, the mass resolution ($M/\Delta M$) in reflectron

mode typically improves to approximately 800 at 58 amu. However, in reflectron mode, the secondary ion detection efficiency is reduced. Consequently, the reflectron mode is most commonly used in SIMS experiments where many secondary ion species are present and mass resolution is of prime importance. Generally, if an efficient resonant ionisation scheme is used that yields a high secondary ion population, the analyser may be used in linear mode since RIMS is element sensitive. However, when wavelengths are used that may cause non-resonant ionisation of species of similar mass number to the species of interest are used or where very low yields of the species of interest are available, the reflectron mode may be used in RIMS.

The detection system employs an R. M. Jordan Cie. C-0701 and C-0726 dual microchannel plate (MCP) detector to convert the ion signal to an amplified electronic signal. The plates have a sub-nanosecond rise time and a gain of the order of 10^7. The output signal is then fed to an EG & G Ortec 535 fast quad DC amplifier where it is amplified 100 times and sent on to a Textronix TDS 420 digital oscilloscope. An example of the typical signal produced is shown in Figure 5.15.

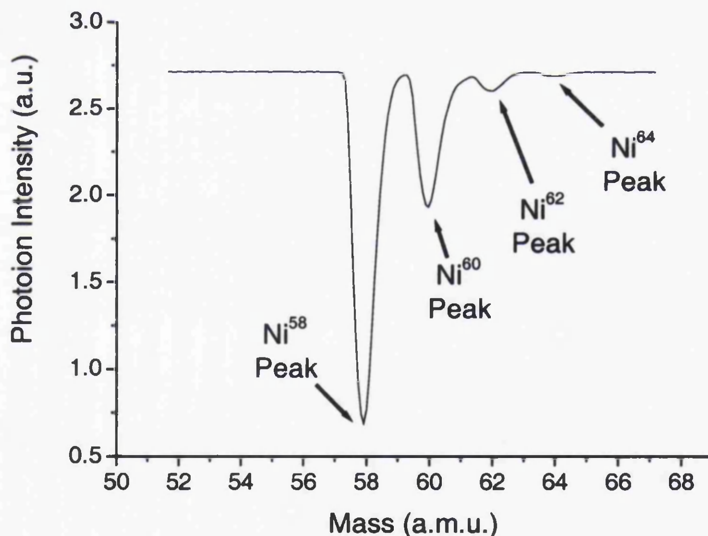

Figure 5.15: Example of typical RIMS mass spectrum of Ni obtained from a Ni/SiC sample.

By using the oscilloscope to select two timing marks between which all signals are integrated, a single peak value can be obtained which is then sent via a GPIB interface to a computer system, which uses a specifically designed program to plot the value as a function of experiment time. Through knowledge of the ion pulsing scheme, this experiment time is converted into true exposure time, from which the fluence can be

calculated. As the integrated signal data points are amassed, a depth profile is built up, revealing chemical and physical variations within the sample.

5.2.4 Ionising laser systems

The ionising laser systems are the single most important aspect when dealing with RIMS studies as opposed to SIMS studies. In order to obtain efficient ionisation (and excitation), high photon fluences must be used, necessitating the use of pulsed laser system. Since RIMS is a highly selective process, the laser systems must be capable of operating over a wide spectral range, i.e. they are tuneable, and the laser light itself at these specific frequencies must have a very narrow bandwidth to prevent photo-ionisation of alternative species.

The Leuven system has two independent laser systems consisting of a pulsed Nd:YAG pumped dye laser and an optical parametric oscillator, also pumped by a pulsed Nd:YAG laser, which are situated in a temperature controlled (within 1°C) room, separate from the time-of-flight apparatus. The output laser light is directed through a series of 90° fused silica prisms to the sample chamber of the TOF system, which the light enters via a fused silica window (UV grade). The laser light leaves the system (after photo-ionisation) through an identical fused silica window on the opposite side of the sample chamber, whereupon it is directed to a pyroelectric power meter for measurement of the laser pulse energy.

Pulsed Dye Laser (PDL) System

The pulsed dye laser (PDL) system uses the second harmonic, 532nm wavelength of a Spectra Physics GCR 150 Nd:YAG laser, with a pulse length of 6ns and 320mJ pulse energy, to pump a Spectra Physics PDL-3 dye laser. The laser light from the dye laser is then frequency doubled using a Spectra Physics WEX-1 frequency-doubling device containing a 58° KD*P crystal. The dye used in the dye laser dictates the tuning range of the emitted laser light. Using different dyes permits a tuneable wavelength range of 577-834nm. In these studies, DCM dye was used to give a dye laser output wavelength range of 610-670nm, with linearly polarised output pulses of ~50mJ per pulse. Following frequency doubling, ultraviolet laser pulses of approximately 5mJ energy and 5GHz bandwidth are directed to the TOF system. At the ionisation location, the energy is ~1-2mJ.

Optical Parametric Oscillator (OPO) System

The optical parametric oscillator (OPO) system uses the third harmonic, 355nm wavelength of a Spectra Physics GCR 230 Nd:YAG laser, with a pulse length of 6ns and 440mJ pulse energy, to pump the two individual optical parametric oscillators of a Spectra Physics MOPO-730 system. The OPO system itself is not a laser system but produces light with the characteristics of laser light and is tuneable over the wavelength ranges 410-690nm and 730-1800nm via the signal and idler optical waves respectively. A high modulation diffraction grating in the master oscillator ensures that the output beam has a narrow bandwidth. This output beam is used to "seed" the second oscillator, the power oscillator. This system of operation results in output pulse energies of 50mJ for the signal beam and 20mJ for the idler beam. A bandwidth of 6GHz can be achieved over the complete tuning range. A Spectra Physics FDO-1 frequency-doubling device is used to provide UV light. The two BBO crystals used in this device permit frequency doubling of the signal beam and the idler beam. The frequency doubled range of the signal beam is 225-340nm, with a typical energy of 4mJ, while the doubled idler beam output is tuneable over the range 370-450nm, with a typical energy of 1mJ. Both beams have a spectral bandwidth of 8kHz.

A more detailed explanation of both laser systems used in these studies can be found in the theses by Vandeweert[3] and Bastiaansen[4].

5.2.5 Time synchronisation of system

The time synchronisation of the components within the system is fundamental when attempting RIMS studies. Two Stanford Research Systems DG535 delay generators are used to control the synchronisation by inserting time delays where necessary. The time synchronisation scheme is shown in Figure 5.16.

The entire timing scheme operates at 10Hz, which is determined by the internal clock of one of the delay generators. The flash-lamp triggers of the Nd:YAG lasers are triggered first after which the Q-switches are triggered allowing the lasers to fire. The Q-switch delay times are set such that maximum output is achieved, hence the time between the flash-lamp trigger and Q-switch trigger must be held constant . The primary ion pulse and Q-switch trigger times are set relative to one another in order that the laser pulses intercept the plume of neutral species sputtered from the sample surface. When a short ion pulse is used (of the order of 300ns as used for probing sections of the velocity

distributions), the accuracy of this temporal overlap becomes paramount. The delay time is determined by measuring the time at which the ion current is incident on the sample in comparison to the arrival time of the laser pulses, measured using a fast photodiode.

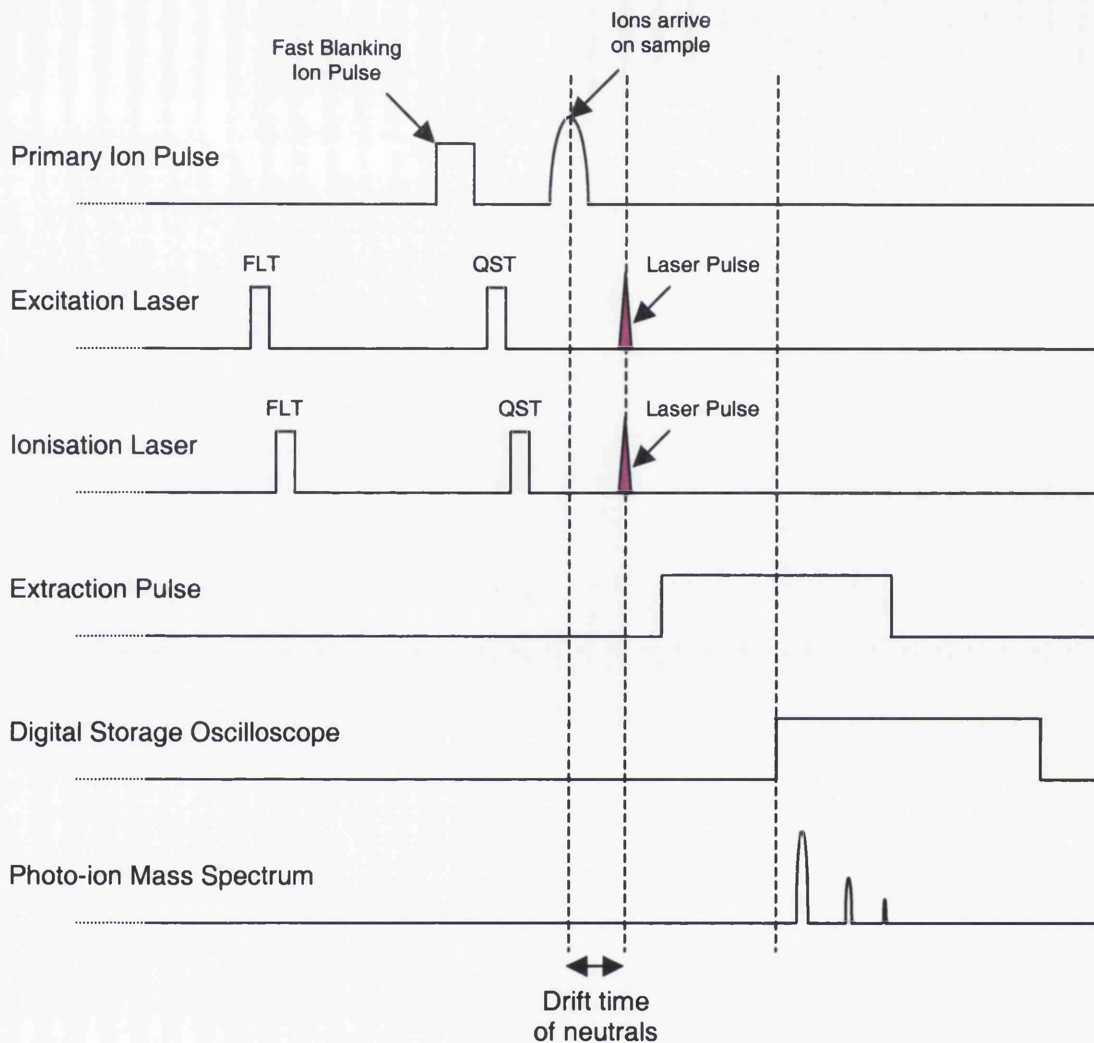

Figure 5.16: Time synchronisation scheme for a pulsed ion time-of-flight RIMS experiment using separate excitation and ionisation lasers. FLT represents the flash-lamp trigger, QST represents the Q-switch trigger,

5.3 Summary

This chapter has outlined the basic components of each experimental system used in these studies. The results sections will develop on the experimental parameters specific to the depth profiles and often refer back to details within this chapter. It is also hoped that some of the equipment description, particularly of the Swansea system, will help in its continued development and operation for future users.

5.4 References

[1] R. Jones, University of Wales Swansea, PhD Thesis, (1996).

[2] C. Abrahams, University of Wales Swansea, PhD Thesis, (1997).

[3] E. Vandeweert, Katholieke Universiteit Leuven, PhD Thesis, (1997).

[4] J. Bastiaansen, Katholieke Universiteit Leuven, PhD Thesis, (2003).

[5] J. Bastiaansen, F. Vervaeke, E. Vandeweert, P. Lievens, R. Silverans, Spectrochimica Acta **B58**, 1147 (2003).

[6] R. Silverans, J. Bastiaansen, V. Philipsen, E. Vandeweert, P. Lievens, Nucl. Instrum. Meth. **B182**, 127 (2001).

[7] E. Vandeweert, P. Lievens, V. Philipsen, R. Silverans, Spectrochimica Acta **B54**, 1219 (1999).

Chapter 6: TOF-SIMS Measurements

6.1 Introduction

This chapter presents the results of TOF-SIMS measurements on Ni contacts to SiC. The samples themselves consisted of as-deposited Schottky contacts and Ohmic contacts, produced by post-annealing in excess of 900°C. The aim of these experiments is to identify chemical changes occurring within the samples, specifically relating to the interfacial region between the Ni contact layer and SiC substrate. Research on Ni/SiC contacts is an area of current interest and recent transmission electron microscopy (TEM) and x-ray photoelectron spectroscopy (XPS) studies[1,2,3] have indicated a chemical dependency on the electrical properties of the contact with voids, Ni-silicides and carbon clusters thought to play a role. These experiments also explore the capabilities of depth profiling to extend these measurements using the technique of resonant ionisation mass spectrometry (RIMS), as discussed in chapter 7.

Described first within this chapter are the processes involved in optimising the system for acquiring depth profiles of thin-layered systems. Bombardment of the sample with variable energy and variable mass primary ions is taken into account by modelling and simulation of the interaction of the primary ions with component matrices of the samples. The simulation is undertaken by means of the "Stopping Ranges of Ions in Matter" program SRIM 2003 2.0[4]. Thus, the ideal experimental parameters for bombardment on this material system are established. Implementation of the ideal parameters is then discussed, relating specifically to the target overlap of the two primary ion sources.

Using the method described in chapter 5, section 5.1.8, mass spectra are obtained from Schottky and Ohmic samples at specified depths. The individual C, Si and Ni signals from each mass spectrum are determined and plotted as a function of depth to produce full depth profiles of the Schottky and Ohmic samples. The results of different primary ion conditions are presented to illustrate the development of the technique. The results of using two separate primary ion sources for sample erosion and acquisition of mass spectra are discussed and developed. A standard technique of rastering the primary ion beam to erode a square crater is also reviewed before the process of using a defocused ion beam for erosion and a partially refocused beam for sampling using the same source is fully explored and analysed.

A conclusion section at the end of the chapter reviews the results and analysis of the depth profiles obtained and puts forward a model for describing the structure of each of the sample types.

6.2 Optimisation of TOF-SIMS parameters

As with any experimental technique, it is essential that the experimental apparatus is set up to yield the best possible results. There are many variables that can affect the mass spectrum obtained in TOF-SIMS. The ideal mass spectrum should consist of a series of sharp, well-defined peaks of substantial magnitude at the appropriate mass unit on the x-axis. The peak sharpness is primarily determined by the pulse width and alignment of the primary ions, along with the magnitude of the sample bias, TOF alignment, and reflectron analyser voltages. The peak magnitude is determined by the aforementioned factors coupled with the primary ion energy, current and species, the sample characteristics, and the channel plate detector voltage. System settings aside, the absolute magnitude of individual peaks is naturally determined by the ion yield of the corresponding element, or compound.

The full description of the TOF-SIMS system can be found in chapter 5. The optimum primary ion pulse width for this system is in the range of 40-50ns. A shorter pulse width limits the number of secondary ions that may be liberated per pulse, whereas longer pulse widths result in a wider range of starting times of same mass ions thus increasing the width of the peaks and reducing mass resolution. A 4kV sample bias was used to accelerate the secondary ions to the TOF tube in all mass spectrum acquisitions.

6.2.1 Selection of primary ion source for analysis

The ion species used as the impact source greatly affects the surface and subsurface kinetics that take place during sputtering. As discussed in chapter 2, the optimum bombardment conditions favoured a low energy, high mass primary ion intercepting the sample at normal incidence to reduce ion beam intermixing and roughening of the sample [5,6]. Due to the constraint of a fixed sample stage on this TOF-SIMS system, the angle of incidence is set at 35° (neglecting sample bias conditions). Consequently, the samples used in these studies required sub-micron thickness Ni contact layers to prevent excessive roughening affecting the depth profiles. Nevertheless, with the availability of two different ion sources, the energy and mass of the primary ion were parameters that

could be varied to yield the best profile possible. The duoplasmatron ion source was capable of exploiting argon and oxygen in elemental ionic form along with associated oxygen molecular species, while the mono-isotopic gallium source of the LMIG gave the added option of $^{69}Ga^+$ ions.

Oxygen has the advantage of enhanced secondary ion emission when used as a primary ion, although its reactivity with metals to form an oxide effectively changes the chemistry of the sample area under analysis, hence it is not considered for these experiments. As a noble gas, argon is the preferred choice when the preservation of sample characteristics is more important than the secondary ion yield. Due to its greater atomic mass, gallium would initially appear to be the best candidate for high resolution depth profiling. However, the extraction assembly of the LMIG typically operates in the 15-25kV region compared with 4-10kV for the duoplasmatron source, hence the duoplasmatron better fits the low energy criterion required for high resolution.

Therefore, it is essential to quantify how each of the primary ion species at their specific initial kinetic energies interact with the components of the samples. By performing SRIM calculations on the material systems present in this investigation using "The Stopping and Range of Ions in Matter" program, SRIM 2003.20, by Ziegler and Biersack [4], the projected longitudinal range of primary ions into the bulk could be modelled. The effect of primary ion mass is demonstrated in Figure 6.1 where 50 of each of the primary ion species at 10keV impact a variety of component matrices present in the annealed Ni/SiC samples at an incident angle of 35°. The component matrices chosen represent the most abundant matrices that would be present in the depth profiling of the Ni/SiC samples as determined from work by other authors.[1,2,3] The range stated for each model calculation represents the average longitudinal depth to which the primary ions are projected. The straggle, σ, is defined as the square root of the variance, effectively the standard deviation, given by:

$$\sigma = \sqrt{\frac{1}{N} \times \sum_i \left(x_i - x_{ave}\right)^2} \qquad \textbf{Equation 6.1}$$

where N is the number of events, x_i is the projected range of the ith event in the x-axis and x_{ave} is the average projected range. It should be noted that the actual range and straggle values stated in Figure 6.1 are those obtained following calculations using 5000 primary ions whereas the images use just 50 primary ions in the interest of clarity.

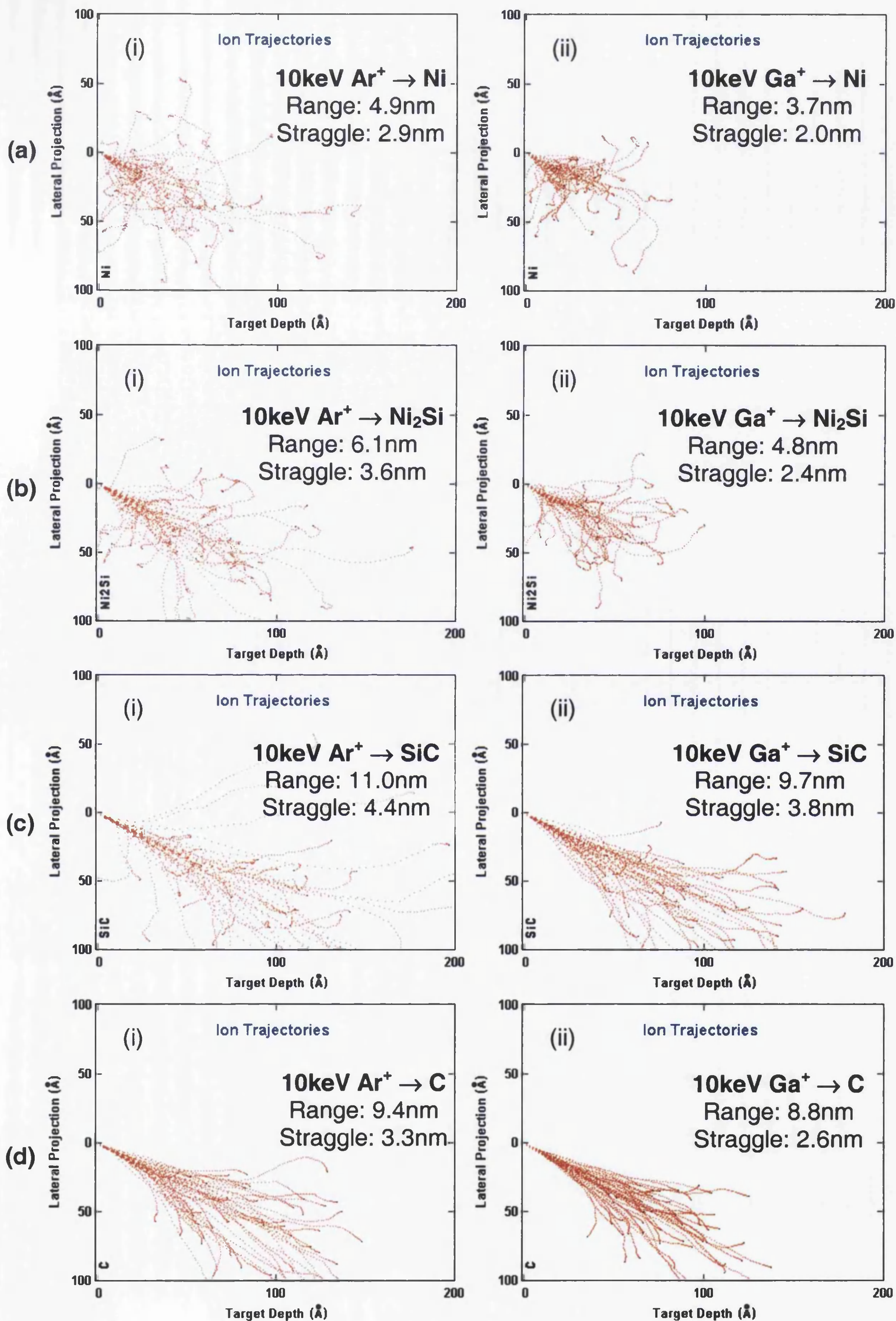

Figure 6.1: SRIM calculations for; (i) argon and (ii) gallium primary ions projected into Ni/SiC component matrices at 10keV; (a) Ni contact layer, (b) Ni_2Si, suggested to be the prevalent Ni silicide formed during the annealing process, (c) SiC substrate, (d) C, which forms in clusters when annealed >900°C. (The left margin represents the target surface).

Beyond 400 primary ions, there is negligible variation in the projected range and straggle. 5000 events were chosen as a random value an order of magnitude greater to ensure statistical rigidity in a convenient timescale, i.e. additional events do not alter the projected range and straggle. It should be noted that the simulations do not allow for progressive sample erosion and hence are used only for comparative purposes.

The models show that the average longitudinal range of the Ar^+ ions is greater than that of the Ga^+ ions in all cases because the Ga^+ ions transfer more energy in the early collisions and hence come to rest more rapidly than the Ar^+ ions. It can also be seen that the ratio of the average longitudinal range of the Ar^+ ions to the Ga^+ ions in each matrix decreases from Figure 6.1 (a) to (d), just as the ratio of primary ion mass to target atom mass increases. Indeed, in model Figure 6.1 (a) (i) the bombarding Ar^+ ion has a lower atomic mass than the target atoms while the opposite takes place in Figure 6.1 (a) (ii). Consequently, the Ar^+ ions undergo substantial recoils with many of the incident ions undergoing a change of direction of close to 180°, consistent with the impact of a smaller incident atom striking a larger target atom. As a result, both the longitudinal and lateral range are substantial. The SRIM calculations at 10keV and 35° incident angle predict that the average projected lateral range of Ar^+ ions into Ni is 29% greater than that of Ga^+, while the average projected longitudinal range is 38% greater. Since the sputtered atoms originate from the volume dictated by these ranges, it is clear that the use of the lower mass Ar^+ ion for depth profiling is inherently detrimental to the ultimate depth and spatial resolution. Therefore, at identical energies, the heavier primary ion is preferable to use, consistent with the theory. However, the duoplasmatron ion source is more adept at operating at accelerating voltages well below 10kV. To this end, further SRIM calculations were performed using Ar^+ and Ga^+ primary ions striking Ni and SiC targets at 35° at energies between 0.5keV and 25keV to observe the variation of the average projected ion range with incident energy of the primary ions. A summary of these results can be seen in Figure 6.2. As to be expected, there is very little difference between the projected ion ranges of both primary ions into a SiC target at each energy increment since both ions are substantially heavier than the SiC component atoms. The greatest difference occurs when bombarding Ni, where the Ga^+ ions come to rest much earlier than the Ar^+ ions, as was shown in Figure 6.1 (a).

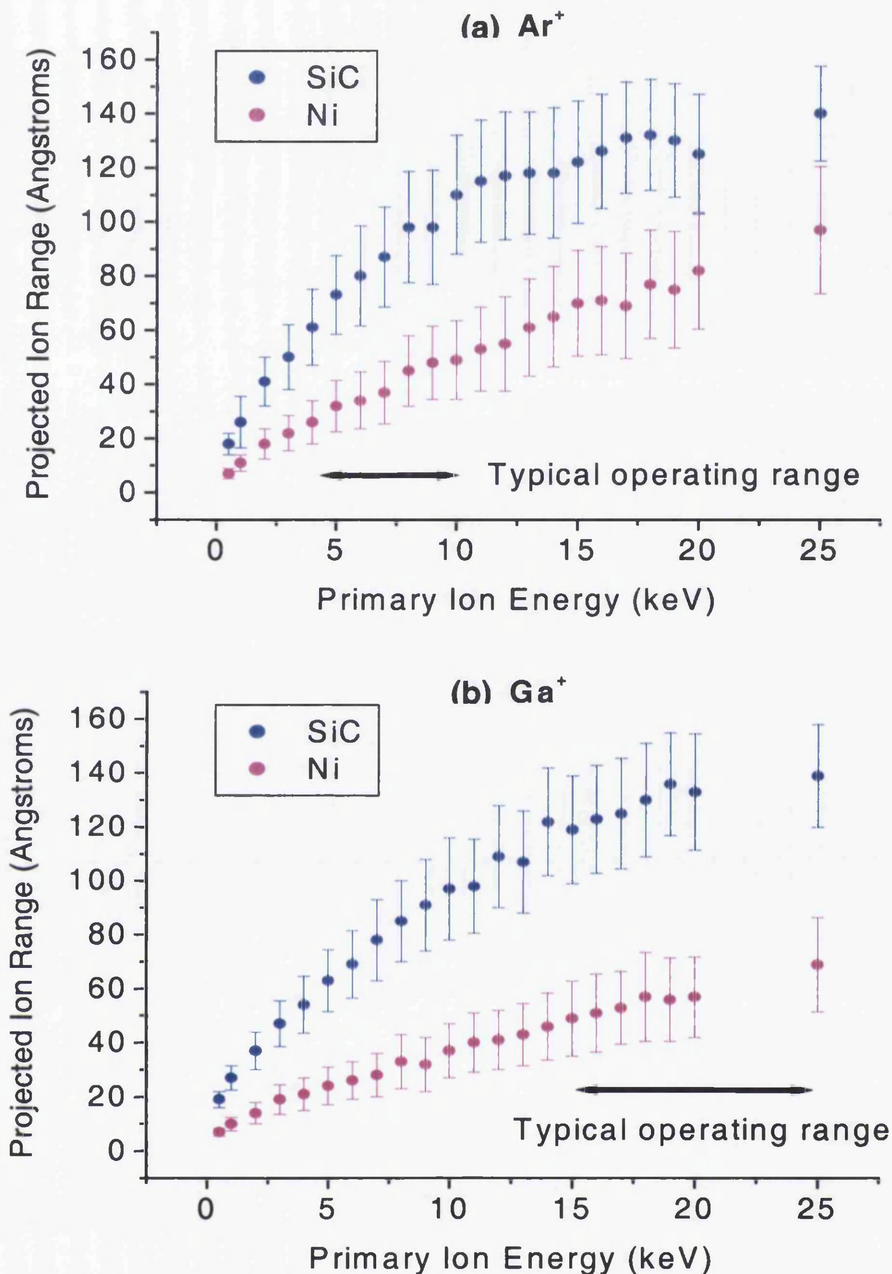

Figure 6.2: Plot of average projected ion range against incident energy of (a) argon and (b) gallium primary ions. The straggle is represented by the error bars given for each data point.

When the typical operating range of both ion guns is taken into account, it can be seen that it is in fact beneficial to utilise the duoplasmatron ion source when ultimate depth resolution is required simply due to its lower operating energy range. However, since the method of depth profiling with this system requires a defined period of sample erosion followed by an acquisition routine to obtain a mass spectrum, it can be advantageous to make use of both ion sources. This is because the duoplasmatron ion source typically has a minimum beam spot diameter of the order of 100μm, although at this diameter, an excessive erosion rate becomes an issue. Nevertheless, increasing the

diameter appropriately reduces the erosion rate and since the LMIG is capable of producing a spot at least two orders of magnitude smaller than the duoplasmatron source during routine operation, it is relatively simple to align both guns so that the LMIG impacts the centre of a crater eroded by the duoplasmatron source. This means that the LMIG should be able to sample the flattest region of the eroded crater thus yielding the best depth resolution. Therefore, the duoplasmatron ion source may be used for low energy erosion while the LMIG may be used for acquiring the mass spectrum. It is essential, however, that the process of spectrum acquisition with the LMIG does not exceed the static SIMS limit, which would cause excessive erosion at the acquisition location on the sample surface.

In conclusion, the use of simulations to predict the projected range of the ions within the sample, coupled with the operational specifications of the equipment have established that the duoplasmatron ion source is an excellent choice for sample ablation due to its ability to project 4keV Ar^+ primary ions with limited knock-on and intermixing effects within the target sample and thus enhanced depth resolution. The LMIG is useful to employ as the acquisition ion source due to the smaller spatial dimensions of the ion beam spot, which permits it to sample a small region within the crater ablated by the Ar^+ ion beam, whilst remaining within the static SIMS limit. This largely negates the effect of any non-uniformity in the Ar^+ beam profile, which would cause a non-flat crater to be formed.

6.3 TOF-SIMS depth profiles of Ni/SiC samples using both ion sources

Upon completion of the studies to determine the best parameters to use for depth profiling, the first Schottky sample was depth profiled using the duoplasmatron ion source set to spot mode to erode a 500μm crater on the sample using 4keV Ar^+ ions, while the LMIG was raster scanned and used 15keV Ga^+ ions to acquire the mass spectra in between the erosion routines from a 25μm x 25μm region of the centre of the eroded crater. A 2kV bias was applied to the sample during erosion in order to further reduce intermixing induced by the Ar^+ ions whereas a 4kV bias was used when acquiring mass spectra. Alignment of the two ion guns is described in chapter 5, section 5.1.9.

6.3.1 Time-to-depth conversion of profiles

The initial profile obtained during an experiment plots the secondary ion intensity as a function of sputter time. In order to convert the sputter time to depth, D_z, eroded on the sample, the following relationship was used:

$$D_z = \delta \cdot Y \cdot d^3 \qquad \textbf{Equation 6. 2}$$

Where δ is the fluence delivered to the sample, Y is the sputter yield determined using the formula developed by Yamamura et al [7] described in Chapter 2, Section 2.2.1 and d is the interatomic distance of the target material. The fluence, δ, delivered to the sample is given by:

$$\delta = \frac{I \cdot t}{q \cdot A} \qquad \textbf{Equation 6. 3}$$

where I is the primary ion current (corrected for secondary electron current), t is the exposure time of the ion beam to the sample, q is the value of the elemental charge and A is the cross-sectional area of the ion beam exposed to the sample surface.

Converting from time to depth on a layered sample can be very complicated, particularly when reactions occur between layers since the sputter yield varies from one matrix to the next. It should be noted that all of the profiles converted to depth use the relevant sputter yield value of Ni over the whole scale. However, since Si and C have sputter yields substantially lower than Ni, the depth scale beyond the interface may become exaggerated. Consequently, the profiles also retain a sputter time axis in addition to the depth axis.

Of crucial importance when depth profiling is ensuring that the acquisition routine for obtaining mass spectra contributes as little as possible to further sample erosion, i.e. static SIMS conditions are maintained.

6.3.2 Depth profile of Schottky Ni/SiC sample using two primary ion sources

The first depth profile obtained using the method described in chapter 5, section 5.1.8, is shown in Figure 6.3 and was on a Ni/SiC Schottky sample, consisting of a 200nm Ni contact layer on a SiC substrate with a 50nm Ohmic Ni back contact. The sample was produced in UHV via the procedure described in chapter 4, section 4.4.

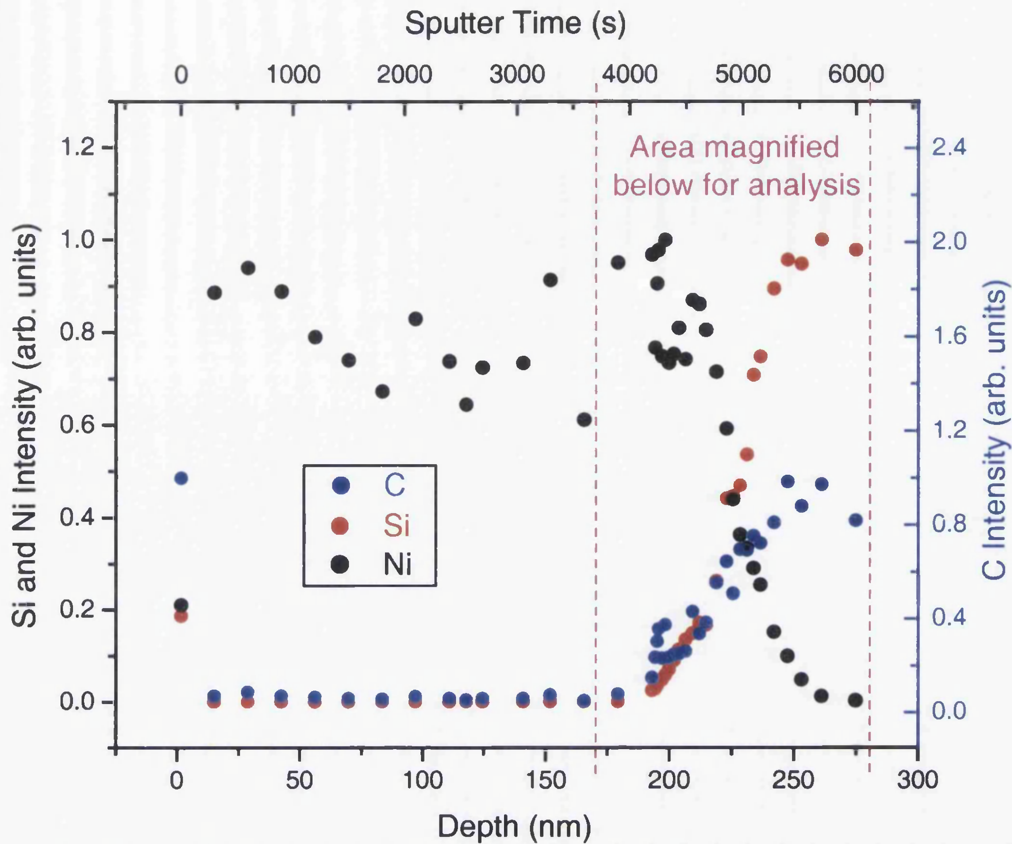

Figure 6.3: TOF-SIMS depth profile of as-deposited Ni/SiC Schottky sample (4keV Ar^{+}, 15keV Ga^{+})

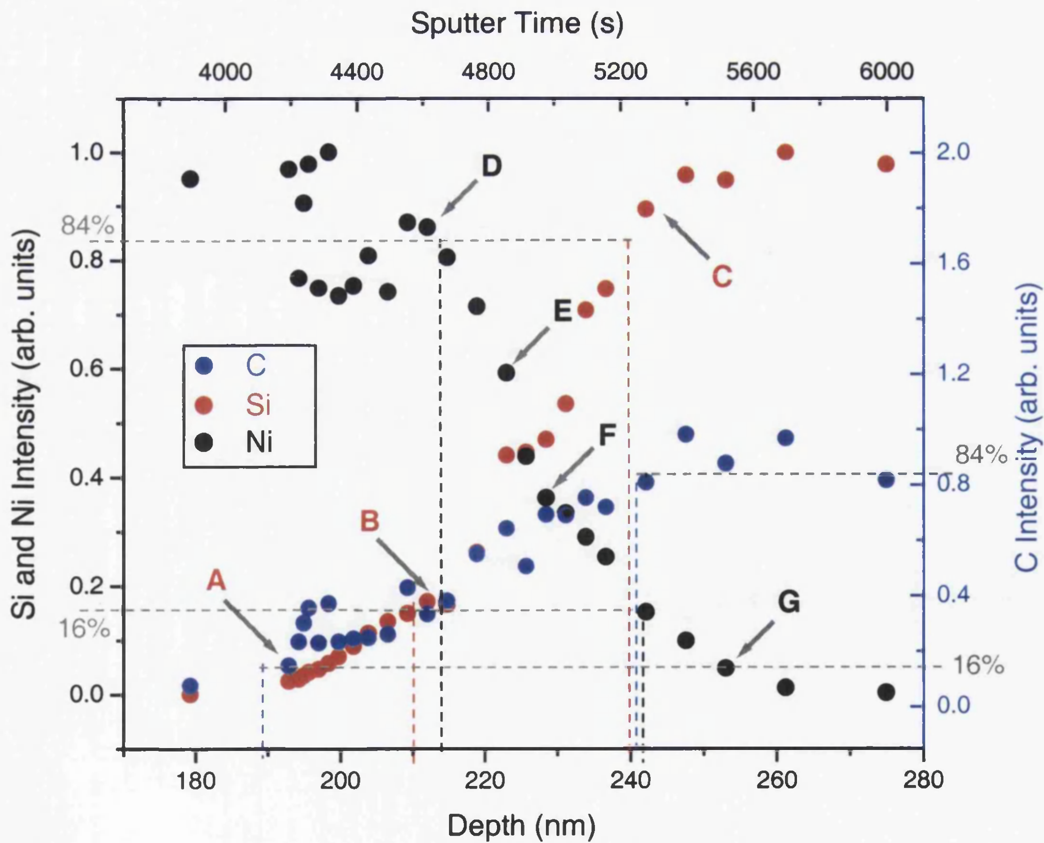

Figure 6.4: Magnified section of Figure 6.3. Points A-G are marker points of interest.

A basic normalisation routine of each signal to its maximum value was used to highlight points of interest in the profile. The presence of the Ni contact layer and top oxide layer can be quite clearly observed, as is the interfacial region whereby the Ni intensity falls off with a corresponding increase in the Si and C signals, representing the progression into the SiC substrate.

The first thing to note is that the depth scale of the profile, derived using the time-to-depth formula is successfully scaled, permitting confidence in the technique. When depth profiling using SIMS, the oxide layer causes substantial fluctuation in the secondary ion intensity, while the presence of hydrocarbons at the surface result in a large C signal as can be seen from the profile. Even after the oxide layer is eroded completely, secondary ion variation within a homogeneous sample will still be present until sputtering has reached equilibrium, whereby the concentration of primary ions in the sample reaches a constant level.[8]

Since it is the interface region that is of primary interest, a magnified version of the section is shown in Figure 6.4. In order to aid analysis, a measurement on each signal is incorporated that measures the depth corresponding to 84% and 16% of the intensity during a transition phase, allowing the relative magnitude of the interface width to be judged. This 84-16 measurement is more usually used at sharp interfaces between two layers in order to determine the depth resolution of a system.[9] Nevertheless, it provides a quantitative analysis between samples where reactions may occur as a result of their preparation process. The apparent width of the interface from this depth profile is approximately 60-70nm. A number of factors affect this value, most notably the intermixing caused by interaction of the ion beam with the sample. The SRIM results in Figure 6.2 show the average longitudinal projected range of 4keV Ar^+ ions to be 2.7 ± 0.8 nm in Ni and 6.1 ± 1.4 nm in SiC. While it can be predicted that the magnitude of intermixing may be of a similar order for a very thin contact layer, the SRIM models used neglect the effect of time evolution of erosion of the sample surface. In conjunction with the cumulative knock-on of Ni atoms through the contact layer, the interface will appear broadened to a greater degree than can be inferred from the simulations. Another factor that will add to the apparent width of the interface when depth profiling is ion beam inhomogeneity. Variation in the current across the ion beam cross-section will cause an uneven crater to be formed. Consequently, the ion pulse used for acquisition will sample material at different depths as the target is eroded, even

positioned at the centre of the crater such as it is. These factors, in combination with ion beam induced roughening, inherently reduce the depth resolution of the depth profile. Nevertheless, while a proportion of the apparent interfacial width may be attributed to experimental factors, it does not preclude the possibility that an element may be due to the presence of a reaction occurring between the Ni and SiC.

The 84-16 values obtained for Ni and Si were quite similar at 28nm and 30nm respectively. This implies that the increase in Si concentration through this region is at the expense of Ni concentration as would be expected at a sharp interface, hence the broadening of the apparent interface would be due to ion beam intermixing. However, the form of the two signals in this region suggests a further effect is taking place. At the start of the interface (point A), the Si signal undergoes a gradual rise followed by a sharper rise at point B. However, the Ni signal shows a great deal of fluctuation at the start of the interface, potentially indicating changing matrix conditions, followed by a decrease at point D, the rate of which increases at point E then reduces again at point F from which it follows a fairly linear decrease to point G. As mentioned earlier, if the depth scale is re-calibrated at the midpoint of the signal transitions with the reduced sputter yield expected for SiC, the subsequent data points become compressed with respect to depth. Consequently, the gradient change in the Ni signal at point D would become less intense. Indeed, the Ni transition gradient from point D to G could become almost linear if sputter yields could be more accurately calculated. However, the corresponding effect to the Si signal would result in an even sharper rise in the Si profile between points B to C. The net result of these effects points to the presence of residual Ni at the latter half of the interface, providing potential evidence of Ni diffusion over a discrete range through the interface.

The C signal had by far the lowest signal intensity due to its low sputter yield and ionisation efficiency. It has been plotted on a separate y-axis to separate the profile from the Si profile and enable better visualisation of the individual profiles. The 84-16 measurement obtained on the C profile of 53nm is substantially greater than that of the Si and Ni profiles. This indicates that C is present over a greater depth range of the interface than Si or Ni. The C profile itself shows a degree of scatter throughout the interface which may represent a single matrix change or a series of matrix changes occurring, which will affect the sputter yield and concentration of species.

These spurious signals could be assigned to significant fluctuations in the ion current of the LMIG but, fortunately, such fluctuations in the LMIG ion current are, in reality, very small, due to the control electronics maintaining a constant field emission current by automatically adjusting the magnitude of the extraction voltage with high precision. In addition, since each mass spectrum acquisition consists of the integrated counts obtained over 2×10^6 ion pulse cycles, the effects of any systemic fluctuations within the acquisition is largely negligible.

6.3.3 Conclusions of Schottky Ni/SiC depth profile

The obvious presence of a clear interface region within the depth profile of the Ni/SiC Schottky sample proves the profile to be a success in terms of identification of buried structures. The interface appears discrete and abrupt, at least in relation to the thickness of the Ni contact layer. While the interface may be subject to broadening caused by intermixing and chemical changes that are difficult to separate, it does suggest that a reaction may be occurring between the Ni and Si due to the form of the individual profiles through the interface. The scatter in the C signal at the beginning of the interfaces also suggests that fluctuations in the C concentration are present.

6.3.4 Depth profile of Ohmic Ni/SiC sample using two primary ion sources

An Ni/SiC Ohmic sample consisting of a 100nm Ni contact layer on an SiC substrate with a 50nm Ohmic Ni back contact was investigated. The sample was deposited and annealed to 900°C in UHV, as described in chapter 4, section 4.4. A thinner contact was produced for this experiment due to the success of the Schottky profile in Figure 6.3, where a 200nm thick contact layer was shown to be more than thick enough to discriminate the interface. Therefore, it was decided that a thinner Ni contact layer should be sufficient to obtain a suitable depth profile, while reducing the likelihood of depth resolution reduction since the effect of knock-on is cumulative over the thickness of the contact layer. The depth profile used the same primary ion conditions as those on the Schottky sample and is shown in Figure 6.5.

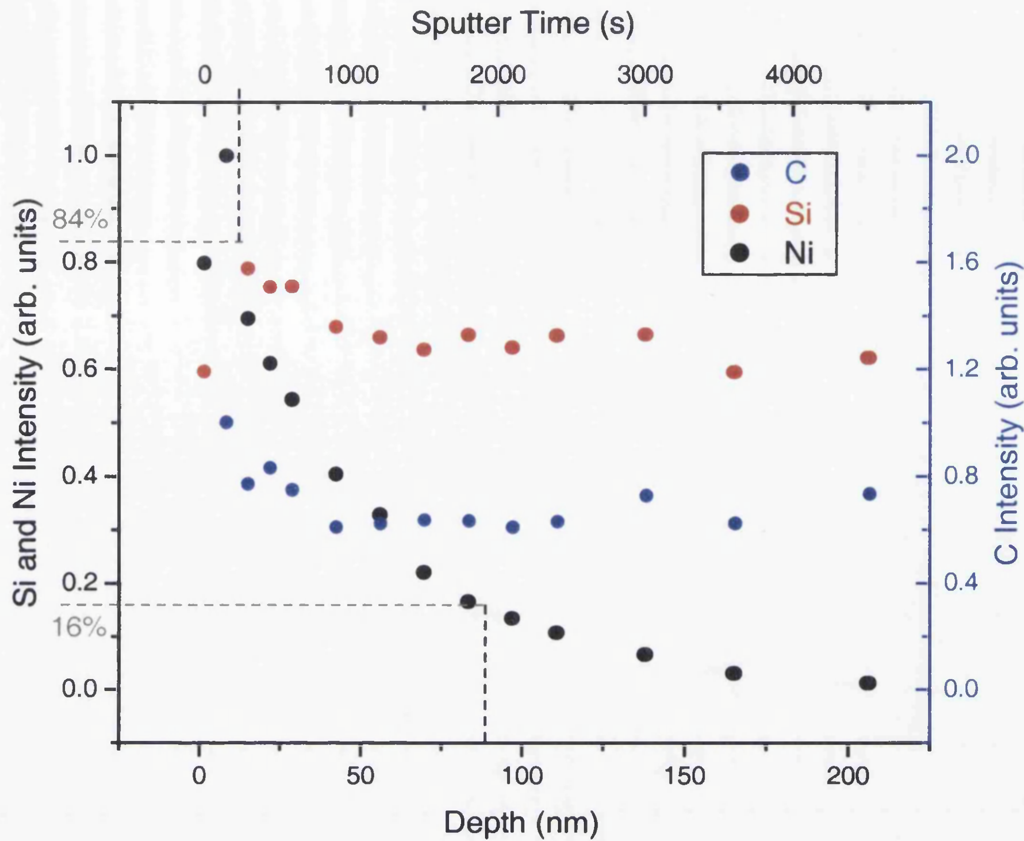

Figure 6.5: TOF-SIMS depth profile of Ni/SiC Ohmic sample annealed to 900°C (4keV Ar^+, 15keV Ga^+)

The presence of the oxide layer is represented in the first two data points of each signal where native oxides and hydrocarbons affect the secondary ion yield and the C signal in particular. The profile itself is clearly different from that of the Schottky sample hence the annealing process appears to have modified the composition and structure of the sample contact and interface. Following the erosion of the oxide layer, it can be seen that all 3 elements under investigation are present in substantial quantity at the beginning of the depth profile. Throughout the profile, Si was the dominant signal in terms of secondary ion yield and there was very little variation in the profile. This was also true of the C signal. Indeed, there was insufficient variation in either signal to obtain an 84-16 measurement indicating likely reactions occurring between the species present. The Ni signal, on the other hand, showed a far more gradual decline in intensity with depth enabling an 84-16 measurement to be roughly taken. The value of 75nm is approximately $2^1/_2$ times greater than the equivalent measurement acquired from the Schottky sample. This suggests that the Ni region of the Ohmic sample extends substantially further than it does in the Schottky sample.

The differences in the C and Si signals as a function of depth support the hypothesis that an extension of the interface and chemical changes as a result of annealing are occurring. Diffusion based reactions could be contributing to this effect, certainly with regard to Si species from the substrate reacting with Ni from the contact layer. However, the C signal may be influenced by surface hydrocarbons, which are inevitably present and are affected by annealing such that they are introduced deeper into the sample. Further analysis of Ohmic samples is discussed in later sections where similar features are observed. Conclusions as to the nature of the Ohmic samples will be developed further in the chapter.

A concern that arose when profiling Ohmic samples using this technique regarded the reproducibility of the depth profiles. Repeat profiles on the Ohmic sample could not reproduce the profile shown in Figure 6.5. Two principal aspects were judged to be the cause of this lack of reproducibility; variation in the duoplasmatron ion beam position with time and oxide layer formation in the time interval when switching between ion sources. In order to use the duoplasmatron ion source, an Ar/O_2 gas mixture was fed into the ion gun assembly to form the plasma at a pressure of approximately $5x10^{-4}$ hPa. The differential pumping system was insufficient to prevent the main chamber pressure from increasing above 10^{-8} hPa, the minimum operating pressure for the LMIG ion source. Therefore, the duoplasmatron ion gun assembly had to be isolated each time a mass spectrum was acquired, a time consuming process over the timescale of a depth profile. Thus, the risk of oxide formation on the sample was always a potential problem that could greatly affect the mass spectrum obtained due to ion yield variation in the presence of an oxide layer. Since the time required to return the main chamber to a pressure suitable for LMIG usage was not constant for each mass spectrum acquisition, the oxide layer thickness was also variable, resulting in similar variability in the mass spectra obtained. This problem was more prevalent in the case of the Ohmic sample where the exact chemical nature is unknown.

The variation in the duoplasmatron ion beam position with time was caused by the fact that the duoplasmatron assembly and ion steering systems were far less sophisticated than those of the LMIG, which was able to maintain a constant primary ion current and ion beam location on the sample. The duoplasmatron ion source had no such monitoring systems causing the beam position to drift over the long term. Since the eroded crater effectively shifted position while the LMIG ion target position was held

constant throughout, mass spectra were acquired from different relative locations within the eroded crater.

6.3.5 Overall assessment of technique of using both ion sources

While the method of using two ion sources to depth profile the samples was successful in demonstrating the existence of differences between the Schottky and Ohmic samples, a number of drawbacks arose that were predominantly technique based, which hindered the reproducibility of the technique. Overall, it was decided that using one ion gun, the LMIG, would significantly improve acquisition times and ensure rigid beam control, as long as depth profiling parameters could be obtained that would minimise intermixing within the sample and mimic the result obtained for the Schottky sample in Figure 6.3 but overcome the fluctuations affecting the Ohmic sample in Figure 6.5.

6.4 TOF-SIMS depth profiles of Ni/SiC samples using LMIG in raster mode

In order to overcome the difficulties encountered when using two separate ion guns for analysis, the LMIG was used for both erosion of a crater and acquisition of mass spectra. A focused Ga^+ ion beam was used to raster a 100µm x 100µm square, flat-bottomed crater.[10] In this way, any non-uniformity in the ion beam profile should be overcome. At set intervals, mass spectra were obtained using the LMIG, again rastered, set to acquire within a 25µm x 25µm square. Both routines used 15keV Ga^+ primary ions with a constant 4kV bias applied to the sample. From Figure 6.2, the average projected ion range of 15keV Ga^+ is 4.9 ± 1.4nm for Ni and 12.0 ± 2.0nm for SiC compared to 2.7 ± 0.8nm and 6.1 ± 1.4nm respectively for 4keV Ar^+ ions. Therefore, additional intermixing in comparison to the duoplasmatron eroded samples is an unfortunate consequence of using the LMIG for both tasks. However, it is expected that this would be offset by improvements resulting from improved uniformity of the eroded crater.

Depth profile of Schottky Ni/SiC sample using LMIG in raster mode

The depth profile of a Ni/SiC Schottky sample is shown in Figure 6.6. The sample structure consisted of an as-deposited 50nm Ni contact layer, SiC substrate and 50nm Ohmic Ni back contact, prepared in UHV as described in chapter 4, section 4.4. The reduced thickness of the contact layer was a result of calibration problems in the deposition system. However, since the profile of the Ni/SiC Schottky sample with a

200nm Ni contact layer profiled using both guns had exhibited a virtual steady-state region prior to the interface (see Figure 6.3), the process of eroding this top layer could be regarded as unnecessarily time consuming and potentially resulting in loss of depth resolution. Therefore, a 50nm Ni contact layer was deemed sufficiently thick enough to obtain steady-state erosion conditions and was also potentially advantageous, in that the increased effect of intermixing associated with the use of 15keV Ga^+ ions may be nullified to an extent by the thinner contact layer.

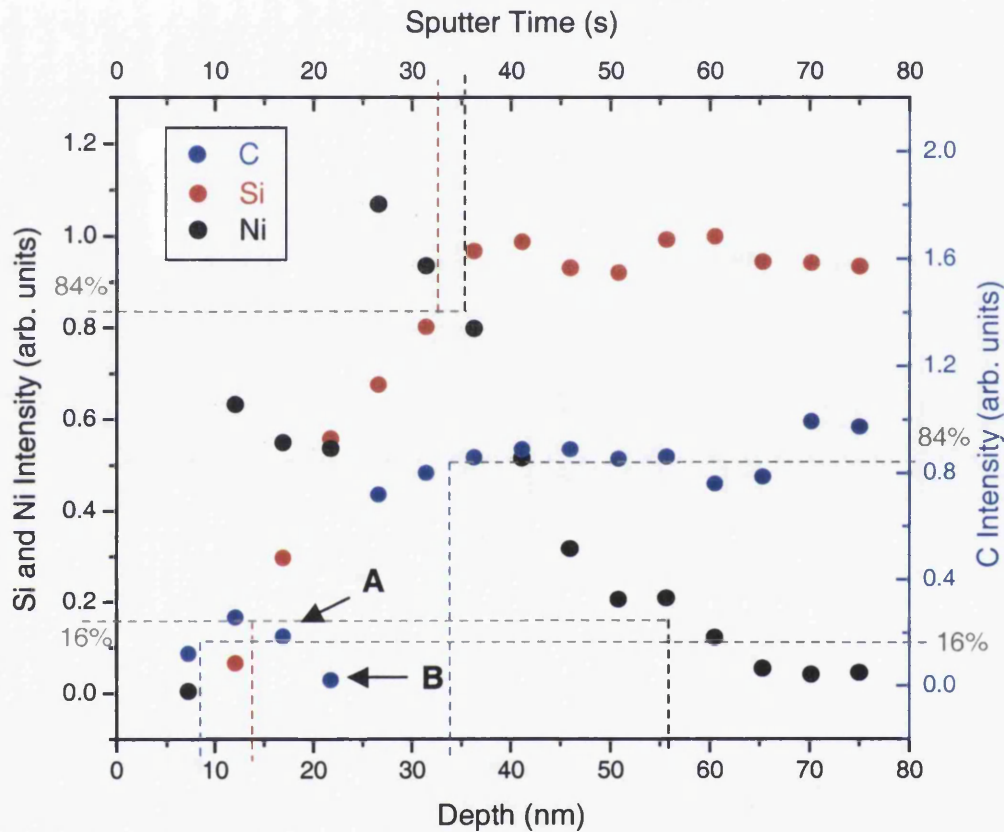

Figure 6.6: TOF-SIMS depth profile of as-deposited Ni/SiC Schottky sample (15keV Ga^+)

From the beginning of the depth profile, an immediate rise in both the C and Si signals is observed followed by a plateau region when the SiC substrate has been reached. This agrees with the profile obtained on another as-deposited sample in Figure 6.3. The C signal profile shows a number of unusual data points at depths indicated by A and B on the profile. The corresponding points within the Ni signal profile are similarly unusual. Since these points are still relatively shallow in the profile, they may be attributed to pre-equilibrium erosion conditions and surface effects. Consequently, a clear Ni rich region corresponding to the contact layer is not obvious from the profile. Nonetheless, a decrease in the Ni signal intensity is visible as the contact layer is eroded, although the Ni still persists at high signal levels when the Si and C signals have reached maximum

intensity. This was not the case in the earlier profile (Figure 6.3) and in this instance it suggests that intermixing has distorted the profile excessively.

The intermixing configuration is caused by the mass difference of the constituents of the two distinct matrices. By using the projected ion ranges of the 15keV Ga^+ ions into Ni and SiC as a guide to kinetics of heavy ion-heavy target and heavy ion-light target collisions respectively, one can predict that knock-on Ni atoms near the interface will project into the SiC substrate. However, these projected atoms will come to rest within a very localised region after the interface as they impart most of their energy in collisions with Si and C atoms in the substrate. This results in substantial Ni concentration within this immediate post-interface region. By analogy with the light ion-heavy target collision scenario similar to that shown in chapter 2, Figure 2.11 (a), recoiling Si and C atoms from the substrate will project into the Ni contact layer with substantial path lengths, although the concentration within the layer will be low due to the spatial variance of the rest positions. Consequently, the depth profile will begin to reveal traces of Si and C once the distance between the bottom of the eroded crater and the interface equals the projected knock-on path length of Ni atoms in a Ni matrix. At this point, knock-on Ni atoms will be capable of reaching the interface to cause a collision cascade within the substrate.

Although the 84-16 measurements for C, Si and Ni of 26nm, 19nm and 20nm respectively suggest that the interface itself is narrower than that of the profile obtained using both ion guns for analysis, the profile itself is far less conclusive that that of Figure 6.3, where a well-defined interface was clearly observable.

Depth profile of Ohmic Ni/SiC sample using LMIG in raster mode

A thicker Ni contact layer was examined for the depth profile of a Ni/SiC Ohmic sample shown in Figure 6.7. The sample, consisting of a 100nm Ni contact layer on an SiC substrate with a 50nm Ohmic Ni back contact, was deposited and annealed to 1000°C in UHV, as described in chapter 4, section 4.4.

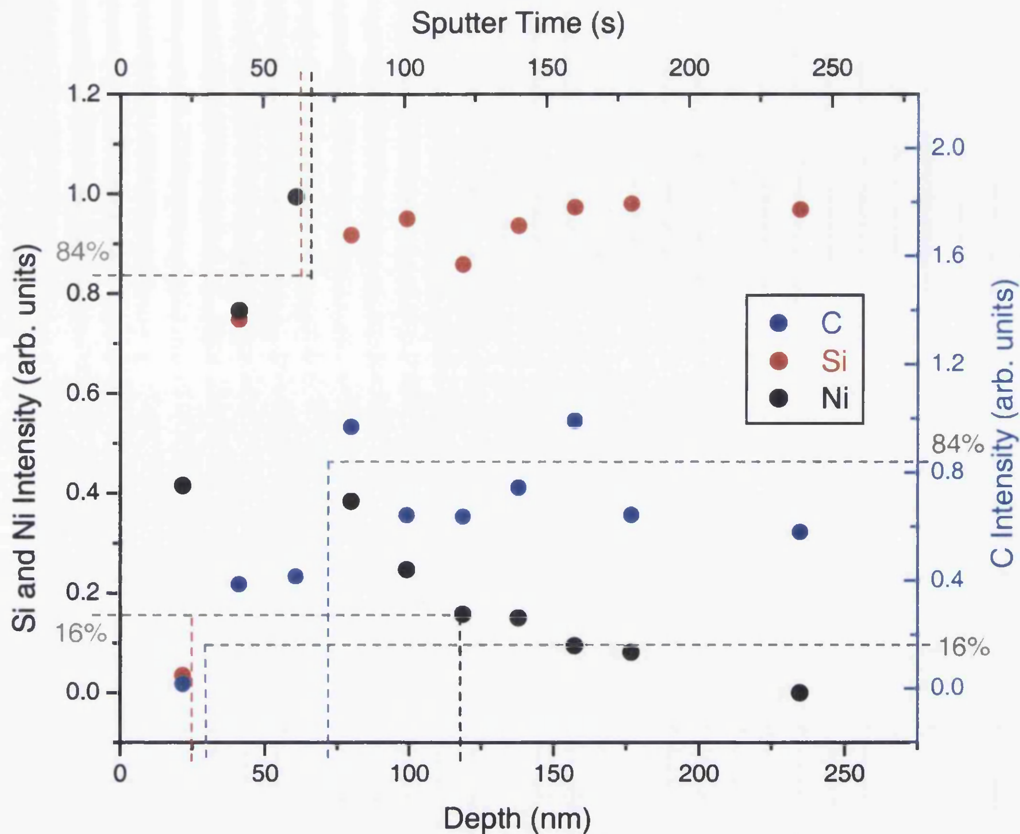

Figure 6.7: TOF-SIMS depth profile of Ni/SiC Ohmic sample annealed to 900°C (15keV Ga^+)

The profile possesses similarities to the Ohmic sample depth profile in Figure 6.5 in that all three signals are present in substantial quantity following erosion of the oxide layer. The Ni signal rises to a maximum then undergoes a similar decline to the earlier profile, while the Si and C signals remain at a high intensity throughout. This also suggests that the contact layer and interface has been modified although there are greater fluctuations in the signals than in the profile that utilised both ion sources. The presence of Si and C in substantial quantities essentially from the beginning of the depth profile (excluding the oxide layer) again confirms the hypothesis that the interface has been extended and that the chemical nature of the contact layer and interface has been altered.

Since the Si and C signal profiles in the earlier profile did not permit an 84-16 measurement to be obtained, it is only relevant to compare the values obtained for Ni. In this instance, a value of 52nm was obtained for Ni compared to 75nm for the earlier profile that used the 4keV Ar^+ source in dynamic mode. This does not agree with the theoretical projections that the 15keV Ga^+ ions should result in increased broadening of features in the profile. However, due to the rather erratic nature of the data points

obtained in Figure 6.7, the error in the 84-16 measurement in this case could be as great as ± 40nm.

The profile also unexpectedly shows similar characteristics to the previous depth profile obtained on a Schottky sample, in that the Ni signal begins to drop as the Si and C reach a maximum level and plateau. It was hypothesised that this was due to the recoil of Si and C into the Ni contact layer in the case of the Schottky sample. This is not necessarily the case in this instance since it is proposed that the Si and C have diffused through the contact layer as a result of the anneal, thus a very different system is present here. Nevertheless, it is clear that there is less distinction between Schottky and Ohmic samples when using this method.

The lack of quality of the depth profiles obtained using the LMIG raster system on both Schottky and Ohmic Ni/SiC samples indicated that this method was flawed. It was decided to investigate if excessive sample roughening was being caused by this procedure that would result in inconsistent secondary ion yields and reduced depth resolution.

6.4.1 Investigation into topographic effects of primary ion beam rastering

Following the acquisition of depth profiles on the samples, the topography of the surface of the Schottky sample and the crater eroded during the profile were investigated using shear force atomic force microscopy (AFM). Topographic images and typical cross-sectional linescans of the surface and crater are shown in Figure 6.8, Figure 6.9 and Figure 6.10.

Figure 6.8 reveals that the surface of the Ni/SiC Schottky sample appears relatively smooth in agreement with TEM studies[1] whereas the post–ablation scans shown in Figure 6.9 and Figure 6.10 show substantial roughening of the crater base. The roughened structure appears to consist of horizontal grooves substantially deeper than the original structure.

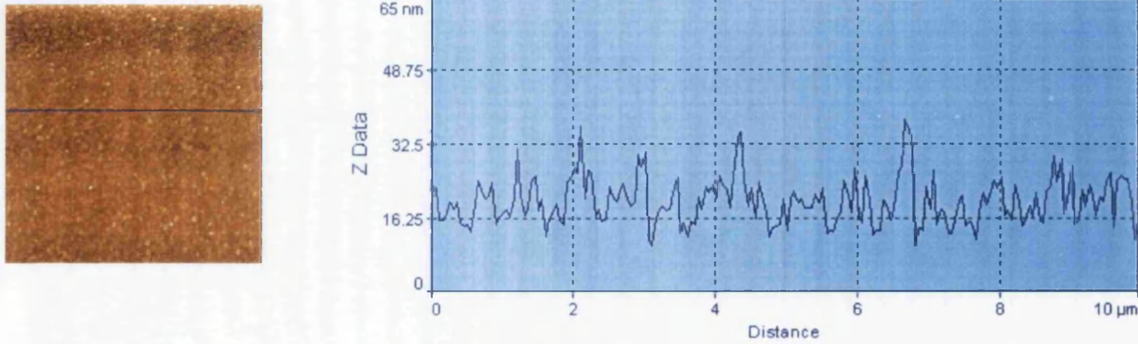

Figure 6.8: 10µm x 10µm topographic scan and typical linescan of Ni/SiC Schottky sample surface.

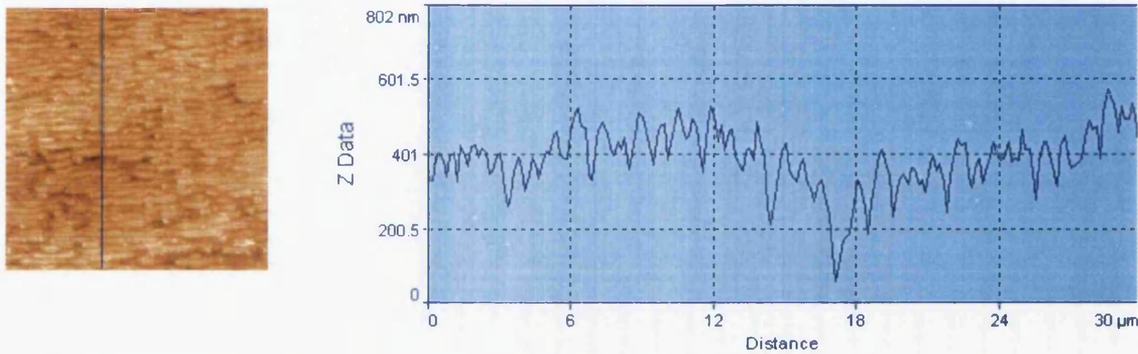

Figure 6.9: 30µm x 30µm topographic scan and typical linescan of crater eroded by focused Ga^{+} ion beam rastered at TV rate on Ni/SiC Schottky sample.

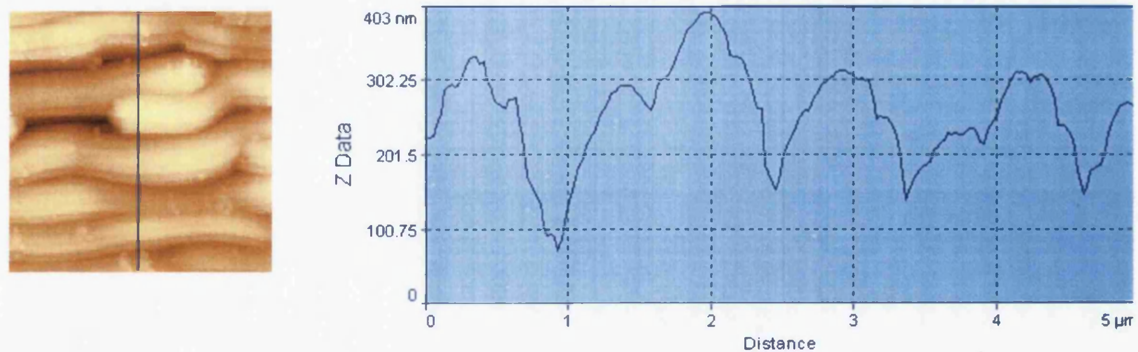

Figure 6.10: 5µm x 5µm topographic scan and typical linescan of crater eroded by focused Ga^{+} ion beam rastered at TV rate on Ni/SiC Schottky sample.

The periodicity of the grooves taken along a line in the y-axis was of the order of 0.8 ± 0.1µm. Since the step-size used for both X and Y translation was ~0.94µm, it can be deduced that the most probable cause of the roughening is the raster rate of the ion beam. The first proposal to counter this roughening involved tightening the raster rate by increasing the X rate with respect to the Y rate. Unfortunately, increasing the X rate naturally increases the acquisition time proportionally. A highly focused ion beam as used in the LMIG would require a very small structure, perhaps up to an order of magnitude larger than the geometry of the ion beam, to be eroded with such a technique.

UNIVERSITY OF WALES SWANSEA LIBRARY

in order to undertake analysis in a feasible timescale. Naturally, this would require that the experimental apparatus is essentially noise-free to eliminate movement of the beam during interaction with the target. Since the TOF-SIMS system used for these experiments was constantly subjected to vibration due to its vacuum pumps and the environment, such high resolution spatial targeting was not feasible. A second proposal to remove the roughening effect was to defocus the ion beam when rastering so that the ion beam diameter is increased to a magnitude greater than the distance between consecutive X cycles. In effect, the beam would overlap each cycle. However, if we consider the inherent Gaussian nature of the ion beam, quantification of fluence delivered at a specific spot, and hence depth eroded, becomes far more complicated.

6.4.2 Overall assessment of technique of using rastered primary ion beam

The technique of rastering a focused ion beam proved to be inadequate in this situation, primarily due to the problem of high magnitude surface roughening caused by the raster beam. "Tightening" the raster rate resulted in excessive acquisition times, while rastering a defocused ion beam introduced uncertainties in the fluence delivered to each area of the sample. To this end, the method used to eliminate the raster-induced roughness was to do away with rastering the beam completely. A defocused ion beam in spot mode would permit "softer" erosion of the sample layers and remove any ambiguity in fluence quantification. Acquisition of mass spectra could be accomplished by using a more focused beam to sample well within the crater. This would reduce the likelihood of probing areas at the edge of the crater containing material at variable depths and diminish the effect of crater bottom unevenness caused by non-uniform current density in the ion beam cross-section when eroding. Consequently, the proposed technique of using a defocused ion beam in spot mode permits simpler deduction of the fluence delivered, a more controlled erosion rate and the ability to sample within a small region of a large crater eroded thus reducing the effect of inhomogeneity inherent to the ion beam. In addition, using the same ion source for both erosion and sampling should enable acquisition of depth profiles in a more convenient timescale. Whilst this method appears rather crude in comparison to the potential of the rastering software, it removes the problem of raster-induced roughening and enables a more direct comparison between Swansea SIMS and Leuven RIMS results.

6.5 TOF-SIMS depth profiles of Ni/SiC samples using LMIG with defocused ion beam

The process of obtaining depth profiles using a defocused Ga^+ ion beam to both erode the sample and acquire mass spectra is far simpler in principle than the previous techniques. However, greater control of the primary ion current and beam position in comparison to the duoplasmatron ion source aids resolution enhancement of the depth profiles.

6.5.1 Depth profile of Schottky Ni/SiC sample using defocused 15keV Ga^+ ion beam

The depth profile of an as-deposited Ni/SiC Schottky sample is shown in Figure 6.11 with the element signals again normalised to the maximum value of each individual element. The sample itself consisted of a 200nm Ni contact layer on an SiC substrate and a 50nm Ohmic Ni back contact. The Ni contact layer was deposited using an Edwards evaporator, described in chapter 4, section 4.4, and is a far more rapid technique than that of UHV deposition. I-V measurements of the sample revealed the same results as the samples deposited in UHV confirming that the electrical characteristics of the sample are unchanged. The Ni contact layer thickness of 200nm was chosen for comparison with Figure 6.3, which had hitherto yielded the most informative Schottky profile.

The LMIG was set to erode a crater of 500µm diameter using 15keV Ga^+ ions by setting the LMIG to spot mode and reducing the voltage applied to the second condenser lens to 9kV. To acquire mass spectra, the voltage of the condenser lens was increased to produce a primary ion beam spot of 200µm in diameter on the sample surface. This ensured that the area probed was located close to the crater centre, reducing the probability of sampling regions on the perimeter of the crater and thus negating contributions of species at the edge of the crater. These conditions were chosen such that static SIMS conditions were maintained during mass spectrum acquisition.

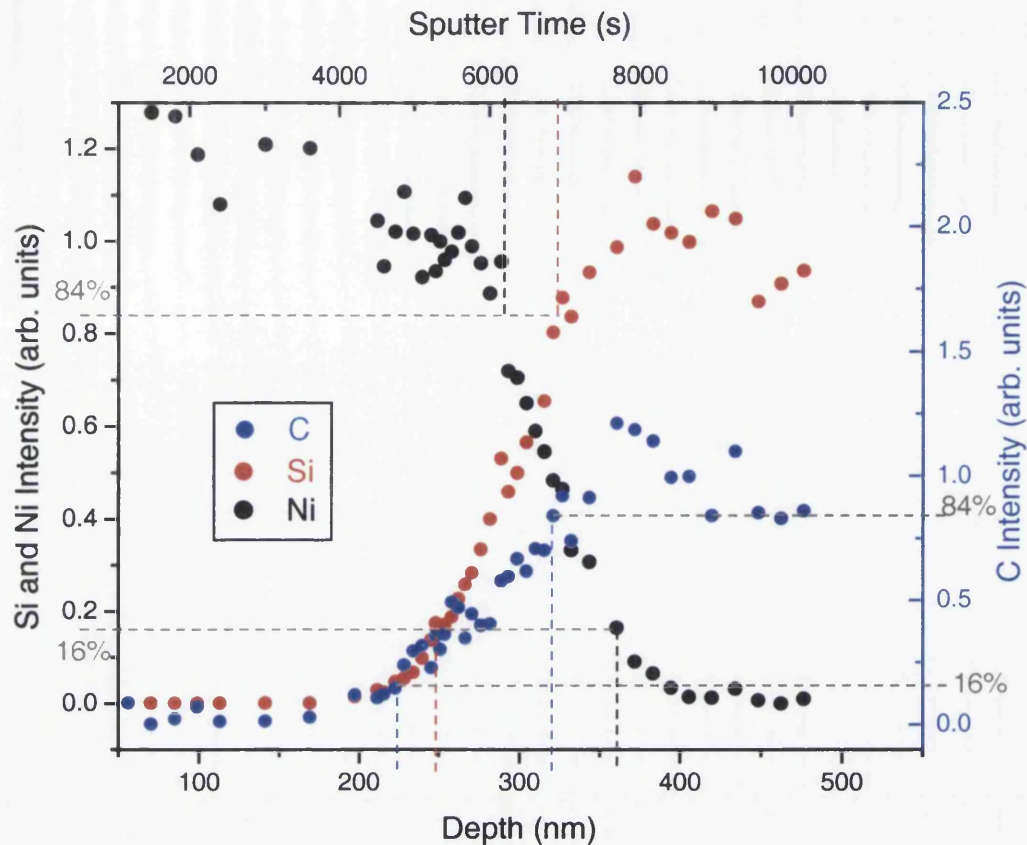

Figure 6.11: TOF-SIMS depth profile of as-deposited Ni/SiC Schottky sample using a defocused 15keV Ga^+ ion beam for erosion and acquisition.

The depth profile obtained very closely resembles that of Figure 6.3, which was acquired using both ion sources. Once again, there is a very obvious transition from the Ni contact layer to the SiC substrate, while the 84-16 measurements for Ni and Si are also very similar to each other with that of C significantly greater in magnitude. The values obtained for the 84-16 measurements in both the earlier profile using both ion sources and this profile using a single defocused Ga^+ ion source are shown in Table 6.1.

The effect of increased interfacial width caused by intermixing when using 15keV Ga^+ ions instead of 4keV Ar^+ ions can be seen in these values, where all values obtained using Ga^+ are between 1.8 and 2.6 times higher than those using Ar^+.

	Schottky sample profiled using both 4keV Ar^+ ion beam (Figure 6.4)	Schottky sample profiled using 15keV Ga^+ ion beam (Figure 6.11)	Ratio of Ga^+ induced values to Ar^+ induced values
Carbon (84%-16% ratio change)	53nm	96nm	1.81
Silicon (84%-16% ratio change)	30nm	76nm	2.53
Nickel (84%-16% ratio change)	28nm	73nm	2.61

Table 6.1: Comparison of 84-16 measurements of component elements of Ni/SiC Schottky sample from depth profiles obtained using different erosion/acquisition methods

Despite the additional broadening of the interface caused by the Ga^+ ions, many features of the depth profile are consistent with the earlier profile that used both ion sources. Once again, the Si signal profile is relatively smooth, whereas the C and Ni signal profiles show a degree of scatter at the start of the interface. The fact that such fluctuations are not present in the Si signal suggests that this phenomenon may not merely be a result of new equilibrium bombardment conditions being set-up in a new matrix, but rather a possible indication of dissociation of SiC and variable concentration Ni regions. However, dissociation of SiC only occurs due to the strong reactivity of Ni beyond 400°C [3]. Thus, the fluctuations are more likely to be a result of a matrix change induced by the ion bombardment. The C fluctuations may also be attributed to residual hydrocarbons present on the SiC substrate prior to deposition since the samples were not produced in UHV.

Following the variable region at the start of the interface, the Ni signal proceeds smoothly through the interface and tails off as the SiC substrate is reached, while the C signal continues to show a similar level of scatter throughout. Again, this is in agreement with the earlier profile thus validating the viability of this new technique of acquiring depth profiles and the method of depositing Ni on SiC. However, the variations in the gradient of the Ni and Si signal during the crossover period of the Ar^+ depth profile do not appear to be present in this profile. The likelihood is that this is a result of the level of intermixing induced by the 15keV ion beam.

Another interesting feature involves the point at which the Ni signal profile begins to fall with respect to the point at which the C and Si signal profiles begin to rise. In theory, these points should occur at effectively the same depth. However, the profile shows a rise in the C and Si signals between 170nm and 200nm, whereas the fall in the Ni signal begins at between 250nm and 270nm, a significant depth further into the sample. This effect may be due to C and Si diffusion into the Ni contact layer or Ni projection into the SiC substrate and will be discussed in comparison to equivalent depth profiles later in the chapter.

6.5.2 Depth profile of Ohmic Ni/SiC sample using defocused 15keV Ga^+ ion beam

With the success of the technique to produce a comparable depth profile to that obtained using both ion sources, an Ohmic sample was depth profiled to achieve a similarly informative result. The sample produced had a 200nm Ni contact layer deposited in the Edwards evaporator on a SiC substrate with a 50nm Ohmic Ni back contact. The sample was then annealed in vacuum to 1000°C to produce an Ohmic contact. A 200nm Ni contact layer was chosen, as the depth profiles of thinner coverage samples suggested a reaction occurring over the whole range of the Ni contact layer. A thicker layer was deposited to permit steady state profiling conditions to be reached before probing the interface region. Identical bombardment parameters to those of the Schottky sample were used to achieve the depth profile shown in Figure 6.12.

The profile obtained appeared strikingly different compared to that of the Schottky sample. The profiles of the carbon and nickel signals in particular appeared extremely erratic although an apparent cross-over was present, beyond marker point C, where the nickel signal drops as the silicon and carbon signals rise. This apparent interface was not particularly evident in earlier profiles on Ohmic samples, while the sputter time required to reach the interface suggests that the earlier profiles did not actually traverse the interface itself. In fact, the earlier profiles may have terminated just shy of the start of the interface. From the time required to reach the interface on this Ohmic sample, it is quite clear that the pre-interface region is comprised of a very different matrix, or matrices, than the Schottky sample. Indeed, since the sputter time required to reach the interface is approximately triple the value of an equivalent Schottky sample, it can be deduced that the average sputter yield of the matrix, or matrices, being eroded is approximately a third of that of nickel.

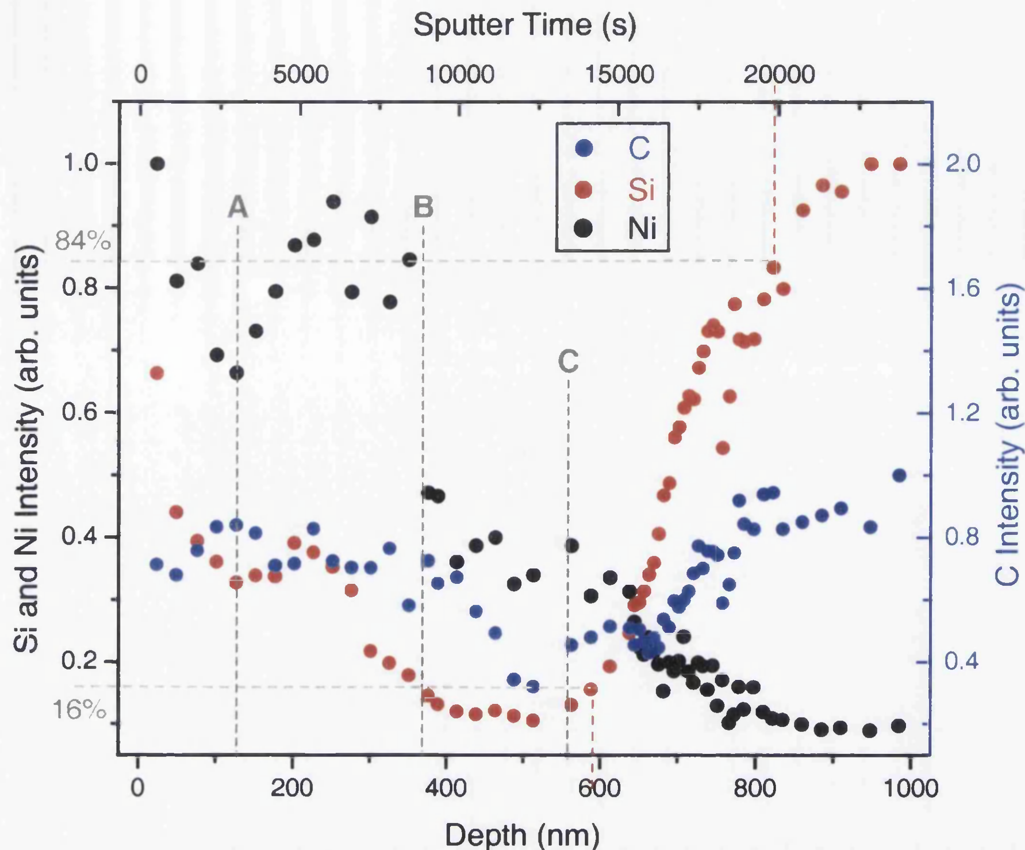

Figure 6.12: TOF-SIMS depth profile of Ni/SiC Ohmic sample annealed to 1000°C using a defocused 15keV Ga^+ ion beam for erosion and acquisition. A, B and C are marker points of interest.

Using the formula derived by Yamamura et al [7], the sputter yield values for 15keV Ga^+ ions striking Ni, Si and C are shown in Table 6.2.

	Nickel	Silicon	Carbon
15keV Ga^+ primary ion	5.566	2.076	1.542

Table 6.2: Sputter yields (sputtered atoms/primary ion) calculated for nickel, silicon and carbon bombarded with 15keV Ga^+ primary ions using Yamamura formula [7] (Equation 2.9).

Since all three elements are present in appreciable abundance throughout the profile, it suggests that a new matrix, or matrices, comprising these elements has been formed. In addition, the magnitude of the signals over the region A-B, point to the presence of a matrix for which the C, Si and Ni have relatively high ionisation efficiency. This

contrasts with the region B-C, where all three signals attain their lowest yield in the contact layer. Indeed, aside from Ni, which naturally drops to an even lower level as the interface is eroded, both Si and C experience their lowest signal levels within this region B-C. This is indicative of a matrix change before the interface is reached. Hence a substantial reaction resulting in diffusion of Si and C to the limits of the contact layer has occurred as a result of the annealing process and potentially two different matrices are known to be present.

Other work using TEM [1,2] has shown that an anneal at 950°C results in a high content of Si in the contact layer in the form of Ni-silicide due to the dissociation of SiC. EDS X-ray analysis and Auger depth profiling of the contact layer[1,2] has revealed the presence of C along with substantial C segregation to the top region of the contact. The diffusion of these elements results in the existence of voids inside the contact layer. The TOF-SIMS depth profile confirms the diffusion of Si and C into the contact layer, and shows that the altered contact layer composition may not consist of a single matrix.

6.5.3 Evaluation of technique of using defocused Ga^+ ion beam

The use of a defocused Ga^+ ion beam has proved capable of obtaining characteristic depth profiles of both Schottky and Ohmic samples. While the resolution of the Schottky sample depth profile does not quite match that of the equivalent profile obtained using both ion sources, many comparable features are present. This is most encouraging considering the magnitude of the primary ion energy. The depth profile of the Ohmic Ni/SiC sample is remarkably different to that of the Schottky sample consisting of many signal variations that indicate a markedly different composition due to a reaction between the Ni and SiC. However, the increased intermixing level does inhibit a more accurate appraisal of the interface.

Therefore, the natural progression was to attempt to obtain further depth profiles using reduced primary ion energy. Subsequent tests succeeded in reducing the energy of the Ga^+ ions to 7keV with a 4kV sample bias present while still allowing sufficient secondary ions to be detected. Further reduction resulted in excessive beam drift, such that insufficient ion current on the sample was available.

6.5.4 Depth profile of Schottky Ni/SiC sample using defocused 7keV Ga^+ ion beam

The next depth profile was obtained from an as-deposited Ni/SiC Schottky sample, consisting of a 200nm Ni contact layer deposited in the Edwards system. To maintain similar bombardment dimensions as the 15keV profile, the second condenser lens was set to 4.1kV to erode a 500μm for erosion and was increased in magnitude to sample a 200μm spot. The profile obtained using 7keV Ga^+ primary ions is shown in Figure 6.13 and shows many of the features observed in the 4keV Ar^+ and 15keV Ga^+ depth profiles. Indeed, it more closely resembles the 4keV Ar^+ profile in Figure 6.3 than the profile obtained at 15keV in Figure 6.11.

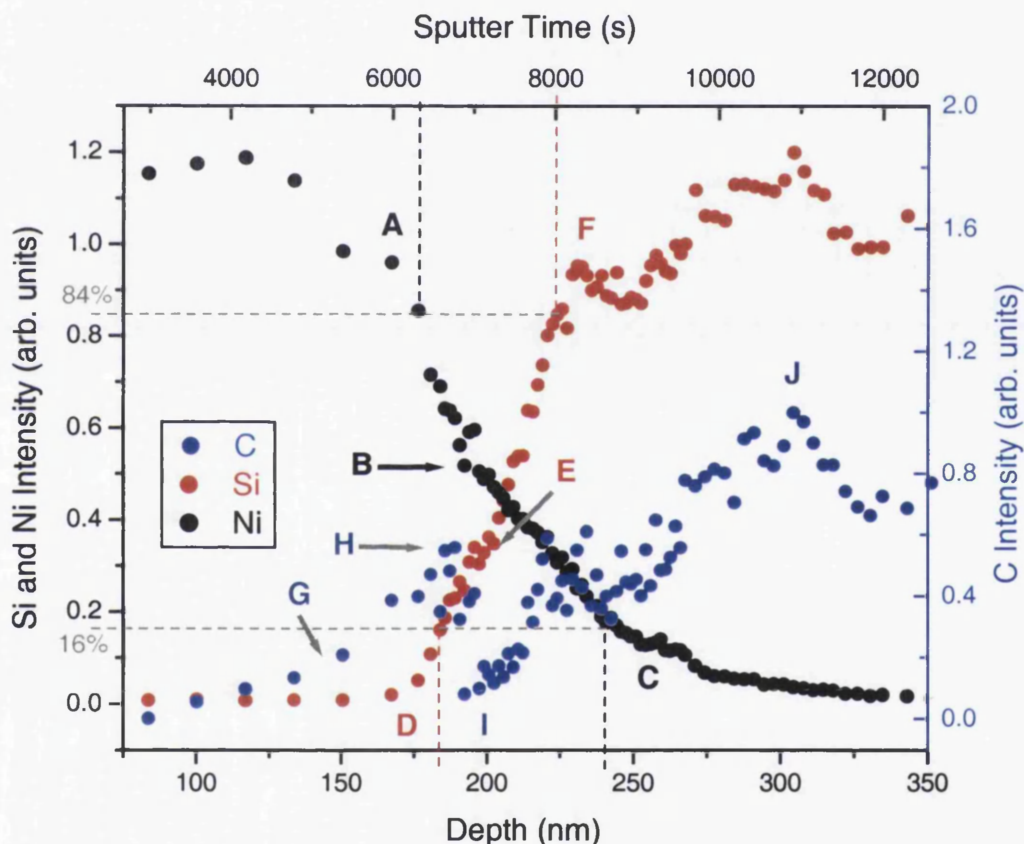

Figure 6.13: TOF-SIMS depth profile of as-deposited Ni/SiC Schottky sample using a defocused 7keV Ga^+ ion beam for erosion and acquisition. Points A-J represent marker points of interest.

The Ni signal shows an intensity decrease consisting of fairly linear sections of variable gradient from point A to B then from B to C, as occurred in the Ar^+ profile. Similarly, the Si signal can be seen to increase from D to E then more rapidly from E to F, although the change in gradient is less striking than that of the Ar^+ profile. A change of matrix is the most likely cause of these variations in the Ni and Si signals since they occur at virtually the same point. Consequently, the sputter yield will vary and since the

location of interest occurs closer to the SiC substrate, the sputter yield can be assumed to be lower. Hence, the sputter depth stated at this point and beyond will be exaggerated. Without exact knowledge of every matrix present in the sample, their size and position, exact conversion to depth is not possible. However, if the sputter yield is indeed lower than that of Ni beyond the point of these gradient changes, the Ni signal profile through the interface could become almost linear over most of the transition B-C. The Si signal profile would experience an even more pronounced gradient increase at the point in question. From this, it can be predicted that a small degree of Si diffusion across the interface may be occurring although recoil implantation may also be a cause of the flatter Si profile at the beginning of the interface.

The scatter in the C signal observed in both the 4keV Ar^+ and 15keV Ga^+ profiles is far more pronounced in this profile. The signal undergoes a rise from point G to H as expected, which precedes a sudden, substantial and unexpected decrease from point H to I, followed by a second rise in the signal from point I to J. The second rise incorporates a region of extensive scatter, consisting of a small plateau in the signal at an apparent depth of ~ 230nm that coincides with a near plateau in the Si signal.

The scatter within the C signal through the interface may be attributed first and foremost to the decreased signal-to-noise level caused by the greatly inferior sputter ion yield of C compared to Si, Ni and indeed most elements. Nevertheless, the profile does suggest extreme changes in the concentration of C through the interface, matrix effects notwithstanding. If the as-deposited samples truly have no reactions occurring at the interface, two distinct matrices will exist and the ideal profile should exhibit abruptly sharp changes of concentrations in the signals at this point. Intermixing caused by the ion beam will inherently broaden this region causing variable composition matrices to be created. However, the "see-sawing" nature of the C signal through the interface is not present in the Si and Ni signals, suggesting an additional process is occurring. As mentioned in the analysis of the Schottky depth profile obtained using 15keV Ga^+ ions, the presence of residual hydrocarbons on the SiC substrate, or hydrocarbons introduced as a result of the Edwards preparation process, may manifest itself in this manner in the profile.

It was only practical to obtain an 84-16 measurement off the Ni and Si signals, due to the substantial variability of the C signal resulting in two points corresponding to 16%

intensity. The 84-16 values obtained were 40nm and 63nm for Si and Ni respectively. The Si value is close to half that obtained in the 15keV Ga^+ profile whereas the Ni value is approximately 86% of its equivalent value. Therefore, the decreased energy results in the reduction of intermixing as expected, although the Ni crossover width remains quite broad. This is primarily due to the flattening of the Ni signal profile described between points B and C. As with the 4keV Ar^+ depth profile, these gradient changes in the transition regions of the Ni and Si suggest that a residual presence of Ni occurs at the latter half of the interface. Since the primary ion energy has been reduced substantially (compared to Figure 6.11), the knock-on effect of Ni projection will be similarly reduced, confirming that the extended presence of Ni in the interface is a real effect.

Another interesting fact regards the locations of the fall of the Ni signal profile and the rise of the C and Si signals at the start of the interface. In Figure 6.11, representing a depth profile using 15keV Ga^+ ions, the Ni signal began to fall between 50-100nm later than the corresponding Si signal rise. The magnitude of the uncertainty is due to the fluctuations that occur in the Ni signal in this region. In the case of the 4keV Ar^+ depth profile on a Schottky sample (see Figure 6.3 & Figure 6.4), this "delay" was reduced to approximately 10-30nm. The latest profile using 7keV Ga^+ primary ions has practically no "delay", i.e. the beginning of the rise of the Si signal and that of the fall of the Ni signal occur almost simultaneously. Interestingly, SIMS studies on Ni/3C-SiC Schottky samples performed by Roy et al[11] used a 10keV Cs^+ primary ion source to obtain depth profiles, which showed a significant "delay" between the start of the fall of the Ni signal and the start of the rise of the Si and C signals. Indeed, the magnitude of this "delay" is comparable to the 15keV Ga^+ depth profile in Figure 6.11.

To this end, SRIM calculations were performed to determine the effect of Ni implantation with differing primary ion sources. In all models, elastic collisions between the primary ion and the target Ni atom have been assumed along with no angular variation between the initial trajectory of the primary ion and the final trajectory of the target atom after collision. By conservation of momentum and energy, the velocity and hence kinetic energy of the Ni atom after collision were deduced. This energy was inputted as the primary projectile energy in the SRIM program and its trajectory into the SiC substrate was then simulated.

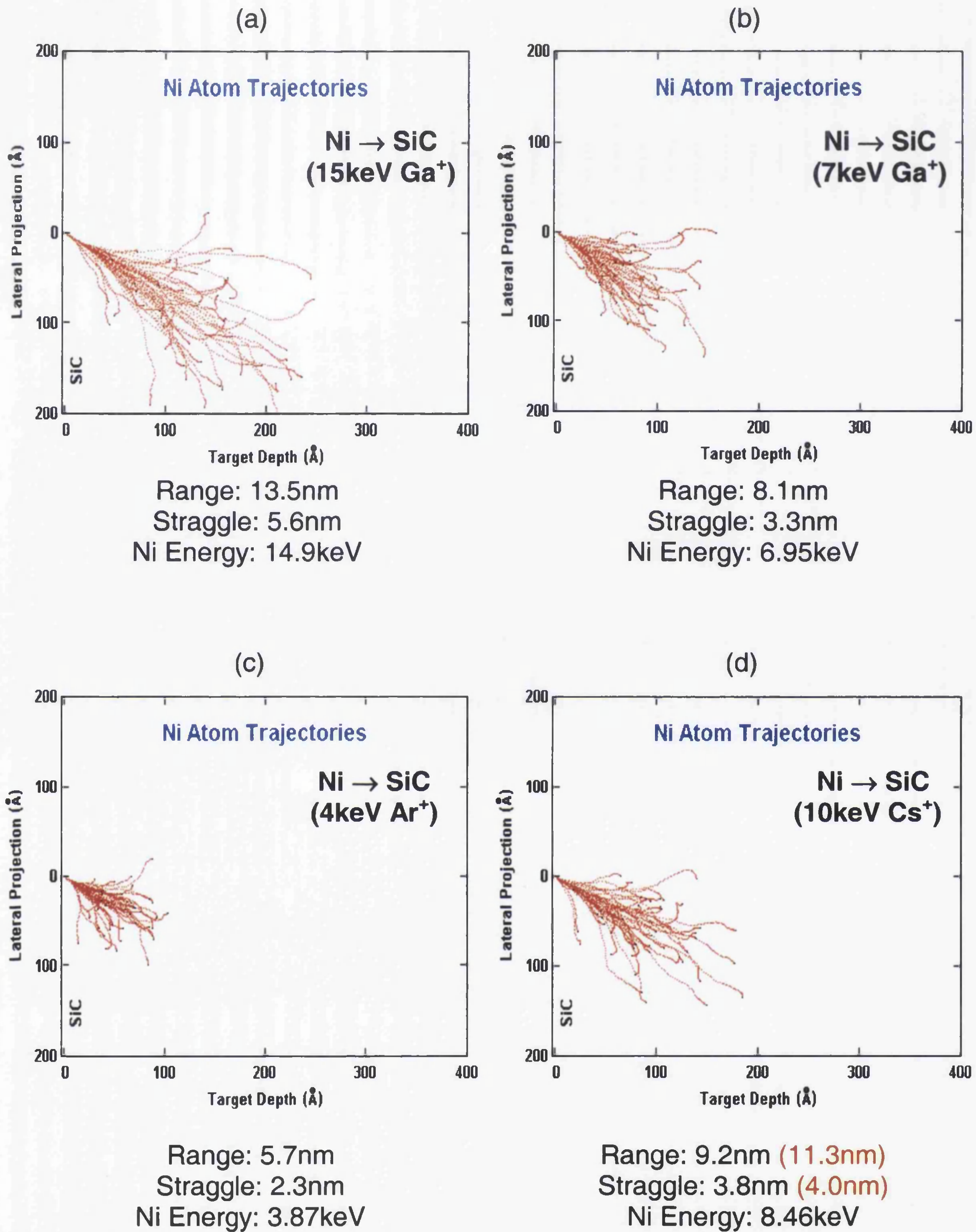

Figure 6.14: SRIM simulations of Ni implantation into SiC at 35° following collision with (a) 15keV Ga^+, (b) 7keV Ga^+, (c) 4keV Ar^+, and (d) 10keV Cs^+ primary ions. (Values states in red denote Ni implantation at normal incidence)

Figure 6.14 shows the results of 50 initial Ni atoms projected into the SiC substrate following collisions with (a) 15keV Ga^+, (b) 7keV Ga^+, (c) 4keV Ar^+, and (d) 10keV Cs^+ primary ions. In all cases, the initial angle has been set at 35°. The studies performed by Roy et al [11] do not specify the angle to which the primary ions intercept

the target. Therefore, the simulations assume a value of 35° for comparison purposes, although the range values for normal incidence are also stated. The range values themselves represent 5000 incident particles, whereas the images plot just 50 in the interest of clarity.

The use of 15keV Ga^+ primary ions can be seen to cause the greatest knock-on implantation of Ni atoms compared to the others. Indeed, its implantation depth is almost 50% greater than that of the next highest, 10keV Cs^+(at 35°). While the values stated for the projected range do not match the magnitude of the "delay" observed between the start of the Ni fall and Si rise in the profiles, it must be noted that these simulations assume all incident atoms originate at the sample surface (0A). As the sample is eroded, implanted atoms may become further implanted as the primary ions reach the initial implantation depth (a multiple knock-on effect). Consequently, it is only in the relative values that comparison should be made.

6.5.5 Depth profile of Ohmic Ni/SiC sample using defocused 7keV Ga^+ ion beam

A depth profile, shown in Figure 6.15, of an Ohmic Ni/SiC sample with a 200nm Ni contact layer deposited on the SiC substrate was then performed using the 7keV Ga^+ primary ion beam parameters employed for the Schottky depth profile in Figure 6.13. The sample was identical in preparation to that used for the 15keV depth profile shown in Figure 6.12.

The first notable feature of the profile is the distinct rise in all three signals to a maximum at an "apparent" depth of 200nm followed by an almost symmetrical fall in all signals. A similar feature was observed when probing with 15keV Ga^+ ions, although the profile using lower energy ions appears to portray this effect with greater clarity. The aspect of the rise appears similar to that observed when probing an oxide layer formed on the surface of a sample, although the erosion time required for the signals to reach their maximum is not consistent with the typical thickness of an oxide layer. However, it may be postulated that the action of annealing may induce diffusion of the oxide layer deeper into the sample, which would broaden the apparent thickness of an oxide layer. The magnitude of the signal intensities over this region certainly suggests a substantial increase in the secondary ion efficiency consistent with oxygen enhancement. It is clear that a distinct matrix change is occurring between an apparent depth of 200nm and 400nm due to the relative signals of C, Si and Ni.

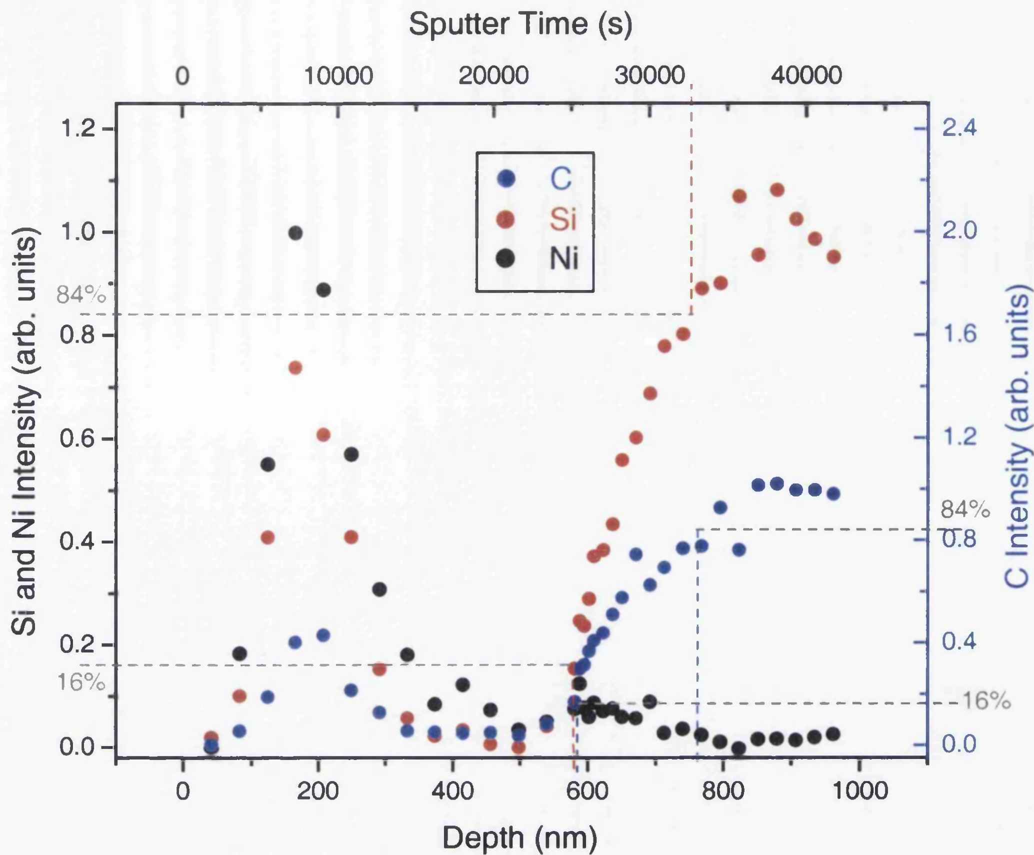

Figure 6.15: TOF-SIMS depth profile of Ni/SiC Ohmic sample annealed to 1000°C using a defocused 7keV Ga^{+} ion beam for erosion and acquisition.

Following this distinct rise and fall in the signals, the profiles stabilise to a large extent at a low intensity level, although a degree of fluctuation is still present. Within this region between 400nm and 550nm, a constant presence of carbon can be observed, whereas the Ni and Si signals proceed to decrease prior to the interface. This may indicate an accumulation of carbon at the deeper region of the contact layer. The presence of carbon in annealed Ohmic Ni/SiC samples has been observed throughout the contact layer by EDS X-ray analysis, Auger depth profiling and XPS[1,2,3,12]. XPS measurements on Ohmic Ni contacts to the C-face and Si-face of 6H-SiC[13] have shown that the interface on the C-face is more enriched with carbon.

The presence of Si and C throughout the contact layer provides evidence that the contact layer matrix is substantially different from that of the Schottky samples. Indeed, the existence of Si and C within the contact layer indicates that the process of annealing has caused diffusion of these elements into the layer itself.

Between an apparent depth of 500nm and 600nm, the start of a clear interface can be observed, which extends to approximately 800nm sample depth, following which the SiC substrate is probed. An 84-16 measurement on the Ni signal profile was not deemed practical due to the effect of the different matrix at the start of the profile. However, a value of 180nm was obtained from both C and Si. In comparison to the value of 40nm obtained from the 7keV Ga^+ profile on an as-deposited sample, the interface of the Ohmic sample appears substantially broader than that of the as-deposited sample. This suggests that in addition to Si and C diffusion into the contact layer, Ni has similarly diffused into the SiC substrate although to a lesser extent as can be observed from the interfacial width.

As with the 15keV Ga^+ depth profile on an Ohmic Ni/SiC sample, the apparent depth at which the interface occurs is approximately three times that expected. This suggests that either the interface has been shifted deeper into the sample and hence the thickness of the contact layer has increased or the matrix properties inhibit the sputter yield causing the apparent depth to be overestimated. Whilst the projection of Ni into the SiC substrate could translate the apparent location of the interface further into the sample, such an effect would occur to a similar degree in the as-deposited sample and as such can be ignored. The presence of Si and C throughout the contact layer appears to reduce the sputter yield of the new matrix, or matrices, formed as described in the 15keV profile analysis, thus the sputtered depth stated represents an overestimation. It can be reasoned that the majority of the increase in the apparent thickness of the contact layer from the depth profiles may be attributed to the inferior sputtering characteristics of this altered contact layer. Nevertheless, even taking into account the reduced sputter yield, it is still quite possible that the interface is located deeper than in the as-deposited Ni/SiC samples, hence the contact layer is increased in thickness by a corresponding amount.

TEM research by other groups [1,2,3] has determined that the contact layer of Ni/SiC samples annealed in excess of 900°C is indeed substantially thicker than that of as-deposited samples in agreement with the findings of these depth profiles. In addition, Marinova et al [3] also determined that the interface is shifted into the SiC region. This too is in agreement with findings of this depth profile.

The research described above also suggested that the annealing action causes the SiC to dissociate at the interface as a consequence of the strong reactivity of Ni above 400°C. This results in the formation of mixed phase Ni-silicides with Ni_2Si found to be the principal phase [1,2,3,12] although Rastegeava et al [13] agreed that while Ni_2Si was the only phase of any magnitude that occurred when the annealed sample consisted of Ni deposited on the Si-face of 6H-SiC, equivalent deposition on the C-face resulted in the formation of appreciable Ni_3Si_2 in addition to Ni_2Si. In both cases, the action of annealing these samples beyond 900°C results in the dissociation of the SiC, causing interaction between the Si and the Ni of the contact layer producing an altered contact layer consisting of Ni-silicide and C. The Ni within the contact layer is consumed by this reaction to form Ni-silicide such that equilibrium conditions between the contact layer and the substrate exist.

The chemical changes that occur within the sample have also been seen to give rise to a number of Kirkendall voids throughout the contact layer but primarily at the location of the original interface [1,2,3,12,13]. Hi-resolution electron microscopy has shown that the internal surface of the voids is covered by some of the excess carbon.[1,2] By allowing for the lower sputter yield of the new contact layer, it can be estimated that the location of the initial interface on these Ni/SiC samples may have occurred at an apparent depth of approximately 400-500nm, approximately where the carbon accumulation prior to the interface described earlier was seen to arise. Therefore, it can be assumed that this corresponds to the location of the large number of voids indicated by other techniques.

6.6 Conclusion of TOF-SIMS depth profiles on Ni/SiC samples

This section has dealt with obtaining the most accurate depth profiles possible and has examined the strengths and weaknesses of various methods of acquiring the profiles. As per theory of depth profiling, the technique of using a high mass, low energy primary ion gave the most promising results while the standard technique of primary ion rastering is only effective if the line-by-line distance is significantly less than the spatial geometry of the ion beam itself. Experimentally, this proved highly difficult to realise during depth profiling of these samples.

The strikingly different depth profiles obtained when probing the Schottky and Ohmic samples indicate that the process of annealing substantially alters the structure of the initial as-deposited sample. The Schottky samples exhibit a very clear region of Ni

dominance coupled with negligible presence of Si and C, representing the contact layer deposited. A discrete interface is then observed whereby the Ni intensity falls off with a corresponding increase in the Si and C signals through to the SiC substrate. The depth profiles obtained using the LMIG at 15keV, in defocused mode, show that the Si and C signals begin to rise before the Ni signal starts to fall. The effect of knock-on implantation was simulated using SRIM for various primary ion types. The "delay" between the rise of the Si signal and the fall of the Ni signal at the interface was found to be a direct result of Ni implantation, the magnitude of which is proportional to the energy imparted to the Ni target atom. The depth profile obtained on a Schottky sample using 7keV Ga^+ primary ions showed virtually no "delay" indicating that Ni implantation had been reduced to acceptable levels.

Despite the broadening of the interface of the Schottky samples caused by ion intermixing, the presence of a reaction occurring between the Ni and SiC can be inferred. The magnitude of the rate of rise of the Si signal through the interface is greater than the equivalent rate of fall of the Ni signal. While this may be due to the aforementioned knock-on implantation of Ni, a degree of Ni-silicide bonding present at the latter half of the interface cannot be ruled out. The variable behaviour of the C signal also suggests an extremely changeable concentration through the interface. Whether this C variation is caused by the matrix effect, residual hydrocarbons on the SiC surface or reactions at the interface cannot be discerned at this point. However, a chemically abrupt interface would consist of two distinct matrices, hence the existence of such fluctuations in the C signal points to the presence of multiple matrices.

The profiles of the Ohmic samples are significantly more complicated than those of the Schottky samples. There are several indications that suggest a reaction has occurred between the Ni and SiC, most notably the constant presence of Si and C throughout the profiles. This suggests diffusion of Si and C beyond the interface and fully into the Ni contact layer. The apparent increased width of the interface width when compared to the corresponding as-deposited sample infers that a degree of Ni diffusion into the SiC substrate has occurred. This agrees with the theory that when these samples are annealed to high temperature, SiC becomes dissociated due to the reactivity of Ni above 400°C. The dissociation continues until complete consumption of the Ni contact layer occurs [3] resulting in the formation of a Ni-silicide (mainly Ni_2Si) contact layer along with C accumulations.

The apparent depth of the interface on the annealed Ni/SiC samples also suggests that the interface exists deeper in the sample than it does in the as-deposited samples and hence the contact layer is increased in thickness after allowing for the overestimation in depth calculated as a result of the reduced sputter yield of the altered contact layer. The increase in the contact layer thickness and the translation of the interface deeper into the sample are due to the reactions occurring throughout the interface and contact layer whereby Si from the substrate continues to react with Ni to form these Ni-silicides until an equilibrium between the contact layer and substrate is reached.

The experiments undertaken indicate that the ideal progression for this analysis would be to reduce the ion beam energy further to low keV, or possibly sub-keV regimes as described recently by several authors[5,6] to further reduce the level of ion beam induced uncertainties in the profile. Since the final profiles represent the limit of the current system, such an analysis would require a system upgrade. However, the potential of TOF-RIMS to perform analysis of bonding mechanisms provides an alternative method of overcoming SIMS constraints as described in the following chapter. By using the same primary ion parameters for RIMS profiling, comparison can then be made between the SIMS and RIMS depth profiles.

6.7 References

[1] B. Pécz, Appl. Surf. Sci. **184,** 287 (2001).

[2] B. Pécz, G. Radnoczi, S. Cassette, C. Brylinski, C. Arnodo, O. Noblanc, Diamond and Related Materials **6,** 1428 (1997).

[3] Ts. Marinova, A. Kakanakova-Georgieva, V. Krastev, R. Kakanakov, M. Neshev, L. Kassamakova, O. Noblanc, C. Arnodo, S. Cassette, C. Brylinski, B. Pécz, G. Radnoczi, Gy. Vincze, Materials Science and Engineering **B46,** 223 (1997).

[4] J.F. Ziegler, J.P. Biersack The Stopping and Range of Ions in Matter Version SRIM-2003.2.0.

[5] T.J. Ormsby, D.P. Chu, M.G. Dowsett, G.A. Cooke, S.B. Patel, Appl. Surf. Sci. **144-145,** 292 (1999).

[6] M.G. Dowsett, Appl. Surf. Sci. **203-204,** 5 (2003).

[7] Y. Yamamura, H. Tarawa, Atomic Data and Nuclear Data Tables **62,** 149 (1996).

[8] Y. Hagashi, Spectrochimica Acta **B54,** 109-122 (1999).

[9] IUPAC Compendium of Chemical Terminology, 2nd Ed. (1997).

[10] K. Wittmaack, Appl. Phys. **12,** 149 (1977).

[11] S. Roy, C. Jacob, S. Basu, Solid-State Electronics **47,** 2035 (2003).

[12] A. Kakanakova-Georgieva, Ts. Marinova, O. Noblanc, C. Arnodo, S. Cassette, C. Brylinski, Thin Solid Films **343-344,** 637 (1999).

[13] M.G. Rastegaeva, A.N. Andreev, A.A. Petrov, A.I. Babanin, M.A. Yagovkina, I.P. Nikitina, Materials Science and Engineering **B46,** 254 (1997).

Chapter 7: TOF-RIMS Measurements

7.1 Introduction

Time-of-flight resonant ionisation mass spectrometry (TOF-RIMS) is a useful evolution of TOF-SIMS that overcomes the problem of isobaric interferences and, to a certain extent, the matrix effect that plagues TOF-SIMS depth profiling. By using tuneable lasers to achieve photo-ionisation within the plume of sputtered neutral material, elementally selective and even state selective information about the sample under investigation can be obtained.

This chapter will review the TOF-RIMS depth profiling of Ni/SiC samples at various anneal stages. The experiments were conducted at the Laboratorium voor Vaste-stoffysica en Magnetisme at the Katholieke Universiteit Leuven. Two independent laser systems were employed consisting of a Nd:YAG pumped pulse dye laser (PDL) and an optical parametric oscillator (OPO), also pumped by a Nd:YAG laser. The first experiments probed the a^3F_4 ground and a^3D_3 first excited states of Ni, whilst depth profiling Schottky and Ohmic Ni/SiC samples. This provided insight into the bonding mechanisms occurring in such samples. Experience gained from the analysis of the initial results of these profiles, along with TOF-SIMS results obtained in Swansea, suggested that enhancements in the depth profiling procedure were required to improve the quality of the results. This focused on optimising the profile and homogeneity of the primary ion beam exposed to the surface such that the crater eroded was as uniform as possible. A test sample was depth profiled as a control standard to determine the optimum conditions for depth resolution, the results of which are presented in Section 7.4.1.

With the optimum conditions established, further depth profiles on as-deposited Schottky and annealed Ohmic Ni/SiC samples[1], again probing the ground and first excited states of Ni and these are presented in Section 7.5. Another set of depth profiles, probing the $^3P_2$ state of Si along with non-resonant ionisation of Ni, were performed to establish the location of the interfacial region within the samples such that comparison with the Ni/Ni* profiles could be made (Ni – ground state, Ni* - excited state). This also allowed a direct comparison to the TOF-SIMS data. The results of all these depth profiles are summarised and discussed within the conclusion section at the end of this chapter.

7.2 Velocity distributions and population partitions of nickel and associated silicides

The process of sputtering causes the emission of secondary particles in a variety of charge and excitation states with an associated distribution of velocities as described in chapter 3, section 3.6. The secondary particles that are emitted in ionic form are utilised in SIMS techniques, although they account for a very small percentage of the total secondary particles emitted. However, there is a wealth of information present in the neutral species that typically comprise in excess of 90% of the sputtered material in most cases. The objective of the RIMS studies was to probe the neutral atoms of different electronic states sputtered from Ni/SiC samples by means of laser ionisation of specific neutral atoms. The distribution of atoms present in each electronic state is referred to as a population partition and can reveal information about the sample surface under investigation. The three primary elements in the samples used in these studies, namely Ni, Si and C, can all be explored in RIMS schemes. (Note: Ionisation schemes for numerous elements can be found in the extensive papers published by Saloman[2,3,4,5]).

(a) Nickel contains an array of metastable states over a wide range of excitation energies with various electron configurations[6]. A great deal of research has been undertaken to determine efficient ionisation schemes for nickel but this research concentrated primarily on the a^3F_4 ground and a^3D_3 first excited states, which are typically among the highest populated states in the nickel compounds relevant to these studies.

(b) Silicon also has a number of metastable states available for resonant ionisation. In these studies, the $^3P_2$ state was probed simultaneously with a non-resonant nickel excitation using a single laser system. This profile enabled comparison with TOF-SIMS data in chapter 6.

(c) Owing to its low number of bound state electrons, carbon is a particularly difficult element to photo-ionise. This is due to the low number of transition possibilities and a lack of screening from inner orbital electrons. Using single-photon excitation, only the two lowest-lying metastable states are easily accessible for RIMS, but not the ground state.

7.3 TOF-RIMS depth profiling of Ni/SiC samples

The RIMS depth profiling utilised a 15keV Ar^+ primary ion beam divided via blanking plates to form a series of alternating ion pulses at a frequency of 10Hz. A typical cycle showing the ion pulse scheme and laser firing times is shown in Figure 7.1.

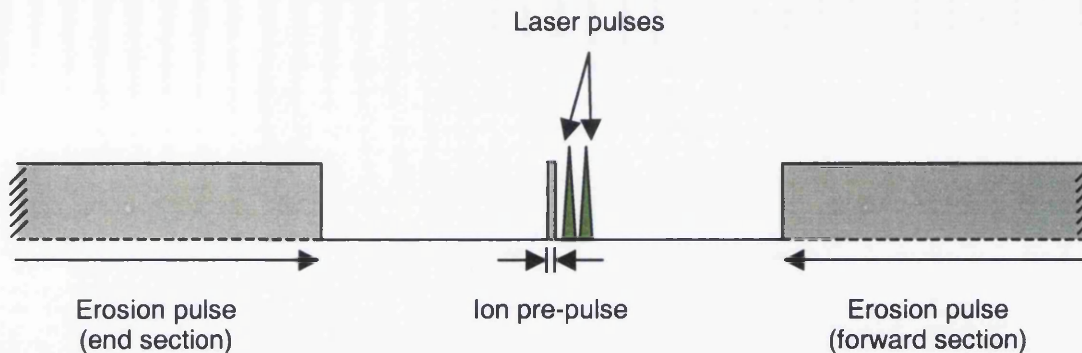

Figure 7.1: Timing diagram of ion and laser pulsing scheme. The two laser pulses are staggered to permit discrimination between the photo-ion signals associated with each.

The first ion pulse, known as the pre-pulse, is a short pulse typically of the order of 100ns to several μs, which is used to sputter material from the target sample to be intercepted by the laser pulse(s) at a distance, d, from the sample surface. The interaction between the laser pulse and the sputter volume causes photo-ionisation of the species to which the laser is tuned. The extraction system is also pulsed to reject initial SIMS ions and permit photo-ionised material to pass down the TOF tube to the detector assembly. A second ion pulse, following extraction of the photo-ions, is used to erode material for the depth profile. The pulse-width of this ablation pulse permits a user-defined erosion rate to be established. The section of the velocity distribution to be probed is determined by the distance between the intercept point of the laser pulse with the sputtered plume and the sample surface, the acceptance angle of the mass spectrometer and the delay between the ion pulse impact on the surface and the laser firing time.

In the first experiments, an ion pre-pulse of 3.3μs was used to sample a major portion of the Ni velocity distribution in each case, effectively probing the population of the Ni electronic states of interest. It was decided to use a long pre-pulse to obtain increased signal, as the signal itself was too low in this case to use a shorter pulse for probing of a section of the velocity distribution. In these first experiments, the a^3F_4 ground state and a^3D_3 excited state were simultaneously analysed by setting each of the laser systems to

ionise an individual electronic state via a one-colour, two-step resonant ionisation scheme as shown in Figure 7.2. The OPO system was set to 322.698nm to resonantly excite and ionise the ground state a^3F_4 atoms, while the PDL system was set to resonantly excite and ionise 0.03eV a^3D_3 excited state atoms using 324.846nm radiation. Both ionisation schemes made use of the intermediate metastable state z^3G_4.

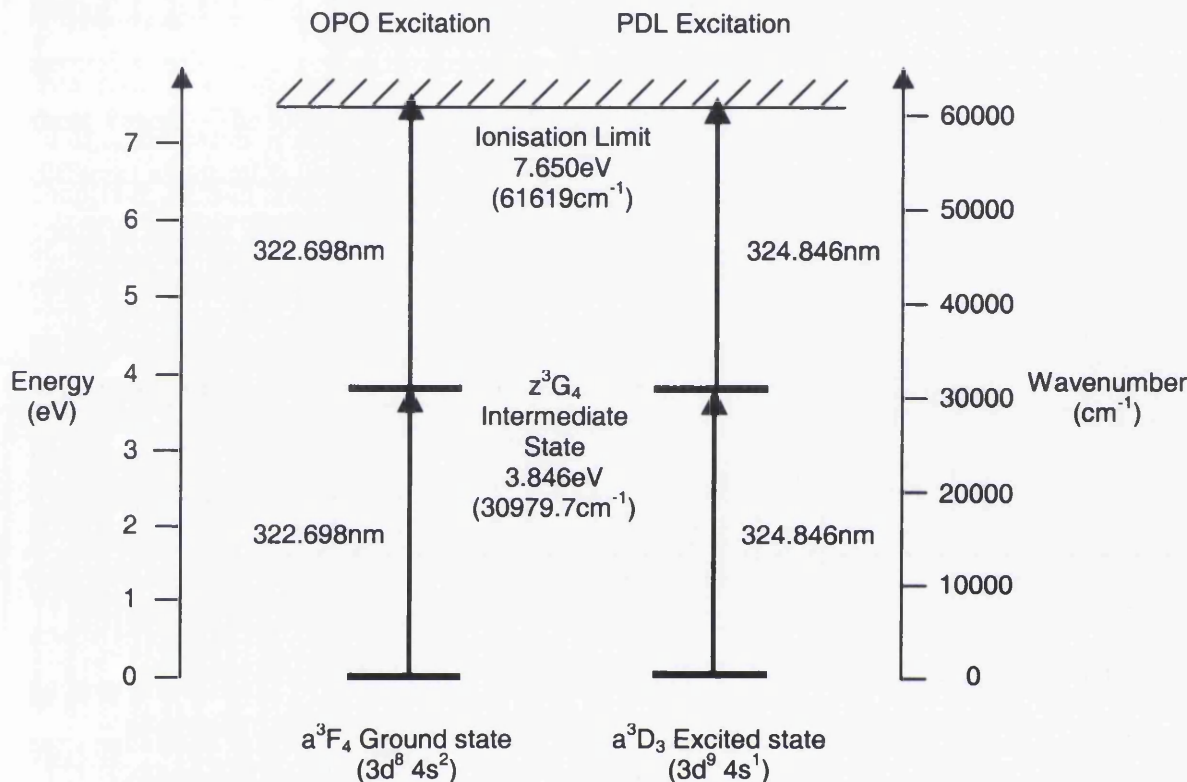

Figure 7.2: Ionisation procedure for sputtered Ni atoms in the a^3F_4 ground state and a^3D_3 first excited state using one-colour two-step schemes. Note that the wavelength readings are in air.

A typical mass spectrum of Ni obtained using the RIMS system in linear mode (i.e. without the reflectron operational) is shown in Figure 7.3. Four of the five Ni isotopes can be clearly observed, while the fifth isotope peak Ni^{61} is in fact enveloped by the Ni^{60} peak, although its existence can be inferred due to the asymmetry of the Ni^{60} peak. A clear appraisal of the Ni^{61} peak could be made by initiating the reflectron mode, although the detected signal would be substantially inferior to that obtained in linear mode. These studies involve measuring the population of specific electronic states rather than identifying individual isotope peaks, hence it is the magnitude of the signal that is of higher importance than ultimate mass resolution. In addition, as the Ni contact layer is consumed and the SiC substrate reached, the Ni signal will decrease through this interface hence the greater the magnitude of the Ni signal, the greater the chances of

detecting changes in the two states relative to one another as the Ni concentration reduces.

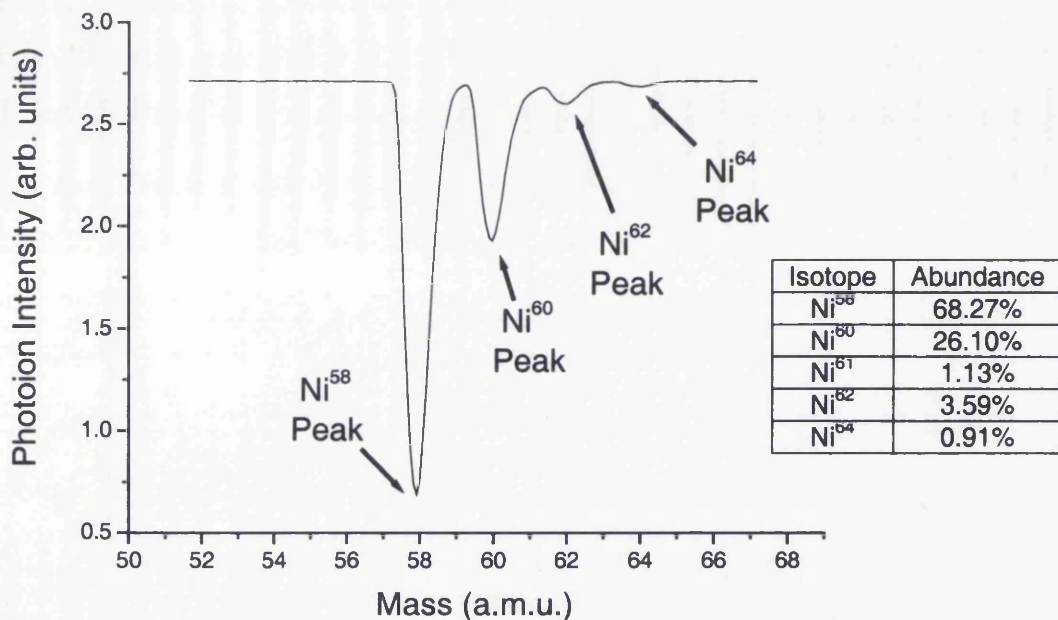

Isotope	Abundance
Ni^{58}	68.27%
Ni^{60}	26.10%
Ni^{61}	1.13%
Ni^{62}	3.59%
Ni^{64}	0.91%

Figure 7.3: Mass spectrum of Ni obtained from RIMS system using one laser system. A second series of peaks produced with the second laser system would be delayed by an interval Δt, such that the separate Ni signals could be discriminated. A table of the relative abundance of the Ni isotopes is provided (Source: NIST website nist.gov).

In order to differentiate between the signals corresponding to the two electronic states, a 1μs delay was inserted between the firing times of the two laser systems, as shown schematically in Figure 7.1. This resulted in photo-ionisation and hence detection of the ground state Ni and excited Ni* atoms at different times thus separating the two signals. Since the long pre-pulse used dictated that almost the entire velocity distribution was being probed, the effect of the time delay is negligible. The photo-ion signals plotted represented an average of 300 pulse events to reduce and effectively eliminate systemic fluctuations during the acquisition.

7.3.1: RIMS depth profiling of Schottky Ni/SiC sample

The first sample to be depth profiled was a Schottky Ni/SiC sample consisting of a 200nm Ni contact layer deposited on the SiC substrate in UHV at room temperature, as described in Chapter 4, Section 4.4. The same sample was also depth profiled using the TOF-SIMS system in Swansea, the results of which are described in Section 6.2. The RIMS depth profile is shown in Figure 7.4, where the photo-ion intensities of the a^3F_4

Ni ground state and a^3D_3 Ni* excited state versus ion fluence are plotted in (a) and the ratio of the excited to ground state versus ion fluence is also plotted in (b).

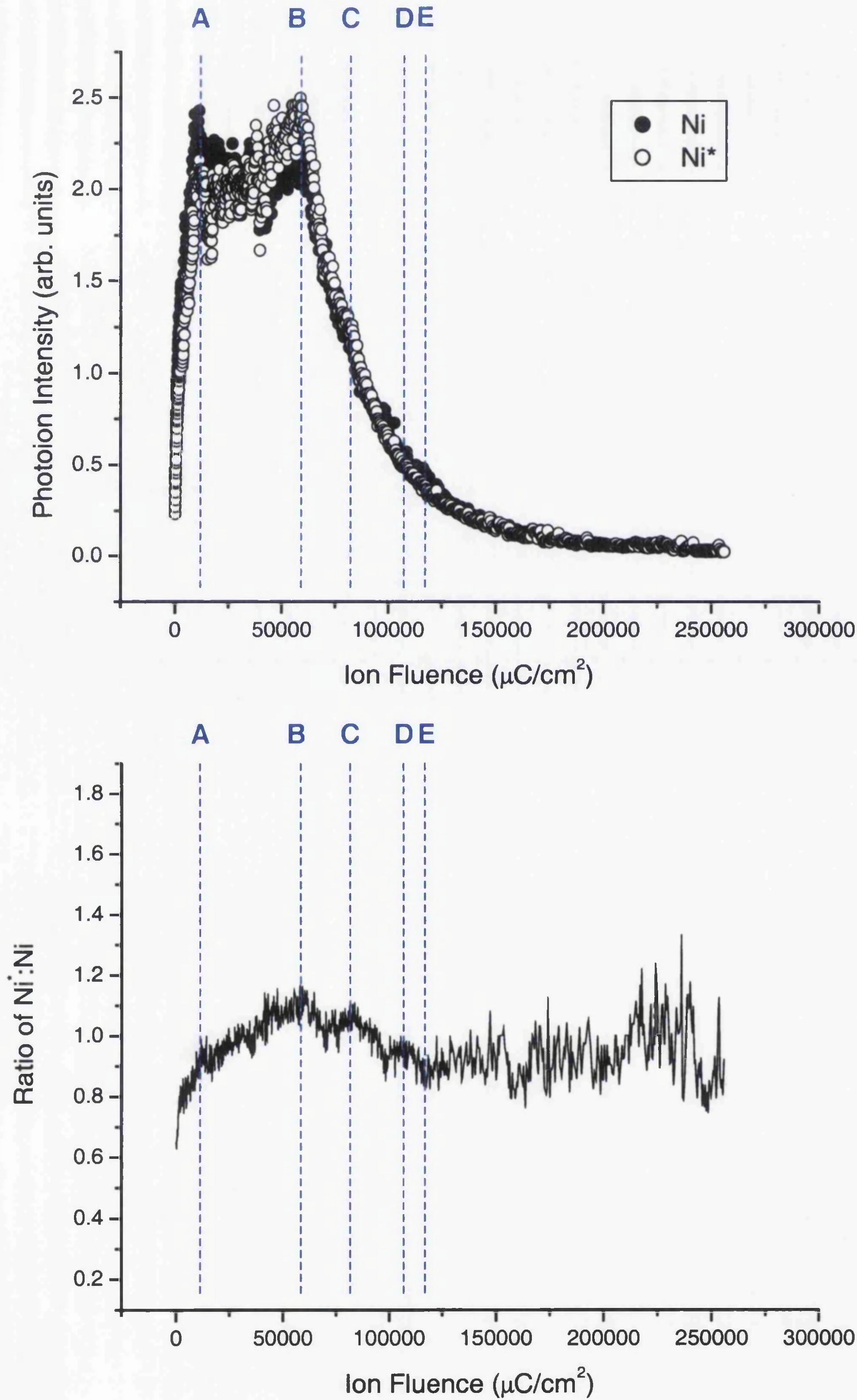

Figure 7.4: RIMS depth profile of as-deposited Ni/SiC Schottky sample (15keV Ar^+) at first location; (a) plot of photo-ion intensities of Ni (Ground state) and Ni^* (Excited state), (b) plot of ratio of Ni^* to Ni. Points A, B, C, D and E are marker points of interest.

The depth profile obtained shows a sharp rise in both photo-ion signals as the top oxide layer is consumed. This may be explained by secondary ion enhancement due to the presence of oxygen, which naturally reduces the secondary neutral yield by an equivalent magnitude. Following erosion of the oxide layer at marker point A, a region of "pure" Ni is profiled whereby the photo-ion signals of both states proceed at a far more constant level until reaching marker point B. However, as the Ni contact layer is probed between marker points A and B, the excited state signal gradually rises whilst simultaneously, the ground state signal falls by a similar amount. Observation of the ratio between the excited and ground state signals over the corresponding range demonstrates this effect quite clearly. The rate of rise of the ratio signal over this region is particularly constant suggesting the effect may be caused either by ion beam inhomogeneity or a change of bonding mechanism within the over-layer. Since the laser energy was monitored throughout the profile to ensure a constant level, fluctuations in the laser system efficiency can be excluded. TEM studies by other authors [7,8,9] have shown that as-deposited Ni/SiC samples exhibit a very sharp interface suggesting that any bonding mechanism between the contact layer and the substrate may only be present over a short range. Certainly, such a mechanism would be very unlikely to extend over the range of the contact layer hence the rise in the ratio signal is most likely attributed to ion beam inhomogeneity.

As the Ni layer is eroded fully, a distinct drop in both signals is observed beyond marker point B, corresponding to the presence of the interface. This is an encouraging feature as it confirms the expectation that the interface is abrupt. The profiles then tail off more gradually due to the different matrix being probed. As such, the depth profile obtained shows good agreement with the depth profiles obtained on Schottky samples using TOF- SIMS in Chapter 6. Indeed, the "tailing-off" of the interface was also present in the TOF-SIMS profiles. Si and C have far lower sputter yields than Ni, hence more time, and thus sputter ion fluence, is required to erode a specific thickness of SiC compared to Ni.

Over the interface region, the ratio of the excited and ground states of Ni from marker points B to E shows a very obvious decrease interspersed with a series of fluctuations over the region. The decrease beyond point B is followed by a rise in the ratio signal to point C, which precedes a similar recurrence at point D resulting in three distinct peaks at marker points B, C and D along with associated troughs between these points.

Inhomogeneity within the ion beam tends to manifest itself in very gradual changes in the signal rather than the rather abrupt features described here. This is because the centre of the beam erodes at a greater rate than the peripheral regions. Consequently, when considering the beginning of the profile, the centre of the beam may rapidly consume the oxide layer and proceeded to erode the subsequent layer while the outer regions of the beam are still eroding the oxide layer. Thus, a combination of signals at different depths would need to be analysed simultaneously. As a result, any sudden change in the composition of the sample will appear far less discrete hence the features described at B, C and D could be particularly short-range variations in the composition of the sample. It should be noted while fluctuations in ion gun or detector efficiency can be excluded (since both signals would exhibit comparable changes), variation in the efficiency of one of the laser systems could be a cause the features described. However, throughout the experiment, the laser energy remained very constant. Therefore, the fluctuations observed point to the presence of varying composition matrices. This recurrent finding will be discussed again later in this chapter.

The decrease in the ratio of the excited state to ground state through the interface indicates that occupation of the *3d*-band is reducing with the Ni concentration in the sample. The resonance electron transfer model described in Chapter 3, Section 3.6.1, states that atomic states with bulk-type electron configurations are preferentially populated hence the bulk configuration is changing through the interface. Bisi *et al* [10] have proposed that *3d*-band occupation decreases as Ni concentration within Ni-silicide decreases, tending towards a more atomic-like configuration. It is difficult to ascertain whether transitions from bulk Ni to Ni-silicide to atomic-like Ni are taking place or merely a single transition from bulk Ni to atomic-like Ni. However, the TOF-SIMS experiments point toward a limited range formation of Ni-silicide at the interface, thus inferring that a bonding change from Ni-Ni to Ni_x-Si_y is manifest by a decrease in the excited/ground state ratio as seen in this profile.

In these first RIMS experiments, the ion beam cross-section incident on the sample measured 2mm x 2mm, while the samples used measured 5mm x 5mm. Without the ability to observe a secondary electron image of the sample and hence the ion beam target location, it was difficult to acquire multiple profiles from a single sample. An example of the problems faced when attempting to repeat a depth profile measurement from the same sample is shown in Figure 7.5.

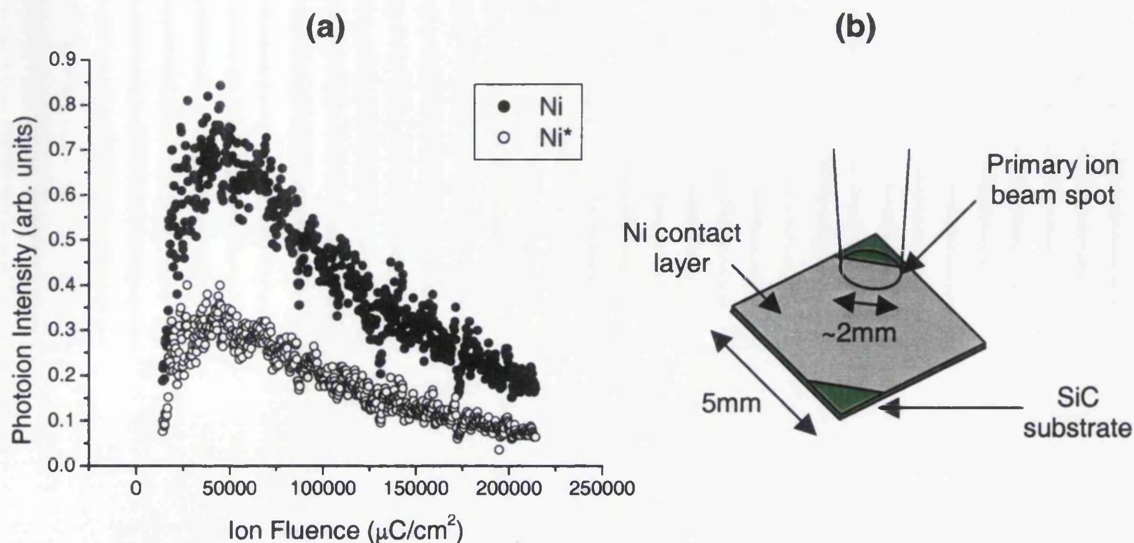

Figure 7.5: (a) RIMS depth profile of as-deposited Ni/SiC Schottky sample (15keV Ar^+) at second location with primary ion beam only partially striking sample as shown schematically in (b).

In this particular depth profile, the ion beam was not fully striking the sample as depicted in Figure 7.5 (b) and shown by the low photo-ion intensity, the scatter of the data points and the general lack of definition of features in the profile. Indeed, both signals rise then fall with no apparent change between the oxide layer and the bulk Ni layer. The fact that the time required to complete the profile was comparable to that in Figure 7.4 suggests that a major portion of the beam was still exposed to the sample. Nevertheless, it was necessary to ensure that the ion beam had been fully incident on the sample for each profile.

7.3.2 RIMS depth profiling of Ohmic Ni/SiC sample

With the depth profile of a Schottky Ni/SiC sample completed, an Ohmic sample was inserted to be depth profiled using the same parameters as used in the depth profile of the Schottky sample since the method appeared sufficient to identify chemical changes. The sample consisted of a 100nm Ni over-layer deposited on a SiC substrate in UHV at room temperature, which was subsequently annealed to 950°C. The thickness variation from the Schottky sample was an unfortunate result of the difficulties encountered when depositing in UHV. I-V measurements confirmed that devices made this way no longer exhibit a rectifying electrical nature. The RIMS depth profile is shown in Figure 7.6, while a repeat profile with excessive noise is shown in Figure 7.7.

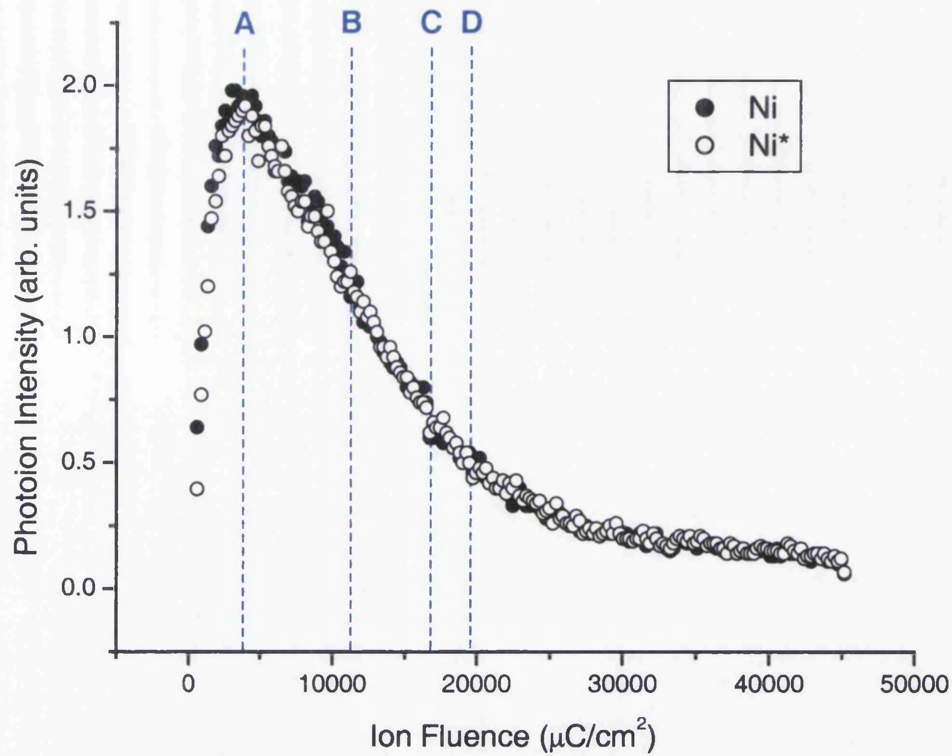

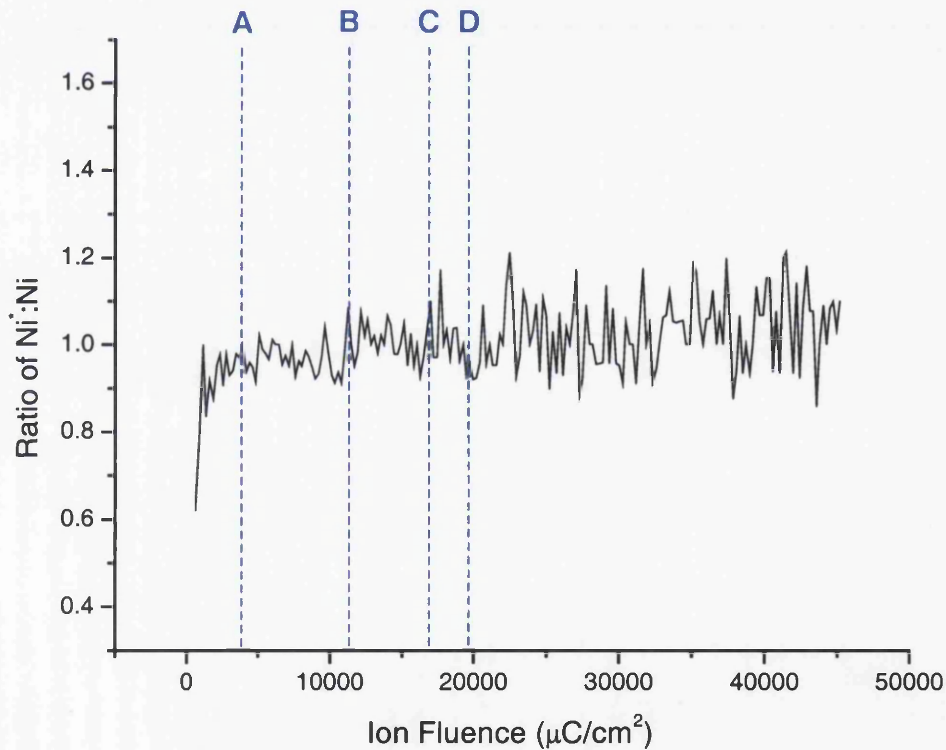

Figure 7.6: RIMS depth profile of Ni/SiC Ohmic sample annealed to 1000°C (15keV Ar+) at first location; (a) plot of photo-ion intensities of Ni (Ground state) and Ni* (Excited state), (b) plot of ratio of Ni* to Ni. Points A, B, C and D are marker points of interest.

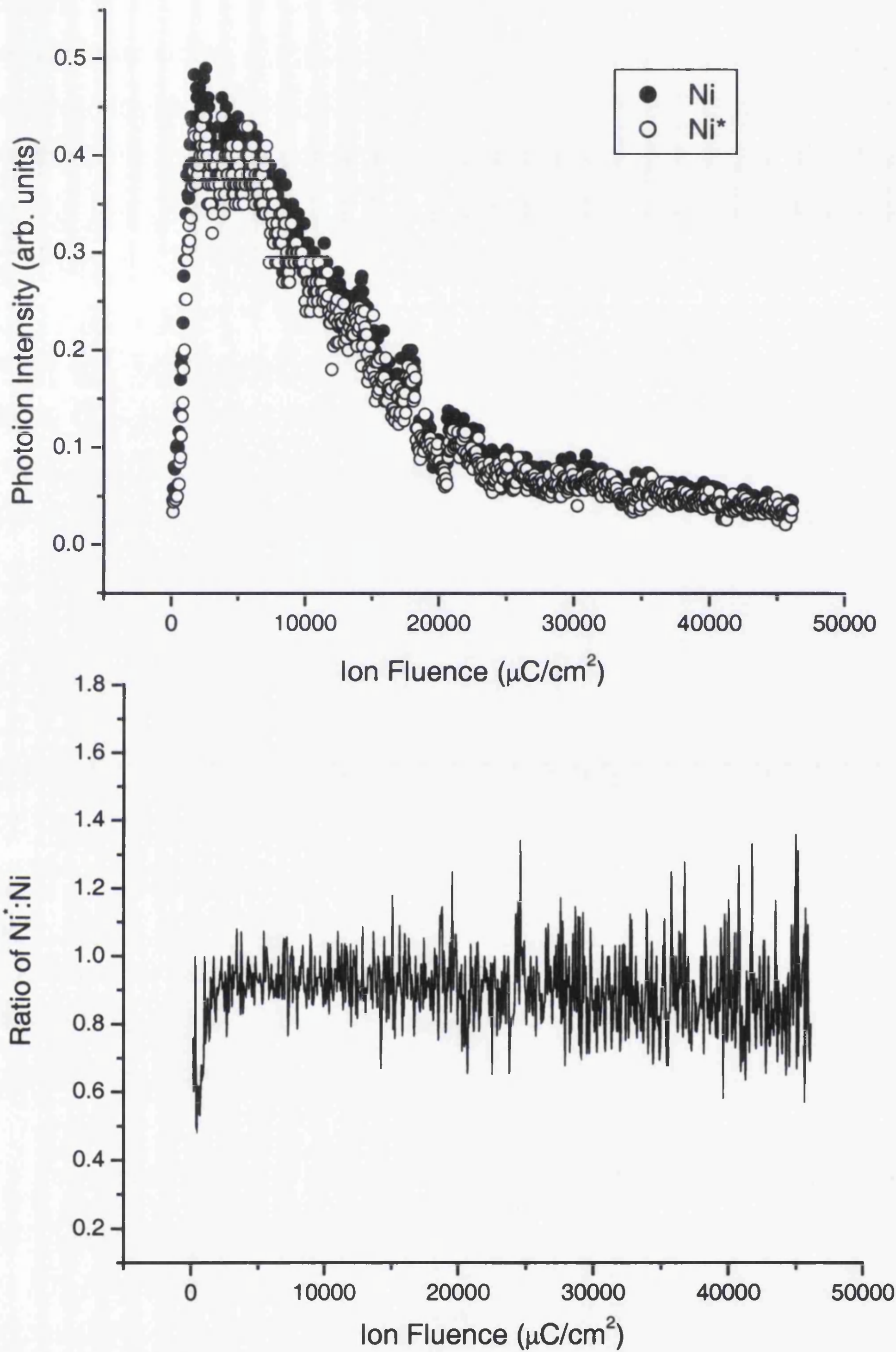

Figure 7.7: RIMS depth profile of Ni/SiC Ohmic sample annealed to 1000°C (15keV Ar^+) at second location; (a) plot of photo-ion intensities of Ni (Ground state) and Ni^* (Excited state), (b) plot of ratio of Ni^* to Ni.

Both profiles show the typical rise in the signals as the oxide layer is eroded, with an increase in the population of the excited state relative to the ground state through the layer in agreement with the profile obtained on the Schottky sample. In Figure 7.6 (a), the intensity of all individual signals proceeds to fall off immediately following the

consumption of the oxide layer, identified by marker point A, with no apparent region of pure Ni profiling that was present in the Schottky sample in Figure 7.4. This was possibly due to the thinner Ni layer that had been deposited although the profile obtained from the Schottky sample suggests that a 100nm layer should be sufficient to observe a near steady state region. Consequently, this points to a reaction occurring during the annealing process that modifies the Ni contact layer such that the bulk of the Ni contact layer is altered.

After the turning point following consumption of the oxide layer, the ratio of the excited/ground state of the first profile in Figure 7.6 (b) undergoes subtle variations where the ratio moves between 0.9 and 1.1. Although noise plays a factor, particularly at fluences in excess of 22,000μC/cm^2, regions AB, BC and CD all show variations between each other. These apparent "steps" in the profile of the ratio signal could be indicative of features present within the sample, as in the Schottky sample interface, although the evidence is less conclusive in this profile due to the higher level of scatter in the data points comprising the ratio profile. Beyond a fluence of 20,000μC/cm^2, the signal-to-noise ratio is too poor to obtain any additional meaningful data.

The effect of excessive signal-to-noise is also present in the repeat profile in Figure 7.7 (b) due to a reduction in the photo-ion signal across the entire profile. The photo-ion signal reduction in this profile was caused by variations in the experimental apparatus. Indeed, the magnitude of the photo-ion signal is dependent on so many factors that it requires only a minor drop in efficiency in each to result in significant loss of signal. Nevertheless, while reasonably quantitative data on the ratio may not be extracted form this profile, the clear similarity in the form of the profile to the first profile serves to confirm that the form of the first profile is accurate.

7.3.3 Evaluation of RIMS depth profiling

The depth profiles obtained from a Schottky sample and an Ohmic sample indicate distinct differences between the two types. Firstly, the Schottky sample exhibits a region of fairly steady state erosion as the Ni contact layer is eroded whereas the Ohmic sample shows no such region. Indeed, following the erosion of the oxide layer, where both samples show very similar characteristics, the Ni photo-ion signal proceeds to fall off instantly with no evidence of an appreciable contact layer. It should be noted that the thinner layer deposited on the Ohmic sample requires that direct comparison

between the two profiles is not straightforward and has to be done with caution. Nevertheless, the fact that no apparent steady state region exists in the Ohmic profile points to a modification of the sample structure with the Ni layer reacting with the substrate and diffusion of chemical species.

The second major difference between the profiles of the two sample types involves the progression of the ratio of the excited state to ground state signals. The Schottky sample shows a gradual rise in the ratio up to the interface coupled with a distinct decrease after the Ni contact layer has been consumed. The Ohmic sample profiles show far less variation in the general trend of the ratio signal although the first profile (Figure 7.6) shows a number of regions in which the ratio changes subtly. A number of step-like fluctuations were also present in the Schottky profile, albeit more pronounced. The ratio profile of the Ohmic sample shows far more scatter than the Schottky sample suggesting that the contact layer of the Ohmic sample may be far less homogeneous than the Schottky sample.

Upon removal of the samples from the system, a distinctive bevelled crater of near-circular cross-section was observed. The ion beam fluence had quite clearly not been homogeneous, thus resulting in substantially increased erosion at the centre of the crater compared to the periphery. Consequently, each point of the depth profiles obtained would consist of information from differing depths with the effect worsening with increasing sputter time. A major example of how this affected the profile manifests itself in the gradual decrease of both signals through the interface of the Schottky sample, although this may also be attributed to the matrix change with the associated sputter yield variation. Therefore, it was necessary to circumvent this inhomogeneity by some means in order to achieve reliable and accurate depth profiles.

7.4 Optimisation of RIMS setting using a defocused primary ion beam

Without the ability to raster the beam on the Leuven system, it was necessary to optimise the beam spot profile on the sample surface. The early profiles at Leuven had used a primary ion beam that had been generally optimised for maximum current delivered to enhance the collision cascade and hence the emission of secondary particles. However, before these profiles had been initiated, a phosphor screen was inserted prior to the sample to determine the intercept location of the ion beam on the sample by the observing fluorescence on the screen due to the ion beam. The phosphor

screen also enabled a rough appraisal of the uniformity of the current density of the ion beam to be made. Before the phosphor screen was removed, the primary ion column controls were adjusted to produce the most homogeneous beam profile.

Following the depth profile of the Schottky Ni/SiC sample (Figure 7.4), a crater of substantial area was observed at the profile location. The crater area measured 2mm x 2mm but the centre region was clearly deeper than the peripheral area. Indeed, the physical manifestation of the Gaussian nature of the ion beam was apparent by analysing the profile of the crater. This inherent inhomogeneity over the cross-section of the ion beam is detrimental to depth resolution and increases as the sample is probed deeper. To this end, the method used to combat this factor was to install a diaphragm aperture within the primary ion column, just prior to the sample as shown in Figure 7.8.

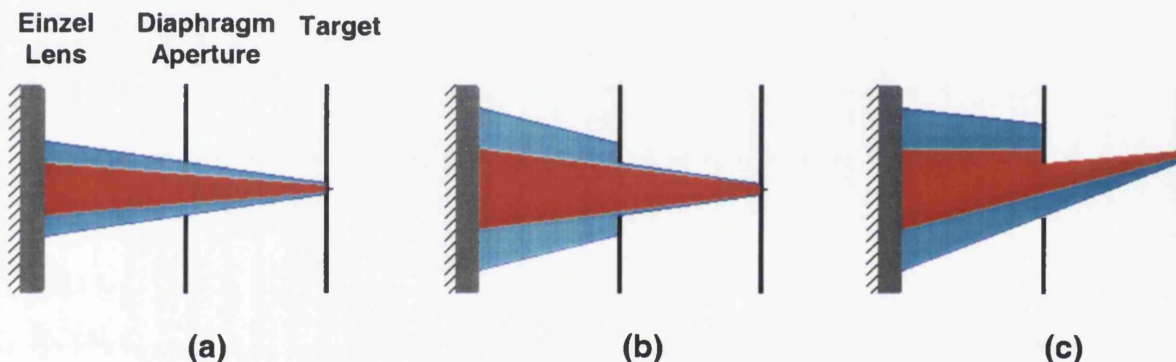

Figure 7.8: Effect of defocusing the ion beam and passing it through a diaphragm aperture. The red section of the ion beam represents the inner region of maximum current density, while the blue section represents the outer region where the current density is lower. In (a) the ion beam is focused to a spot on the target surface. The full range of current density is exposed to the sample hence low depth resolution. In (b), the outer region of the beam is removed permitting only the centre section to proceed to the sample. Less variation in the current density across the beam occurs thus depth resolution is improved. In (c), the beam has been steered off the central axis causing half the beam to be removed by the aperture and half to continue thus resolution will be comparable to condition (a).

In arrangement (a), the beam is highly focused such that the entire beam passes through the aperture. This is identical to situations where the aperture is not present. In such situations, the crater produced by the ion beam is uniform in depth as a result of more rapid erosion of the centre region compared to the outer areas, thus a bevelled crater is formed. This means that an acquisition obtained from this crater would be a

superposition of signals from differing depths within the sample. Consequently, depth resolution is limited and reduces with further sample erosion.

A defocused beam, such as that shown in arrangements (b) and (c), causes a section of the beam to be blocked by the aperture. In (b), the outer regions of the ion beam are incident on the aperture plate surface, allowing only the central area to proceed to the sample surface. This effectively eliminates the "shoulders" of the Gaussian profile of the beam, enabling a beam of more uniform current density to be used for depth profiling. A variation across the profile of the remainder of the beam will still be present but a compromise must be sought that yields sufficient ion current on the sample to permit profiling of the sample in a reasonable timescale.

Arrangement (c) represents a condition where the defocused ion beam is not incident at 90° to the plane of the aperture. This causes a beam of very uneven distribution to be incident on the sample, resulting in a similar loss of resolution as arrangement (a). Consequently, it was most important that any steering of the beam off the central axis was limited.

7.4.1 RIMS depth profiles of test sample

In order to quantify the effect of defocusing the primary ion beam and inserting a diaphragm aperture to remove the outer regions of the beam, depth profiles were undertaken on a test sample at varying beam focus settings. The sample consisted of a 5nm silver top layer, 5nm nickel layer, 5nm silver layer and a 5nm nickel layer grown upon a magnesium oxide substrate by molecular beam epitaxy in Leuven. At the time of testing, only the pumped dye laser (PDL) was available for experiments. By setting the wavelength to 280.507nm, a one colour, two-photon scheme was used to obtain resonant $^3F_4$ Ni signals (via the $^1F_3$ intermediate state) along with a non-resonant Ag signal.

Four of the depth profiles obtained using 15keV Ar^+ primary ions and using variable focus settings are shown in Figure 7.9. A conversion to actual depth is extremely difficult due to markedly different sputter yields of the layered species. Therefore, the profiles are plotted as a function of primary ion fluence delivered to the sample as fluence takes the primary ion current and beam area into account, whereas sputter time contains multiple variables.

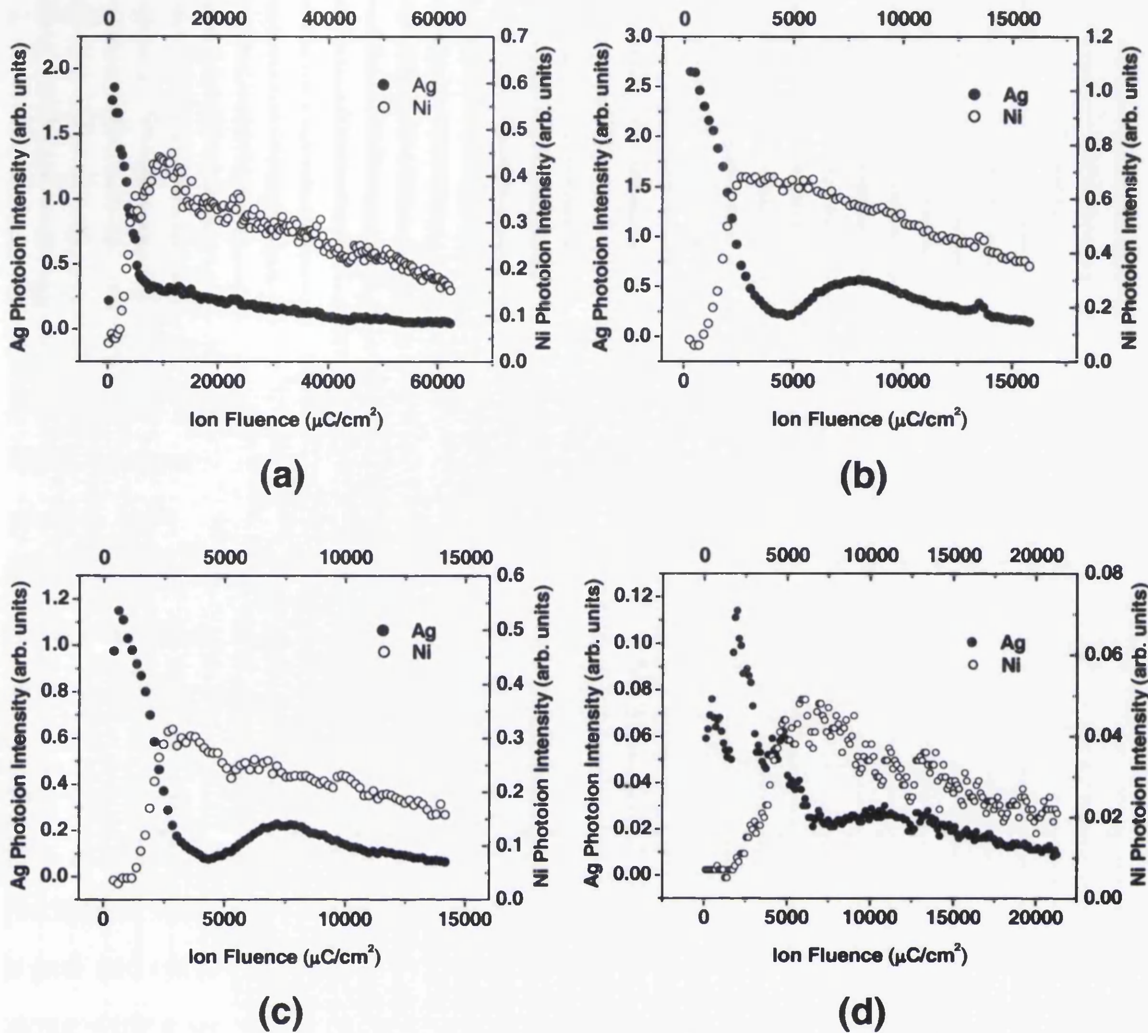

Figure 7.9: 15keV Ar^+ RIMS depth profiles of test samples with variable focus lens settings (a) 7.2kV (1.25μA primary ion current), (b) 5.8kV (0.72μA primary ion current), (c) 4.8kV (0.32μA primary ion current), (d) 4kV (0.2μA primary ion current). The aperture was only installed in profiles (b), (c) and (d).

Figure 7.9 (a) represents a situation where the diaphragm aperture is not present and the focusing Einzel lens is set to 7.2kV to produce a well focused beam on the sample surface, i.e. it depicts the conditions under which the first depth profiles of the Ni/SiC samples were acquired. From the beginning of the profile, a decrease in the intensity of the silver signal with a corresponding increase in the Ni signal is clearly observed, representing consumption of the first silver layer and progression into the first Ni layer. However, this is the only apparent occurrence of a transition within the profile, as both signals gradually decrease showing little or no variation with subsequent layers. This implies that depth resolution is significantly decreasing with depth. This effect of inhomogeneity in the beam fluence naturally reduces depth resolution as mentioned

earlier but it is magnified further when layered species are probed that have distinctly different sputter yields.

In profile (b), the diaphragm aperture has been installed and the voltage applied to the focusing Einzel lens reduced to 5.8kV, to permit defocusing of the beam. Immediately, it is clear that it is a multi-layered sample that is being profiled as an increase in the Ag signal is observed following a fluence of approximately 5,000$\mu C/cm^2$ of primary ion current This indicates the presence of a second Ag layer coupled with a corresponding, albeit small decrease in the Ni signal following a fluence of 7,000 to 8,500$\mu C/cm^2$. There is insufficient evidence to propose that the second Ni layer is visible from the profile, only a minor "hump" in the Ni signal from approximately 8,500 to 11,000$\mu C/cm^2$ suggests the possible presence of such a layer. The small hump in both signals at about 13,500$\mu C/cm^2$ is caused by a temporary increase in the laser power resulting in increased resonant ionisation and, as such, may be ignored.

The ion beam was further defocused, by reducing the voltage applied to the focusing lens to 4.8kV, as shown in Figure 7.9 (c). The best depth profile, in terms of depth resolution, was obtained on the sample using these settings. Again, a decrease in the Ag signal and corresponding increase in the Ni signal is observed from 0 to 3,000$\mu C/cm^2$ along with a second increase in the Ag signal at 4,000 to 5,000$\mu C/cm^2$. However, a more definite rise in the Ni signal at approximately 9,000 to 9,500$\mu C/cm^2$ can be seen, representing the second Ni layer. Whilst the rise is not as pronounced as the first rise, it does show that a significant improvement in the depth resolution was achieved using this set-up, especially considering the thin nature of these layers.

Further defocusing of the ion beam was undertaken by reducing the focusing lens voltage to 4kV. The depth profile obtained, shown in Figure 7.9 (d), demonstrates that the limit of defocusing the beam has been surpassed for this system. The depth resolution has dropped substantially compared to profile obtained in (c) and indeed, it is barely superior to the profiles obtained without an aperture in place. The problem is primarily due to the lack of ion current striking the sample due to excessive defocusing and the section of the ion beam exposed contains the greatest proportional fluence variation, i.e. the centre section. The lack of ion current striking the sample resulted in limited secondary particle emission; hence the photo-ion intensity was approximately an

order of magnitude lower than previous profiles resulting in a substantial increase in the scatter of the data points.

Further testing using lower energy ions of 10keV were undertaken along with a profile that used a 10kV acceleration voltage coupled with a 3.8kV sample bias to further reduce the incident energy. Neither profile showed an improvement in depth resolution, while the photo-ion intensity was low in both instances. Consequently, it can be concluded that to achieve optimum depth resolution when depth profiling with this system, the focusing lens must have an applied voltage in the region between 4kV and 5.8kV when profiling at 15keV, with the sample bias set at 4.8kV.

7.5 TOF-RIMS depth profiles of Ni/SiC samples using a defocused beam

The depth profiles performed on the test sample had demonstrated that the use of a defocused primary ion beam and installation of a pre-sample diaphragm aperture resulted in superior depth resolution when compared to the initial set-up. The new arrangement permitted definite discrimination of three of the thin layers and also indicated the presence of the fourth layer, whereas the original arrangement barely enabled two layers to be discerned. Therefore, with just a single layer of Ni deposited on the SiC substrate, the aim was to observe a similar improvement on the Ni/SiC samples. Despite the additional thickness of the Ni layer in comparison to those on the test sample, a clear interface was observed on the Schottky sample (in Figure 7.4). Consequently, a sharper interfacial region of the depth profile was expected with the new arrangement.

7.5.1 RIMS depth profiling of Schottky Ni/SiC sample

The Schottky Ni/SiC sample used for depth profiling was produced in the Edwards evaporator as opposed to UHV conditions. The sample preparation technique is described in chapter 4, section 4.4. I-V measurements and TOF-SIMS depth profiles of such samples (see chapter 6.5) had determined that the process yielded good consistency with the UHV samples. A 200nm Ni contact layer was deposited on the SiC substrate as this thickness had been shown to allow a region of steady-state erosion conditions to be achieved prior to probing the interface.

The depth profile of the Schottky Ni/SiC sample plotted the variation of the same Ni states as the earlier profiles, with the a^3F_4 Ni ground state excited with 322.698nm

radiation from the PDL and the a^3D_3 Ni excited state probed using the OPO wavelength set at 324.846nm. The depth profile itself is shown in Figure 7.10, where the photo-ion intensities of the Ni and Ni* states are plotted in (a) and the ratio of the excited to ground state can be seen in (b). As in Figure 7.4, a discernible interface is observed between points A and C on the profile. As a consequence of optimising the photo-ion signals at the start of the experiment, the rise in the signal at the beginning of the profile resulting from consumption of the oxide layer is absent. Point B represents an approximate point of inflexion in both signals, most obviously in the ground state signal, within the interface while point C represents the corresponding inverse points as the profile levels off.

An interesting phenomenon occurs in the ratio between the excited state and ground state through the interface. The effects of the interface are first identifiable in the region between points A and B corresponding to an irradiation fluence of approximately 33,000 – 50,000μC/cm^2 respectively, where the excited state signal falls at a greater rate than the ground state signal, as shown by the Ni*/Ni signal in Figure 7.10 (b). Once again, it can be inferred that the electronic configuration of the bulk matrix is changes at the interface with a decrease in the occupation of the *3d*-band of the Ni sputtered. A similar result was observed in Figure 7.4 over the first section of the interface, which suggests that the new method of defocusing the beam and passing it through an aperture is at the very least producing a consistent profile. The TOF-SIMS depth profiles of Schottky samples point to the presence of Ni-silicide at this region, although the stoichiometry could not be established. However, beyond point B, the excited/ground state ratio undergoes a turning point and proceeds to increase markedly up to point C, representing the point at which the Ni signal profiles begin to level off. This implies that occupation of the *3d*-band is now increasing as the latter half of the interface is probed. Such a distinct rise was not present in the earlier depth profile on the Schottky sample.

A feature identified between points C and D is a small "hump" in both signals located at the end of the interface or indeed within the SiC substrate, the Ni signals present in the region being a possible consequence of ion intermixing. The corresponding point in Figure 7.10 (b) exhibits a near-plateau region suggesting that a new constant matrix, at least over a small depth, is present.

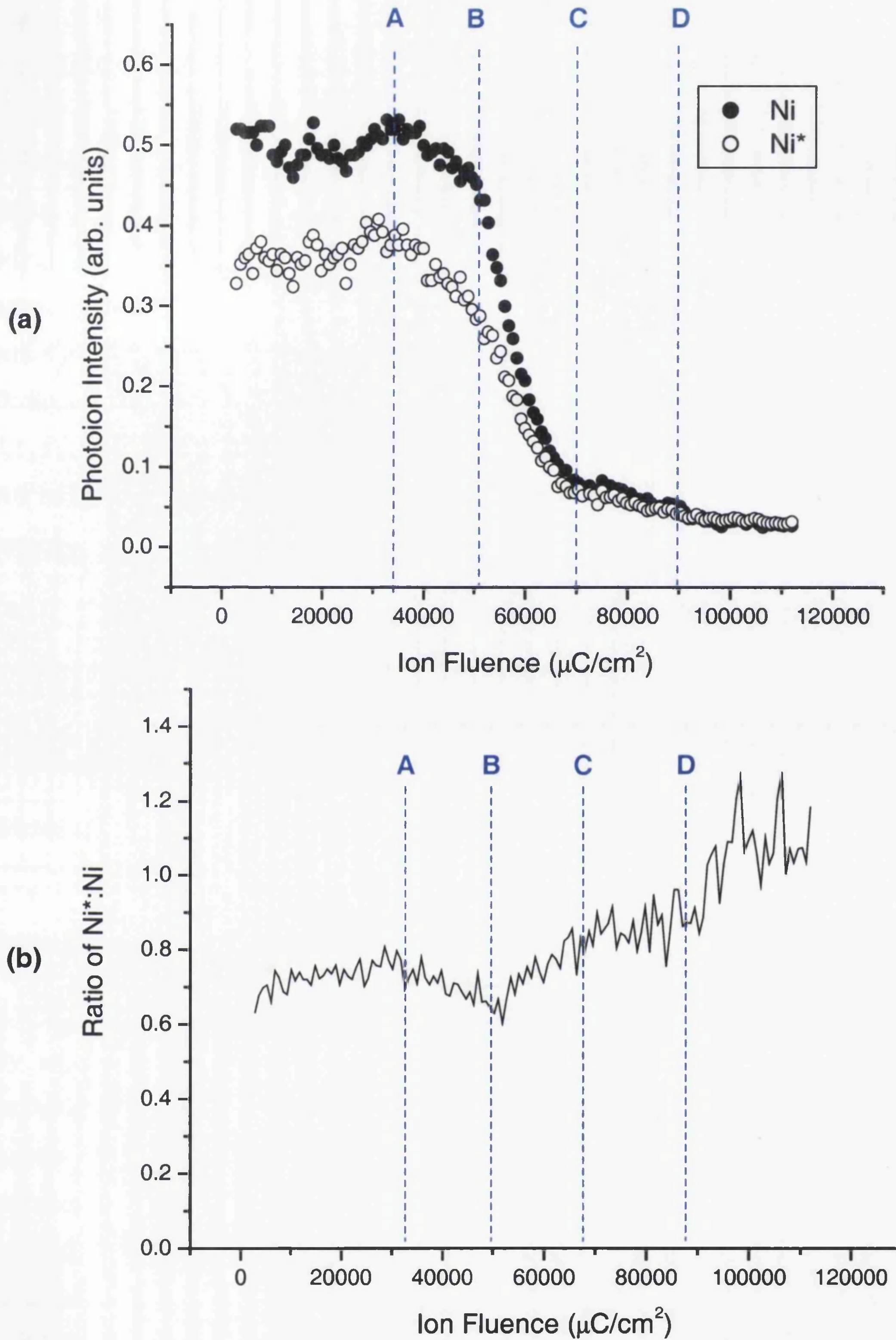

Figure 7.10: RIMS depth profile of as-deposited Ni/SiC Schottky sample using 15keV Ar^+ defocused primary ions; (a) plot of photo-ion intensities of Ni (Ground state) and Ni^* (Excited state), (b) plot of ratio of Ni^* to Ni. Points A, B, C and D are marker points of interest.

Consequently, it is suggested that a second change in bonding mechanism is occurring within the interface of the Schottky sample over a not-insignificant range. The plot of the ratios suggests that it is likely that two distinct Ni-silicide species are present within the interface. Thus, a comparison of the relative ratios of the regions AB and BC could provide further insight. As the signal does not stabilise within the region AB, it is difficult to obtain an exact reference value. The same problem is faced in region BC, whereas region CD has a typical value between 0.85 and 0.90. However, an approximation may be made for the maximum increase in the relative ratio between B and CD of 40-50%. By comparing with the population partition values obtained by Bastiaansen [11] for the a^3F_4 and a^3D_3 atomic states of various Ni-silicides shown in Table 7.1, it can be deduced that the most likely Ni-silicide candidate of the three for region AB is Ni_2Si, while region BC and CD is most likely comprised of NiSi, although the presence of $NiSi_2$ cannot be ruled out.

	Population, n_i		
Atomic State	Ni_2Si	NiSi	$NiSi_2$
Ground state, a^3F_4	1	1	1
Metastable state, a^3D_3	2.14	2.58	2.34

Table 7.1: Populations of the ground and first excited states of Ni after ion sputtering of various Ni-silicides with populations normalised to the ground state population [11].

By adjusting the OPO system to 251.670nm, it was possible to obtain resonant ionisation of the $^3P_2$ Si state along with non-resonant ionisation of nickel using one laser system only. Therefore, a profile could be obtained that could directly compare the variation of nickel and silicon with depth as any system fluctuations could effectively be negated. The benefit of obtaining a RIMS depth profile of both Ni and Si is that it permits comparison with the TOF-SIMS depth profiles obtained in Chapter 6. Since no suitable region could be found to obtain such a depth profile off the Schottky sample used in Figure 7.10, a new sample produced in the same manner was used. The sample was produced during a different session and due to calibration problems, the thickness of the Ni contact layer was only 100nm. Nevertheless, the thickness was deemed sufficient to attempt a depth profile, as shown in Figure 7.11.

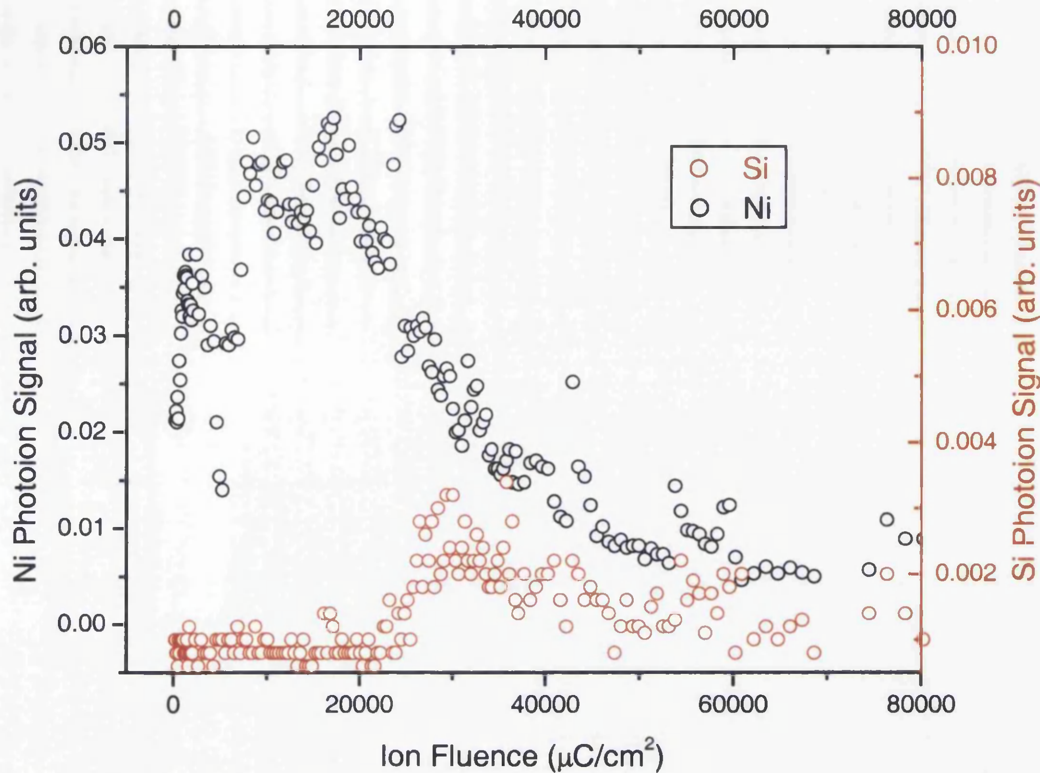

Figure 7.11: RIMS depth profile of as-deposited Ni/SiC Schottky sample using 15keV Ar^+ defocused primary ions. Ni and Si plotted as a function of depth.

Despite inefficient photo-ionisation of the species in comparison to the Ni-Ni* profiles, a clear interface can once again be seen where the Ni signal falls off, coupled with a corresponding rise in the Si signal. This confirms that the suggested location of the interface is indeed true. The decrease in the Si signal following the peak at the interface suggests that a fairly significant matrix change is occurring between the interface and the upper SiC substrate resulting in a greater yield of Si atoms at the interface than in the substrate. Whilst a low sputter yield will naturally account for the inhibition of all species sputtered from the substrate, it does indicate that a reaction is occurring at the interface.

7.5.2 RIMS depth profiling of Ohmic Ni/SiC sample

Following the success of the depth profiles on the Schottky sample described in 7.5.1, an Ohmic sample was used for depth profiling. A 200nm Ni contact layer was also deposited in the Edwards evaporator during the same session as the Schottky sample. Following Ni deposition, the sample underwent an anneal of 1000°C to produce the Ohmic nature. The depth profile of the Ohmic sample, shown in Figure 7.12, used the

same ion bombardment and laser photo-ionisation parameters as were used to profile the Schottky sample shown in Figure 7.10.

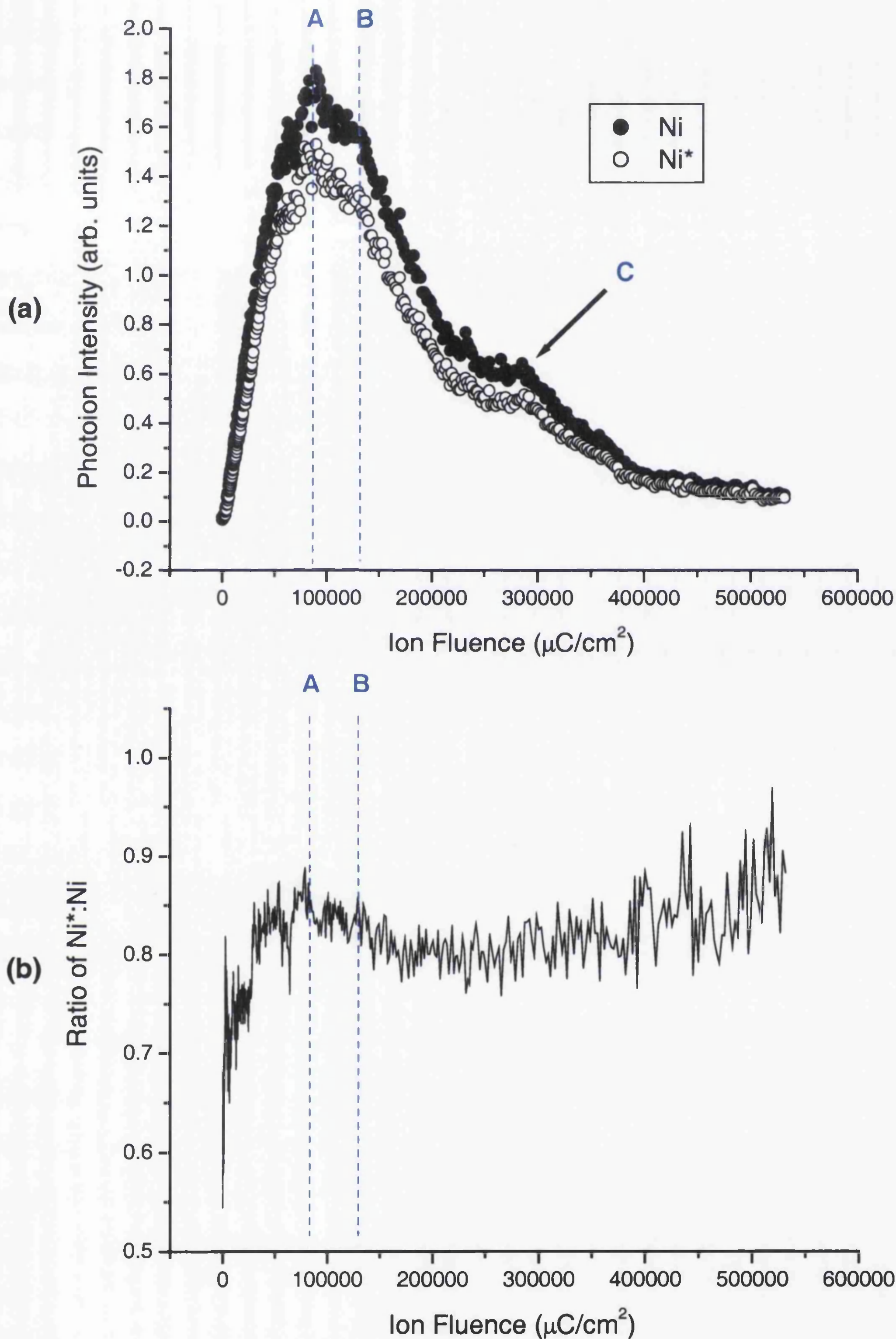

Figure 7.12: RIMS depth profile of Ni/SiC Ohmic sample (annealed to 1000°C) using 15keV Ar^+ defocused primary ions; (a) plot of photo ion intensities of Ni (Ground state) and Ni^* (Excited state), (b) plot of ratio of Ni^* to Ni. Points A, B and C are marker points of interest.

The depth profile obtained reveals additional features that were not observed in the earlier profiles of an Ohmic sample (refer to Figure 7.6 & Figure 7.7). In addition, a visual appraisal of the plot of the excited/ground state ratio shows far less noise in the data and hence more confidence can be taken from this latest depth profile. As with the earlier profiles, both signals rise through the oxide layer to a maximum, highlighted by point A, after which they fall off gradually to point B. At point B, an apparent point of inflexion is observed leading to a sharper fall-off in the signals. A minor "hump" is present in this depth profile, highlighted by point C. However, whether this hump has any connection with the one present in Figure 7.10 would require further study. Note that an attempt is made later to explain this actual phase change in the depth profile by interpreting the Ni/Si profile measurement shown in Figure 7.13.

Despite the difference in the form of the Ni signal profiles in comparison to the Schottky sample, e.g. the lack of a plateau region corresponding to the Ni contact layer, the profile of the ratio of the two electronic states, shown in Figure 7.12 (b), exhibits some features that are similar in both cases. As with the Schottky sample, it can be seen that the excited state signal apparently decreases more rapidly than the ground state signal directly after consumption of the oxide layer, a feature evident in the Ni*/Ni ratio profile between points A and B. The rate of decrease of both Ni and Ni* signals in Figure 7.12 (a) increases beyond point B, corresponding to a fluence of ~ 140,000μC/cm^2, a feature that also occurred in the Schottky sample profile, albeit following a different irradiation fluence. Such a rate change was not apparent in the earlier profiles on an Ohmic sample suggesting that the modified technique is capable of resolving features that were not previously possible.

Analysis of the excited/ground state ratio profile in Figure 7.12 (b) shows a far less changeable trend than was evident in Figure 7.10 (b). This indicates that the sample composition beneath the oxide layer of the Ohmic sample is far more homogeneous than that of the Schottky sample. Consequently, it can be suggested with some confidence that the contact layer has been substantially altered with the formation of Ni-silicide the most likely cause. Nevertheless, a noticeable decrease in the excited/ground state ratio following consumption of the oxide layer at point A can be observed on the Ohmic sample. The decrease continues a small distance beyond point B before levelling off for the majority of the contact layer. This indicates that the Ni-silicide composition changes, albeit gradually from the start of the contact layer to the end.

While direct comparison between the photo-ion intensity (and hence ratio magnitude) for individual depth profiles cannot be made because experimental conditions alter the efficiency of the process each time, variation in the relative intensities within the same profile does infer chemical changes. The average value of the ratio between points A and B is approximately 5-6% higher than the near-plateau region between 175,000μC/cm^2 and 360,000μC/cm^2. Therefore, it can be surmised that a matrix change is occurring over this region.

A major difference between the Schottky and Ohmic profiles regards the irradiation fluence required to profile the entire contact layer. In the earlier profiles, direct comparison could not be made due to the variation in the contact layer thickness in the Schottky and Ohmic samples. However, both sample types used in these experiments with the defocused ion beam consist of contact layers of equal thickness. In the case of the Schottky sample profile, the sample was exposed to an irradiation fluence of ~ 70,000-75,000μC/cm^2 to reach a point beyond which no further information of relevance could be gained. The equivalent fluence required in the Ohmic depth profile was ~ 400,000μC/cm^2, a substantial increase to say the least. TEM studies[7,8,9] have shown that Ni/SiC samples annealed beyond 950°C exhibit a substantially increased contact layer thickness. While the increased contact layer thickness of the Ohmic sample naturally increases the fluence required to reach the same point in the profile as the Schottky sample, the diffusion of Si into the Ni contact layer resulting in a dramatically altered contact layer inherently reduces the sputter yield and hence further increases the fluence that must be delivered to the sample to complete the profile.

By once again setting the OPO system to 251.670nm to obtain resonant ionisation of the $^3P_2$ Si state along with non-resonant ionisation of nickel, another depth profile comparing the variation of nickel and silicon with depth was obtained, as shown in Figure 7.13. With the addition of this profile, much of the structure of the Ohmic sample suddenly becomes far clearer. The Ni profile follows a very similar pattern to the Ni profiles in Figure 7.12 as expected, particularly the gradient change at point B, although the form of the profile is not as smooth as the earlier profile, primarily due to the inefficient ionisation scheme, which results in a substantially lower photo-ion signal. However, the interesting addition is that of the Si profile which, despite its low photo-ion signal also, reveals a most intriguing trend. Up to marker point A, both Ni and Si signals rise as the oxide layer is consumed then fall off practically in synchronisation.

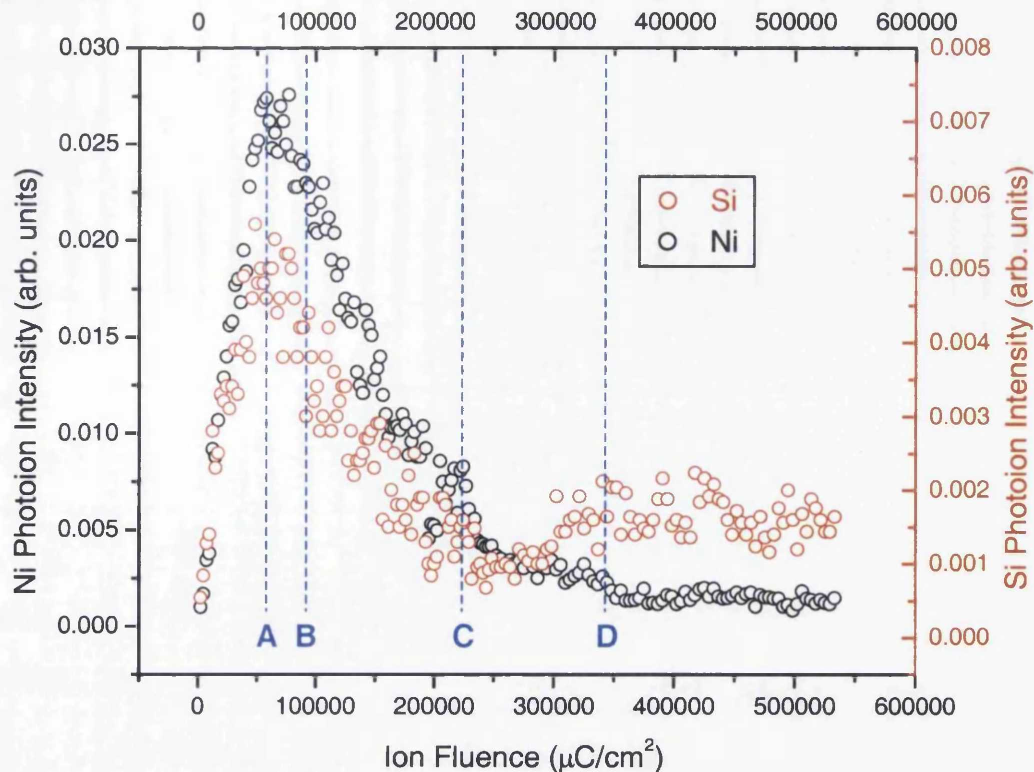

Figure 7.13: RIMS depth profile of Ni/SiC Ohmic sample (annealed to 1000°C) using 15keV Ar^+ defocused primary ions. Ni and Si plotted as a function of depth. Points A, B, C and D are marker points of interest.

The fascinating factor is the actual presence of Si from the very beginning of the profile. This confirms that the action of annealing causes Si from the substrate to diffuse to the farthest extremity of the contact layer. This is consistent with recent TEM and XPS studies [7,8,9] that have also revealed a substantially altered contact layer.

Further along the profile, another crucial feature is explained. At point C, a small hump in the Ni signal can be observed as was present in Figure 7.12 (a). Simultaneously, the Si signal rises from its minimum level at point C to a plateau region at point D corresponding to the SiC substrate. Clearly, an interface region can be identified between points C and D. Without this Ni/Si depth profile, it would be easy to misjudge the location of the interface and assume that it resided in the region between points A and C.

With the knowledge of the "true" interface location, we can revert back to the plot of the Ni*/Ni ratio in Figure 7.12(b). It has been mentioned that the ratio drops following consumption of the oxide layer as it did in the Schottky profile (Figure 7.10). The ratio then remains fairly constant until the interface, at which point it begins to rise gradually.

This fall in the ratio followed by a rise was also observed in the profile of the Schottky sample although the feature occurred over a much shorter depth range. Nevertheless, this suggests that a similar bonding mechanism is occurring in both samples although the degree of the changes appears far greater in the Ohmic sample.

7.6 Conclusion of RIMS depth profiles on Ni/SiC samples

The RIMS experiments in this chapter successfully add further insight into the chemical variations between Schottky and Ohmic samples. The initial experiments were encouraging, particularly so in the case of the Schottky sample (refer to Figure 7.4), showing a distinct interface and varying bonding mechanisms occurring over a short range. In comparison, the profiles obtained from Ohmic samples showed very little variation in the excited/ground state ratio, once the oxide layer had been removed, indicating a distinctly homogeneous structure with no apparent interface.

Nevertheless, the geometry of the crater eroded by the ion beams during acquisition of these profiles indicated that non-uniform beam fluence existed that could severely compromise depth resolution. To this end, the installation of a diaphragm aperture at the end of the primary ion column coupled with defocusing of the ion beam produced a far more uniform ion beam profile incident on the target. Tests with a thin, multi-layered sample confirmed that depth resolution was substantially improved and depth profiling on Ni/SiC samples could resume.

The first depth profile obtained on a Schottky sample using the new method (refer to Figure 7.10) yielded a general profile similar to that obtained without the defocused beam but containing more subtle features within the profile. A change of matrix at the start of the interface preceded a second matrix change also within the interface. Analysis of the relative ratios of the excited/ground states deduced that a probable region of Ni-silicide of the form Ni_2Si[12] was present at the beginning of the interface switching to a lower Ni concentration silicide, possibly NiSi or $NiSi_2$, over the latter part of the interface. Overall, however, the Ni/Si reaction is limited to a short-range effect, namely the interface itself.

The defocused ion beam depth profile obtained on the Ohmic sample (Figure 7.12) showed a similar improvement over the earlier depth profiles on an Ohmic sample, primarily with respect to resolution. Features that were not observed on earlier profiles

became apparent, while the plot of the excited/ground state ratio showed dramatically improved signal-to-noise ratio. As for the depth profile itself, a particularly homogeneous contact layer was observed with no discernible interface present. Consequently, it can be deduced that the action of annealing creates Si diffusion from the substrate into the contact layer and vice versa, Ni diffusion into the substrate with a fairly uniform Ni-silicide altered layer. While the altered layer appears generally consistent, the response of the excited/ground state ratio in the upper section of the layer suggests a different Ni-silicide composition may be present. Since the ratio is higher at the beginning of the layer, it is postulated that it may be composed of $NiSi_x$, where $x \geq 1$, whereas the bulk of the layer is composed of Ni_2Si.

The two-element RIMS depth profile on the same Ohmic sample, investigating resonantly ionised Si and non-resonantly ionised Ni, revealed the location of an interface between the altered layer and the substrate. It also confirmed the presence of Si throughout the contact layer while the overall fluence required to complete the profile determined that the contact layer was thicker than the as-deposited samples (even allowing for sputter yield reduction).

7.7 References

[1] A. Kestle, S.P. Wilks, P.R. Dunstan, M. Pritchard, P. Mawby, Electronics Letters Vol. **36** (3), 267 (2000).

[2] E.B. Saloman, Spectrochemica Acta. **B45**, 37 (1990).

[3] E.B. Saloman, Spectrochemica Acta. **B46**, 319 (1991).

[4] E.B. Saloman, Spectrochemica Acta. **B47**, 517 (1992).

[5] E.B. Saloman, Spectrochemica Acta. **B48**, 1139 (1993).

[6] J. Bastiaansen, F. Vervaecke, E. Vandeweert, P. Lievens, R. Silverans, Spectrochemica Acta. **B58**, 1147 (2003).

[7] B. Pécz, Appl. Surf. Sci. **184,** 287 (2001).

[8] Ts. Marinova, A. Kakanakova-Georgieva, V. Krastev, R. Kakanakov, M. Neshev, L. Kassamakova, O. Noblanc, C. Arnodo, S. Cassette, C. Brylinski, B. Pécz, G. Radnoczi, Gy. Vincze, Materials Science and Engineering **B46,** 223 (1997).

[9] B. Pécz, G. Radnoczi, S. Cassette, C. Brylinski, C. Arnodo, O. Noblanc, Diamond and Related Materials **6,** 1428 (1997).

[10] O. Bisi, C. Calandra, J. Phys. C. **14**, 5479 (1981).

[11] J. Bastiaansen, Electronic Processes during the Sputtering of Metals studied by Resonant Laser Ionization, PhD thesis, Katholieke Universiteit Leuven (2003).

[12] C.S. Pai, C.M. Hanson, S.S. Lau, J. Appl. Phys. **57** (2), 618 (1985).

Chapter 8: Conclusions and Future Work

8.1 Summary of Results

The detail present in the depth profiles produced via the TOF-SIMS and RIMS studies have revealed a wealth of information relating to the chemical composition of the interfaces between Ni and SiC. In particular, the optimisation of the primary ion beam characteristics, to give the required depth resolution, has indicated that it is possible to overcome some of the pitfalls of ion beam bombardment. It has been clear from both sets of studies that the electrical nature of the samples is very much dictated by the chemical properties of the Ni-SiC contact.

Experimental advances in the TOF-SIMS system at Swansea have seen the use of defocused 7keV Ga^+ ions, which gave a comparable depth resolution when compared to studies performed using the lower energy Ar^+ ions (4keV). Moreover, the routine use of the newly acquired LMIG has been established during the project and simulations have been made that verify the validity of using the Ga^+ ions in depth profiling for this system.

The RIMS experiments in Leuven have exploited the technique for looking at specific layers structures and gained an insight into depth-profiling, rather than surface or alloy material analysis which form the more standard RIMS measurements. Modification of the primary ion beam to enhance depth sensitivity and gain uniform ion ablation was a major obstacle and required aperture development and testing during the experimental run. Successful profiles based upon Schottky contacts and test structures indicated that a reproducible and depth sensitive set-up had been achieved. Appropriate ionisation schemes for Ni and Ni^* were instigated and it was also possible to mimic the TOF-SIMS studies using a Si ionisation scheme so that simultaneous Ni – Si acquisitions could be performed.

A summary graph of various depth-profiles is presented in Figure 8.1. The profiles were obtained from as-deposited Schottky Ni/SiC contacts, column (a), and annealed Ohmic Ni/SiC samples, column (b). Clear differences in composition versus depth can be observed between the TOF-SIMS profiles in Figure 8.1, row (i), when comparing the Schottky and Ohmic samples.

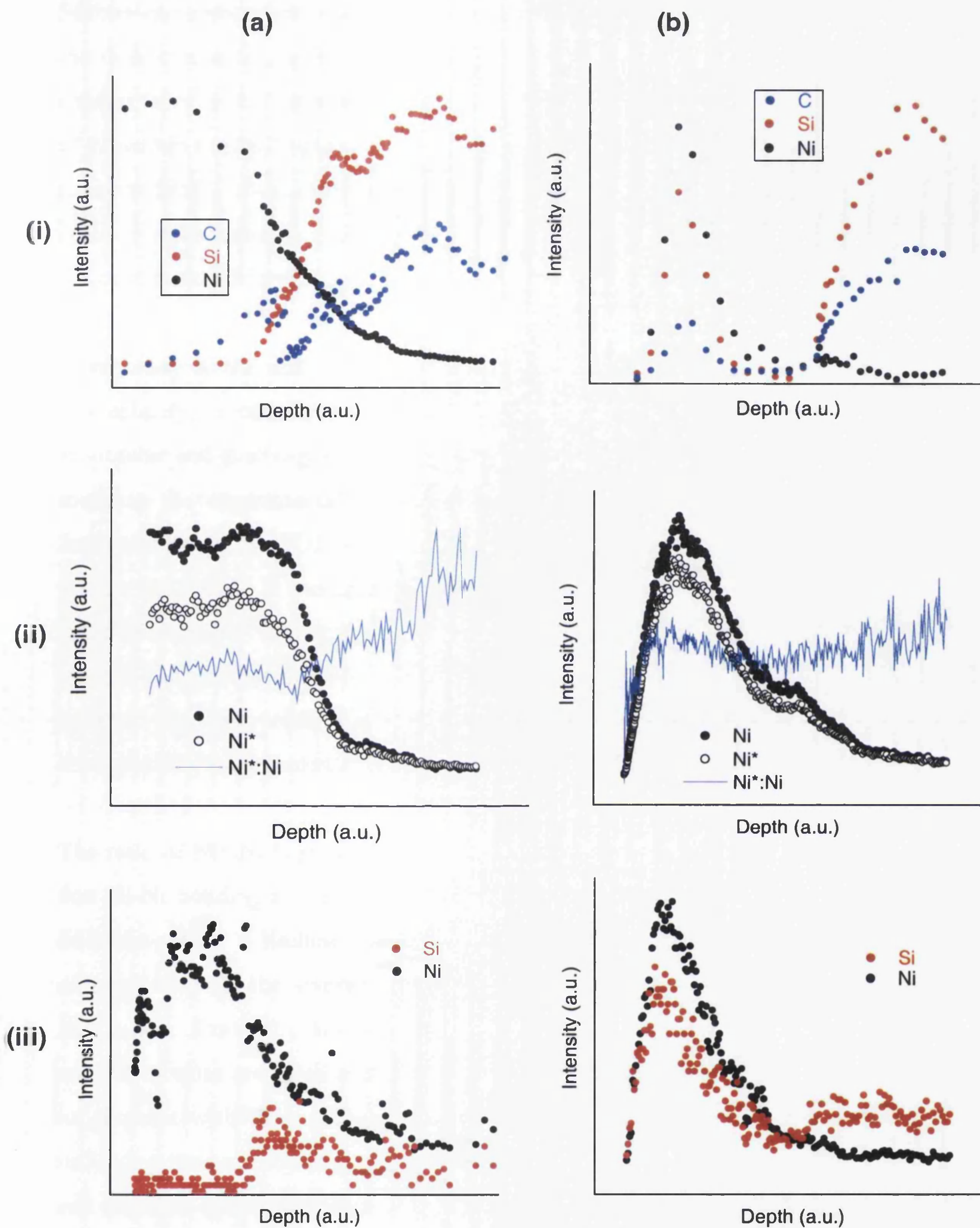

Figure 8.1: Comparison of depth profiles obtained on (a) Schottky and (b) Ohmic samples using (i) TOF-SIMS with a 7keV defocused Ga^+ ion beam, (ii) TOF-RIMS of Ni ground state (a^3F_4) and Ni excited state (a^3D_3) using a 15keV defocused Ar^+ ion beam, (iii) TOF-RIMS of Ni (non-resonant) and Si ($^3P_2$), also using a 15keV defocused Ar^+ ion beam.

Silicon and carbon both appear in significant quantities within the Ni contact layer for the Ohmic samples, whilst the Schottky samples indicate an abrupt transition from Ni contact layer to SiC substrate. Some beam effects may be responsible for the presence of Ni within the SiC region on the Schottky sample, and the results discuss these issues in more detail. It was clear from previous studies on Ni/SiC that the interface becomes reactive upon annealing and hence forms an Ohmic contact. Indeed, our studies indicate that the Si signal appears to extend throughout the complete 200nm contact.

A summary of the main RIMS depth profiles is presented in Figure 8.1 (ii) and (iii). Immediately, it can be seen that comparison to the TOF-SIMS profiles is highly favourable and much agreement exists between them due to careful beam considerations made in the experimental settings. In particular, the Ohmic samples confirm the features seen in the TOF-SIMS profiles for both the Ni signal and also the Si signal (Figure 8.1 (biii)). It was speculated that the TOF-SIMS signal from the Ohmic sample could be the result of a mixed matrix, affecting the ion yield and even the possibility of oxygen enhanced ion yield. However the similar signal rise in the RIMS profiles indicates that the selectively ionised neutrals also have an increased yield, further strengthening the arguments for a change of matrix affecting the yield.

The ratio of Ni*:Ni is presented for both types of samples in Figure 8.1 (ii). It is clear that Ni-Ni bonding in the Schottky gives a different ratio to the region closest to the interface where a limited silicide reaction looks likely. The Ohmic ratio is more complex due to the overall variation in ion yield and the relative lack of ratio fluctuation. Studies by Bastiaansen[1] have indicated that the ratio differences for bulk Ni silicide samples are small and thus an exact definition of the silicide phase is still hard to pinpoint with these measurements. However the studies have proven useful in indicating the need to develop experimental methods to overcome equipment variations and establish quantitative measurements, details of which are expanded upon in the final section.

8.2 Ni/SiC contacts, a proposed model based on TOF-SIMS and RIMS.

It appears that a limited reaction does occur between Ni and SiC of a Schottky contact, as the ratio change in Ni*:Ni at the interface is indicative of a bonding change. This is somewhat contrary to the early work of Pai *et al*[2] using x-ray diffraction and ion backscattering on Ni/SiC. Unfortunately, this work does not specify what SiC samples

were used and the composition of the SiC face used in making the contact. Our studies use a Si terminated epilayer and thus the reaction may be initiated. The TEM work of Pécz *et al*[3] also indicates an abrupt TEM image across the interface but no chemical EDS information has been published to verify the chemistry of the interface. Upon annealing a significant movement of atomic species is present across the interface and a Ni-silicide formation is clear. Previous studies have indicated that the likely silicide is Ni_2Si, whilst both the TOF-SIMS and RIMS profiles are indicating the presence of other possible silicide phases. Specifically, the change in ion yield and the subtle ratio change between Ni*:Ni near the interfacial region of the Ohmic contact are key indicators. The reduction in ratio is indicative of the presence of Ni_2Si at the interface, whilst the slightly higher ratio within the contact (away from the interface) is suggestive of NiSi or $NiSi_2$. These ratio changes are in agreement with studies from Leuven on bulk silicides[1]. This model is also encouraging because it supports the recent literature evidence[4] of Ni_2Si forming a good Ohmic region, at the interface of Ni/SiC contacts.

Raman spectroscopy experiments performed on as-deposited and 1000°C annealed Ni/4H-SiC samples have investigated the carbon phases present. This provides an area of chemical information that was unobtainable using the RIMS technique, due to the inaccessibility of efficient ionisation schemes. The results showed that there was a considerable difference between the relative ratios of the peaks associated with ordered (graphitic) carbon and disordered carbon in the as-deposited and annealed samples. A greater quantity of carbon accumulation was discovered in the annealed samples, the enhanced conductivity of which could be a factor influencing the change from rectifying electrical properties in these samples.

It can be deduced that the carbon accumulation arises in the Ohmic samples due to the extreme interdiffusion of nickel in the contact layer and silicon from the substrate. The silicon diffusion gives rises to a vacancy, or void, which is surrounded by carbon, hence an apparent accumulation is observed at these locations. These vacancies effectively act as dopant sites, which influence the interface by causing a decrease in the width of the depletion region, confining the field and increasing the sharpness of the band-bending thus allowing electrons to tunnel through the Schottky barrier, yielding Ohmic behaviour.

8.3 Suggestions for future work

There are many extensions that can be made to these studies. Many concern experimental system improvements that may be employed to maximise depth resolution, while other extensions to the work involve studies on modified contacts with interlayers. Such modifications could include the deposition of a thin Si buffer layer on the SiC substrate, prior to Ni contact layer deposition. XPS [5,6] and TEM [7] studies have been performed on Ni/Si/SiC samples and these show that the buffer layer inhibits the reaction between the Ni and SiC by reducing the decomposition of the SiC. It also serves to reduce the number of voids present within the contact layer.

Discrimination of the interfaces straddling the thin Si layer would require a further improvement in depth resolution compared to the current experimental set-up. Chapter 2 describes the necessary experimental conditions for optimum depth resolution, which, in general, require a high mass, low energy primary ion, intercepting the target at normal incidence that also does not induce excessive surface roughening of the target[8]. Normal incidence could be achieved by means of a sample stage with rotational capabilities. The sample bias could then be adjusted to alter the effective primary ion energy without the problem of beam shift on the sample as a result of the bias. The gallium used in the LMIG ion source is of sufficient mass to satisfy the high mass requirement for Ni/SiC experiments and although a caesium source could improve it further, the advantage would not necessarily outweigh the expense.

A useful addition to the acquisition of depth profiles would be an automated routine to ablate the sample and acquire mass spectra consecutively, such as that used on the Leuven system. This would permit depth profile acquisition in a more reasonable timescale and with more data points

Using both ion sources to obtain a depth profile initially proved to be most encouraging due to the low energy operating range of the DP. As described in chapter 6, section 6.3, this technique was flawed due to inadequate beam position control. However, the Ionoptika raster scan unit has been used to successfully control the raster scan plates of the duoplasmatron (DP) ion source. Therefore, it should be possible to control both ion sources during a depth profile and obtain higher resolution depth profiles.

The RIMS studies could also make use of these resolution improvements, while additional laser systems could permit simultaneous measurement of C, Si, Ni (ground state) and Ni (excited state). This would give a more complete description of the chemical variations as a function of depth. Perhaps the most useful development of this work would be to install a pure Ni and various standard Ni-silicide samples into the chamber along with the sample for analysis, as shown in Figure 8.2.

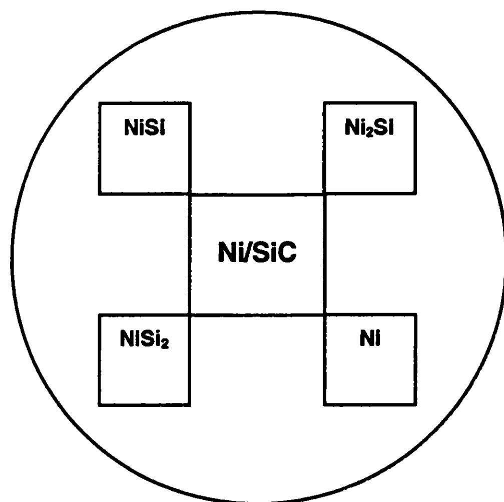

Figure 8.2: Method for avoiding experimental apparatus fluctuations by sampling standard reference samples in concert with analysis.

The principle is that the analysis of the Ni/SiC sample could incorporate a routine whereby each of the standard reference samples is probed at defined intervals during the depth profile to obtain a normalisation factor. This could compensate for variations in the apparatus during sample change operations that can lead to inaccuracy in the depth profile and permit direct identification of the Ni-silicide phase present in the sample.

8.4 References

[1] J. Bastiaansen, Electronic Processes during Sputtering of Metals studied by Resonant Laser Ionization, PhD thesis, Katholieke Universiteit Leuven (2003).

[2] C.S. Pai, C.M. Hanson, S.S. Lau, J. Appl. Phys. **57** (2), 618 (1985)

[3] B. Pécz, G. Radnóczi, S. Cassette, C. Brylinski, C. Arnodo, O.Noblanc, Diamond and Related Materials **6**, 1428 (1997).

[4] Ts. Marinova, A. Kakanakova-Georgieva, V. Krastev, R. Kakanakov, M. Neshev, L. Kassamakova, O. Noblanc, C. Arnodo, S. Cassette, C. Brylinski, B. Pécz, G. Radnoczi, Gy. Vincze, Materials Science and Engineering **B46**, 223 (1997).

[5] W.Y. Lee, The control of metal-silicon carbide contact using a silicon interlayer, PhD Thesis, University of Wales Swansea (2004).

[6] W.Y. Lee, K.S. Teng, S.P. Wilks, Silicon carbide and related materials 2003 (1,2) 457 (2004).

[7] B.Pécz, Appl. Surf. Sci. **184**, 287 (2001).

[8] M.G. Dowsett, Appl. Surf. Sci. **203-204**, 5 (2003).